IMPROVED TORQUE AND SPEED CONTROL PERFORMANCE IN A VECTOR-CONTROLLED PWM-VSI FED SURFACE-MOUNTED PMSM DRIVE WITH CONVENTIONAL P-I CONTROLLERS

A THESIS SUBMITTED TO
THE GRADUATE SCHOOL OF NATURAL AND APPLIED SCIENCES
OF
MIDDLE EAST TECHNICAL UNIVERSITY

BY

ÜMİT BÜYÜKKELEŞ

IN PARTIAL FULFILLMENT OF THE REQUIREMENTS
FOR
THE DEGREE OF MASTER OF SCIENCE
IN
ELECTRICAL AND ELECTRONICS ENGINEERING

APRIL 2012

Approval of the thesis:

IMPROVED TORQUE AND SPEED CONTROL PERFORMANCE IN A VECTOR-CONTROLLED PWM-VSI FED SURFACE-MOUNTED PMSM DRIVE WITH CONVENTIONAL P-I CONTROLLERS

submitted by **ÜMİT BÜYÜKKELEŞ** in partial fulfillment of the requirements for the degree of **Master of Science in Electrical and Electronics Engineering Department, Middle East Technical University** by,

Prof. Dr. Canan Özgen
Dean, Graduate School of **Natural and Applied Sciences** __________

Prof. Dr. İsmet Erkmen
Head of Department, **Electrical and Electronics Engineering** __________

Prof. Dr. Aydın Ersak
Supervisor, **Electrical and Electronics Engineering Dept., METU** __________

Examining Committee Members:

Prof. Dr. Muammer ERMİŞ
Electrical and Electronics Engineering Dept., METU ____________________

Prof. Dr. Aydın ERSAK
Electrical and Electronics Engineering Dept., METU ____________________

Prof. Dr. Işık ÇADIRCI
Electrical and Electronics Engineering Dept., METU ____________________

Dr. Faruk BİLGİN
Space Technologies Research Institute, TÜBİTAK ____________________

M. Sc. Bülent BİLGİN
ASELSAN Inc. ____________________

Date: 26/04/2012

I hereby declare that all information in this document has been obtained and presented in accordance with academic rules and ethical conduct. I also declare that, as required by these rules and conduct, I have fully cited and referenced all material and results that are not original to this work.

Name, Last name : Ümit BÜYÜKKELEŞ

Signature :

ABSTRACT

IMPROVED TORQUE AND SPEED CONTROL PERFORMANCE IN A VECTOR-CONTROLLED PWM-VSI FED SURFACE-MOUNTED PMSM DRIVE WITH CONVENTIONAL P-I CONTROLLERS

Büyükkeleş, Ümit

M. Sc., Department of Electrical and Electronics Engineering
Supervisor: Prof. Dr. Aydın Ersak

April 2012, 134 pages

In this thesis, high performance torque and speed control for a surface-mounted permanent magnet synchronous machine (PMSM) is designed, simulated and implemented. A three-phase two-level pulse width modulation voltage-source inverter (PWM-VSI) with power MOSFETs is used to feed the PMSM.

The study has three objectives. The first is to compensate the voltage disturbance caused by nonideal characteristics of the voltage-source inverter (VSI). The second is to decouple the coupled variables in the synchronous reference frame model of the PMSM. The last is to design a load torque estimator in order to increase the disturbance rejection capability of the speed control. The angular acceleration required for load torque estimation is extracted through a Kalman filter from noisy velocity measurements.

Proposed methods for improved torque and speed control performance are verified through simulations and experimental tests. The drive system is modeled in Matlab/Simulink, and control algorithms are developed based on this model. The experimental drive system comprises a three-phase VSI and a 385 W surface-mounted PMSM. Control algorithms developed in the study have been implemented in a digital signal processor (DSP) board and tested comprehensively. With the use of the proposed methods, a considerable improvement of torque and speed control performance has been achieved.

Keywords: Surface-mounted PMSM, vector control, inverter non-linearity compensation, load torque estimation, Kalman filtering.

ÖZ

GELENEKSEL P-I DENETLEYİCİLERİN KULLANILDIĞI VEKTÖR DENETİMLİ PWM EVİRİCİ BESLEMELİ YÜZEY MIKNATISLI SENKRON MOTOR SÜRÜŞÜNDE MOMENT VE HIZ DENETİM PERFORMANSININ İYİLEŞTİRİLMESİ

Büyükkeleş, Ümit

Yüksek Lisans, Elektrik Elektronik Mühendisliği Bölümü
Tez Yöneticisi: Prof. Dr. Aydın Ersak

Nisan 2012, 134 sayfa

Bu tezde, bir yüzey mıknatıslı senkron motorun (YMSM) yüksek performanslı moment ve hız denetimi tasarlanmış, bilgisayar benzetimi yapılmış ve donanım üzerinde gerçeklenmiştir. YMSM, güç MOSFET'leri ile oluşturulmuş üç-fazlı iki-seviyeli gerilim kaynaklı evirici (GKE) ile beslenmiştir.

Çalışmanın üç amacı bulunmaktadır. Birincisi, GKE'nin ideal olmayan özelliklerinden kaynaklı bozucu etkilerin giderilmesidir. İkincisi YMSM'nin senkron referans düzlemindeki modelinde bulunan bağımlı değişkenlerin bağımsız hale getirilmesidir. Üçüncüsü ise hız denetleyicisinin bozucu etki giderme performansını geliştirmek amacıyla yük momentini tahmin edecek bir kestiricinin tasarlanmasıdır. Yük momenti kestiricisi için gerekli olan açısal ivme bilgisi gürültülü hız ölçümlerinden bir Kalman filtre yardımıyla çıkartılmıştır.

Önerilen yöntemler bilgisayar benzetimleri ve deney çalışmalarıyla doğrulanmıştır. Sürüş sistemi Matlab/Simulink yazılımında modellenmiş ve denetim algoritmaları bu model üzerinde geliştirilmiştir. Deney çalışmaları için üç-fazlı GKE ve 385 W gücünde YMSM'den oluşan bir sürüş sistemi kullanılmıştır. Denetim algoritmaları sayısal işaret işleyicisi (DSP) tabanlı bir kartta gerçeklenmiş ve ayrıntılı bir şekilde test edilmiştir. Önerilen yöntemlerin kullanımıyla moment ve hız performansında önemli iyileşmeler sağlanmıştır.

Anahtar kelimeler: yüzey mıknatıslı senkron motor, vektör denetimi, evirici doğrusalsızlığını giderme, yük momenti kestirimi, Kalman filtreleme.

To My Wife and My Daughter

ACKNOWLEDGEMENTS

I thank my supervisor Prof. Dr. Aydın Ersak for his guidance throughout the thesis.

I am also grateful to ASELSAN Inc. for the realization of this thesis.

I wish to express my deepest gratitude to my wife Melike and our families for their endless support.

Special thanks to Kenan Ahıska for his valuable helps especially in editing my thesis and the conference paper.

Finally, I would like to thank my friends and colleagues Hüseyin Meşe, Aycan Uçar, Tufan Ayhan, Murat Ertek and İsmail Akbulut for their support and help throughout the thesis.

I am thankful to "the God" for all the wonderful things that he has given to me.

TABLE OF CONTENTS

LIST OF TABLES

TABLES

LIST OF FIGURES

FIGURES

LIST OF ABBREVIATIONS

PMSM	Permanent Magnet Synchronous Machine
PWM	Pulse Width Modulation
VSI	Voltage Source Inverter
mmf	Magnetomotive Force
SFCR	Synchronous Frame Current Regulator
P-I	Proportional-Integral
Nm	Newton meter
rpm	Revolution per minute

CHAPTER 1

INTRODUCTION

1.1 AC Motor Drives and Permanent Magnet Synchronous Machine

Electric motors are employed in many applications such as pumps, compressors, elevators, cranes, white goods, electric vehicles, electric tractions etc. Traditionally, electric motors were operated without speed control. However, with further studies it is proved that, with an adjustable speed, motor drive systems offer higher efficiency and lower maintenance. “Prior to the 1950s all such applications required the use of a dc motor drive since ac motors were not capable of true adjustable or smoothly varying speed since, they inherently operated synchronously or nearly synchronously with the frequency of electrical input [3]“. Dc motor drives have been the most popular drives for speed control because of their lower cost and ease to control. However, they are losing their popularity to the ac motors which do not have slip rings and brushes. Brushless ac motors have some advantages over dc motors. Due to the lack of brushes, they can reach higher speeds and also require less maintenance. In general, an ac machine of the same torque capacity is smaller than the equivalent dc machine.

Ac motors can be directly fed from the utility source. However, in order to adjust the speed, an electric drive system should be implemented. An electric drive consists of a power converter, controller, sensors and other necessary electronic circuits as demonstrated in Figure 1.1. The power converter gets its power from the utility source or from a dc power supply such as a battery. Controller gets the feedback from the sensor and receives the commands from an interface and then actuates the power converter accordingly.

If the power is supplied from the utility, a rectifier is used at the input. The rectified voltage is filtered with a dc-link capacitor. Then, by means of an inverter, the ac waveform with the desired frequency and magnitude can be generated at the output to supply the ac machine. If the power is supplied from a battery, rectification is not needed. In this thesis, electric drive is fed by a battery of 24 V therefore, the rectifier issues are not examined.

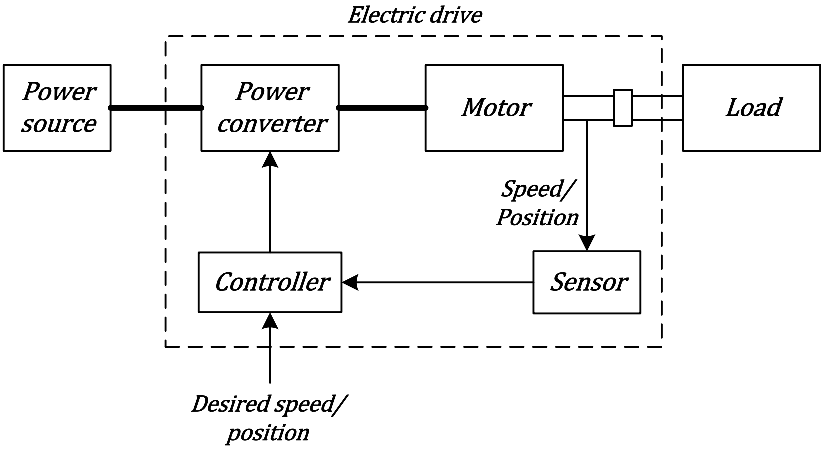

Figure 1.1. Electric drive system block diagram.

Two-level three-phase voltage-source inverters (VSIs) are the most widely used circuits to supply three-phase ac machines. It consists of six power transistors and anti-parallel diodes (freewheeling diodes) as shown in Figure 1.2. In low voltage applications, approximately lower than 250 V, power MOSFETs are used in the VSI because of their lower device voltage drop compared to IGBT. In this thesis, VSI is constructed with power MOSFETS.

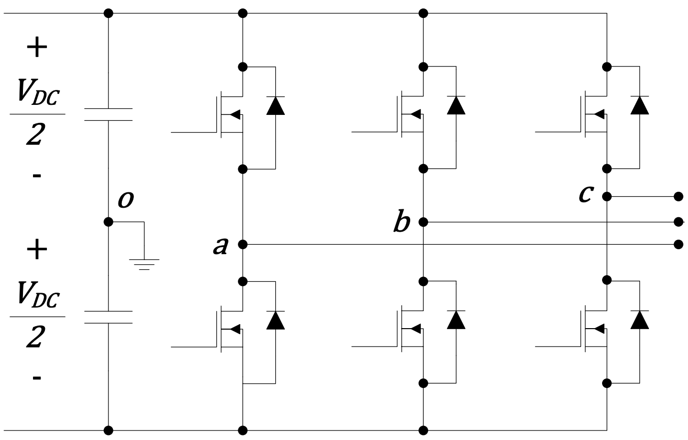

Figure 1.2. Two-level three-phase voltage source inverter.

Recently, permanent magnet synchronous machines (PMSMs) become an important class of high performance ac drives. PMSMs are special types of the synchronous machines. They have conventional three-phase stator windings but, instead of a field winding, permanent magnets produce field flux. Synchronous machines with electrically excited field winding require brushes and slip rings to transfer current to the rotor. The use of permanent magnets eliminates this requirement thus, problems related to the brushes and slip rings are overcome. Lack of brushes also results in a more robust mechanical construction. Moreover, the copper losses are eliminated therefore; higher efficiency and higher torque/inertia ratio can be achieved.

PMSM types are demonstrated in Figure 1.3. When the stator windings are concentrated, the machine is named as trapezoidal type or brushless dc (BLDC) machine. This machine has a trapezoidal back-emf waveform. When the stator windings are sinusoidally distributed, the back-emf waveform is also sinusoidal and the machine is named as permanent magnet ac (PMAC) machine. This type of PMSM is usually named as servo motor and widely used in high performance servo applications.

The PMSMs are further classified according to their magnet mounting types. One of them is the surface-mounted PMSM where the magnets are mounted on the rotor surface as demonstrated in Figure 1.4. The other type is the interior permanent magnet (IPM) machine where the magnets are buried inside the rotor core.

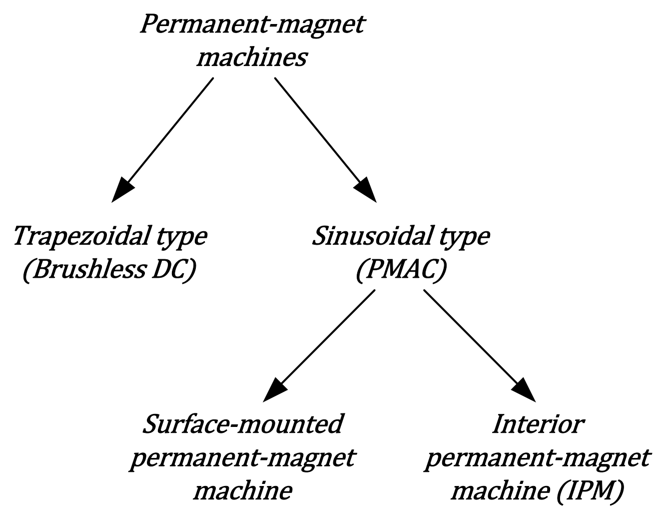

Figure 1.3. Permanent-magnet machine types.

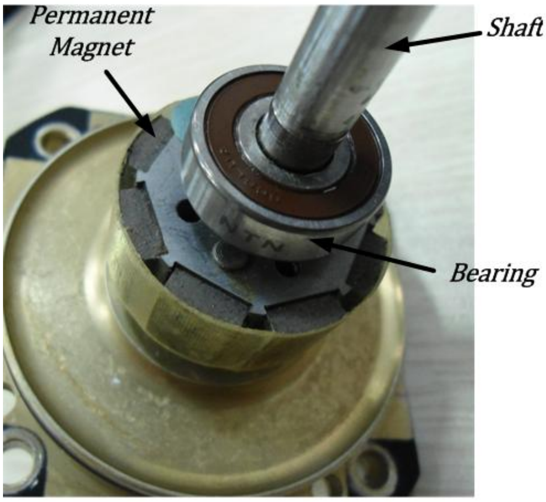

Figure 1.4. Surface-mounted PMSM rotor.

1.2 High Performance PMSM Drive

There are mainly two ac machine control methods, scalar and vector control. Scalar control depends on the steady-state model of the ac machine. Only magnitude and frequency of the voltages, currents and flux linkages are controlled. This control method is used in applications where dynamic performance is of no account. In vector control, spatial positions of the magnetic fluxes in the machine are also controlled [42]. By means of the vector control, the electromagnetic torque can be controlled both in steady-state and in transient operations of the ac machine therefore; it is generally used in applications where high dynamic performance is desired.

Field-oriented control is a type of vector control where the field flux, armature mmf and the angle between them are controlled separately. It is based on the vector coordinate transformations. In this method, the motor equations are transformed into a coordinate system which rotates in synchronism with the field flux. It permits separately control of torque and flux quantities by utilizing current control loop with P-I controllers like in a dc machine control.

Usually, current controllers are designed in the synchronous reference frame since ac currents at synchronous frequency can be transformed into dc currents, which makes the closed-loop system robust to the operating frequency. The synchronous frame model of a PMSM can be expressed as a multiple-input multiple-output (MIMO) system where the stator d- and q-axis voltages are the inputs and the stator d- and q-axis currents and rotor velocity are the system outputs. In the synchronous frame model of the PMSM, d- and q-axis voltages, currents and rotor velocity terms are coupled to each other [44], [45]. These couplings lead to degradation of the controller performance in high speed operation of the machine [44], [46]. Therefore, it is desirable to decouple these coupled terms by a proper controller design. Decoupling of these variables is one of the goals of this thesis.

Voltage-source inverters (VSIs) are the most widely used circuits for PMSM supply. Despite their advantages, VSIs suffer from problems due to non-ideal behavior of the power switches. This results in distortion on the output voltage of the VSI. In most of the applications, output voltage distortion causes serious problems such as instability or torque ripple in motor drive systems [43]. Therefore, an accurate voltage synthesis at the output of the VSI is needed. This is another goal of this thesis.

There are several causes of voltage distortion in the VSI output voltage; some of them are caused by the inserted dead-time, finite turn-on/off time of the power switches and voltage drop on them. To avoid a short circuit in the dc-link (shoot-through), a finite time must be inserted before turning-on the power switches in the VSI. This period is generally called as *blanking-time* or *dead-time*. During the dead-time, the output voltage depends primarily on the related phase current direction which results in a loss of control of the voltage. The dead-time guarantees a safe operation but it causes serious voltage distortion.

In an open-loop pulse width modulation voltage-source inverter (PWM-VSI) fed drive system, inverter nonlinearity can lead to instability and extra losses in the driven machine [20], [23], [26], [28]. In a closed-loop drive system, this nonlinearity causes distortion in current waveform, and ripples on the torque output [24], [26], [28]. In direct torque or sensorless control applications, the output voltage is to be known for flux-linkage estimation. It is not convenient to measure output voltage. In general, reference voltages are used instead. However, due to the nonlinearity of the VSI, reference voltages deviate extensively from the output voltages [28], [36]. Therefore, in most of the applications these distortions cannot be neglected and are need to be eliminated.

There are various approaches to compensate the nonlinearity of the VSI [20]-[33]. A different VSI configuration can be designed to prevent the shoot-through thus eliminating the requirement of dead-time [32]. In this configuration, problems regarding to dead-time are eliminated but other sources of nonlinearity still exist. Moreover, it requires hardware modification which is not easy to implement. In conventional VSI configurations, usually a nonlinearity compensation algorithm is employed. The widely used method is based on the modification of the reference voltages to compensate the volt-second error [27]. This method is known as *volt-second compensation* in which the volt-second error is averaged over a PWM carrier cycle and then added to the reference voltage. Earlier studies used the output voltage measurement to detect the volt-second [20], [23] which was troublesome since, the output voltages are in PWM waveforms [37]. Instead of using voltage feedback, usually current feedback type compensation method is preferred because, voltage error depends on the direction of current [21], [22], [26], [30], [33]. First difficulty in this technique is the detection of the current direction owing to the fact that, current sensing process has some inherent delay and offset/gain/linearity errors. Especially, when current is close to zero, the detection of the current direction is quite challenging on account of the switching ripple and zero-current clamping effect [28], [33]. To handle zero current crossings, one method is based on utilizing the current reconstruction [27]; another is the zero-current clamping compensation [28]. Sometimes a smooth hysteresis curve is applied to the compensation signal [29]. Another problem in this method is the variation of the parameters used in calculation of the compensation signal. Compensation methods based on disturbance observer can also be employed to overcome this problem [31], [34], [37].

In low voltage applications, such as battery-powered applications, power MOSFETs are utilized due to the lower device voltage drop. VSI nonlinearity studies made so far are focused mostly on to the voltage distortion analysis for IGBT inverters but very few cover MOSFET inverters. Switch voltage drops are quite different between the two; an IGBT has a diode-like voltage drop whereas a MOSFET has a resistance-like voltage drop. In [24] a MOSFET inverter is analyzed but this distinction was not adequately accounted. Another study considers this difference but the analysis was not detailed [35]. In this thesis, the voltage distortion in a three-phase VSI which is realized by power MOSFETs is analyzed. Volt-second algorithm is applied to compensate the voltage distortion. The rotor angle information is implemented to determine the direction of the current in order to eliminate the problems regarding to switching nature of the current. The method proposed in this study, does not require the d-axis current to be zero. Simulation and experimental results are provided to verify the validity of the analysis and the compensation technique.

Another problem faced in electric motor drive systems is the effect of disturbance torque (sometimes called as load torque). The common sources of the load torques are friction torques, externally applied torques and unbalanced mass center. They cause unacceptable motion errors. Conventional P-I speed controllers cannot fully suppress these disturbance torques due to limited bandwidth of the controller.

Disturbance rejection capability of the speed controller can be increased by the use of *load torque estimator*. Load torque estimator calculates the disturbance torque from the measured phase current and motor speed. Then, the necessary compensation current for the estimated torque is added to the current reference. By means of this compensation current, disturbance torques can be suppressed faster than the response time of the feedback loop [47].

Load torque estimator can also handle parameter variations such as variation of total inertia and variation of motor torque constant as well as suppressing the load torque [39]. This is a very useful property because; inertia variations are usually encountered due to payload variations. Torque constant is also likely to vary, due to the temperature dependence of this constant.

Load torque estimation algorithm requires the angular acceleration information. The use of angular acceleration transducers is not feasible because, a few of them exist in the market and they are not economical [41]. Usually, derivative of the velocity feedback is used instead [47]. However, differentiation techniques produce severe noisy signals.

In this thesis, a linear stochastic observer, *Kalman filter* is implemented for angular acceleration estimation. Then, load torque is estimated using this acceleration information, measured current and nominal values of inertia and torque constants. Compensating current corresponds to the estimated load torque is added to the current reference. Simulation and experimental results are provided to verify the validity of the load torque estimation.

1.3 Objectives of the Thesis

In this thesis, as a power converter, voltage-source inverter is utilized. As stated, the output voltage of the VSI is distorted due to non-ideal behavior of the power switches. First objective of the thesis is to compensate this distortion.

Synchronous frame current regulator (SFCR), a widely used current control method is implemented in this thesis. Although it offers the regulation of the currents in a wide speed range, it has some disadvantages. One of them is that, it is more complex and requires more computational effort. However this can be overcome by the emergent high performance

DSPs. Another disadvantage is that, in the synchronous frame model of the PMSM frequency dependent couplings exist between the mechanical system and electrical system and also between the torque-axis (q-axis) and flux-axis (d-axis). The second objective of the thesis is to decouple these variables.

In general, P-I controllers are implemented for speed regulation. Although they offer good steady-state response, the transient performance is limited because; controller bandwidth is limited due to practical reasons. Their disturbance rejection capability is limited by the bandwidth of the controller. The last objective of the thesis is to design a load torque estimator in order to increase the disturbance rejection capability of the speed controller.

Besides these major objectives, there are minor objectives of the thesis. One of them can be stated as, to derive and simulate the dynamical model of the surface-mounted PMSM. Another is to investigate the characteristics of the surface-mounted PMSM under different torque angles.

Motivation of the thesis can be expressed briefly as, improving the torque and speed control performance of the PMSM drive system.

1.4 Scope of the Thesis

The thesis consists of seven chapters. CHAPTER 1 is an introduction. In CHAPTER 2, mathematical model of the PMSM is presented. Space vector notation and reference frame transformations are explained. Dynamical model of the surface-mounted PMSM is derived from the machine equations in a, b, c reference frame. Electromagnetic torque equations and electromechanical equations are derived. Block diagram of the machine is presented. Different torque angle conditions are examined. CHAPTER 3 is devoted to voltage-source inverters (VSIs). Specifically, two-level three-phase VSI is analyzed. Space vector pulse width modulation scheme is described. CHAPTER 4 gives a review of PM synchronous motor vector control method. Current regulation issues are examined. Speed control of the machine is also presented in this chapter. In CHAPTER 5, the analysis of the conventional current control and speed control is performed and improvements on them are proposed. The theoretical confirmations of the proposed methods are given. Simulation and experimental results are demonstrated in CHAPTER 6. CHAPTER 7 includes the conclusions. Possible future works are stated in this section.

CHAPTER 2

DYNAMIC MODEL OF THE SURFACE-MOUNTED PMSM

2.1 Introduction

Analysis of ac machines is typically presented by means of the so-called per phase equivalent circuit. However, this model is inadequate when applied to dynamic conditions as encountered in transient responses of the machine. Therefore, a dynamic model of the ac machine should be built.

Developing a mathematical model is the key point for controlling an electric motor. In this chapter, mathematical model of the surface-mounted PMSM is derived. Space vector notation and reference frame transformations are explained. Electromagnetic torque equations and electromechanical equations are attained. Block diagram of the machine is presented. Different torque angle conditions are examined.

2.2 Stator Voltage Equations in the Stationary a, b, c Reference Frame

In a PMSM the rotor houses the permanent magnets which establish a dc magnetic field linking the surrounding three-phase stator windings placed spatially 120^0 apart from each other as shown in Figure 2.1. Two-pole PMSM structure is depicted in the figure nevertheless, the analysis is applicable to machines with any number of poles. Permanent magnets are on the surface of the rotor but, they are shown as a single bar magnet inside the rotor for a better insight. Although stator windings are sinusoidally distributed, they are represented as concentrated windings. To derive the model, magnetic saturation, core losses and eddy currents are neglected.

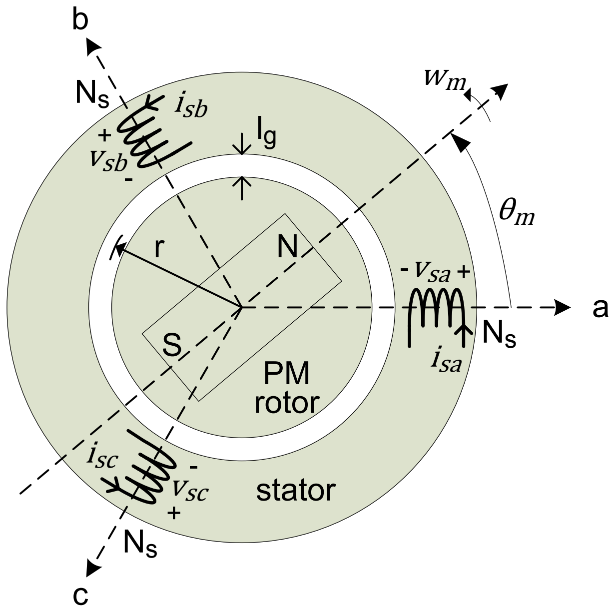

Figure 2.1. Three-phase permanent-magnet synchronous machine structure.

Instantaneous stator voltages developed in these three windings can be written as:

$$v_{sa} = R_s i_{sa} + \frac{d}{dt}\lambda_{sa} \tag{2.1}$$

$$v_{sb} = R_s i_{sb} + \frac{d}{dt}\lambda_{sb} \tag{2.2}$$

$$v_{sc} = R_s i_{sc} + \frac{d}{dt}\lambda_{sc} \tag{2.3}$$

where v_{sa}, v_{sb}, v_{sc} are stator voltages, i_{sa}, i_{sb}, i_{sc} are stator currents, R_s is the stator resistance and λ_{sa}, λ_{sb}, λ_{sc} are the flux linkages of the corresponding phases. Here it is assumed that, all three-phase windings have an equal resistance such that, $R_{sa} = R_{sb} = R_{sc} = R_s$.

The flux linkages with the stator winding for one of the phases consist of two components from stator and rotor,

$$\lambda_s = \lambda_{s(s)} + \lambda_{s(r)}. \tag{2.4}$$

Here $\lambda_{s(s)}$ is the flux linkage with the stator phase winding due to the stator currents and $\lambda_{s(r)}$ is the flux linkage with the stator phase winding due to the rotor flux. Therefore, the flux-linkages of the stator windings, λ_{sa}, λ_{sb} and λ_{sc} can be written as:

$$\lambda_{sa} = L_{sa} i_{sa} + M_{sab} i_{sb} + M_{sac} i_{sc} + \lambda_{PM} \cos\theta_r \tag{2.5}$$

$$\lambda_{sb} = M_{sba} i_{sa} + L_{sb} i_{sb} + M_{sbc} i_{sc} + \lambda_{PM} \cos(\theta_r - \frac{2\pi}{3}) \tag{2.6}$$

$$\lambda_{sc} = M_{sca} i_{sa} + M_{scb} i_{sb} + L_{sc} i_{sc} + \lambda_{PM} \cos(\theta_r - \frac{4\pi}{3}) \tag{2.7}$$

where L_{sa}, L_{sb} and L_{sc} are the self-inductances of the stator phases-a, -b and –c respectively, M_{sab}, M_{sac} and M_{sbc} are the mutual inductances between stator phases-a and –b; -a and –c; -b and -c, respectively. It is assumed that, all three stator phases have equal self-inductances such that, $L_{sa} = L_{sb} = L_{sc}$. Also M_{sab} is assumed to be equal to M_{sba} where M_{sab} is the mutual inductance of the phase-a winding due to the current flow in phase-b winding and M_{sba} is the mutual inductance of the phase-b winding due to the current flow in phase-a winding. Similarly, $M_{sac} = M_{sca}$ and $M_{sbc} = M_{scb}$.

λ_{PM} is the flux linkage with the stator phase windings due to the flux produced by the permanent magnets placed on the rotor surface. θ_r is the electrical angle between the axis of the rotor flux and stator phase-a axis which is related with the spatial angle of the rotor as in (2.8) where P is the number of poles.

$$\theta_r = \frac{P}{2}\theta_m\,. \tag{2.8}$$

The self-inductance of a stator phase can be defined as:

$$L_{sa} = L_{sb} = L_{sc} = L_{ls} + L_{ms} \tag{2.9}$$

where L_{ls} is the leakage inductance which accounts for the flux produced by the stator winding which does not cross the air gap. L_{ms} is the magnetizing inductance that can be formulated as,

$$L_{ms} = \mu_0 \pi \frac{rl}{l_g} \frac{N_s^2}{4} \tag{2.10}$$

where μ_0 is the permeability of air, r is the mean radius at the air gap, l is the length of the rotor along its shaft axis, l_g is the air gap length and N_s is the number of turns per phase in the stator winding. Since the surface-mounted PMSMs are almost always non-salient, it is assumed that, air gap length l_g does not vary with θ_r.

Mutual inductances between two stator phases can be found as,

$$M_{sab} = M_{sac} = M_{sbc} = (\cos \frac{2\pi}{3})\, L_{ms} = -\frac{L_{ms}}{2} \tag{2.11}$$

Detailed information and derivations can be found in [3] and [4].

2.3 Space Vector Notation

Each stator phase winding produces a sinusoidally distributed mmf $\overrightarrow{\mathrm{F_{sa}}}$, $\overrightarrow{\mathrm{F_{sb}}}$ and $\overrightarrow{\mathrm{F_{sc}}}$ in the air gap which can be represented by vectors along the axis of that phase. The resultant stator mmf, $\overrightarrow{\mathrm{F_s}}$ at any point in the air gap around the rotor periphery can be represented by a vector which is the sum of mmf vectors due to all three phases as shown in Figure 2.2.

The resultant vector of any three-phase stator variable (such as mmf distributions, currents, voltages or flux linkages) can be written as the sum of the instantaneous values of that variable according to,

$$\vec{k}^a = \frac{2}{3}[k_{sa} + \vec{a}k_{sb} + \vec{a}^2 k_{sc}] \tag{2.12}$$

where k_{sa}, k_{sb} and k_{sc} can be any of three-phase stator variables such as current, voltage or flux linkage of the corresponding phases. Superscript “a” designates that the resultant vector, $\vec{k}^a$ is written with respect to a-axis. Subscript “s” denotes that, it is a stator variable. $\vec{a}$ and $\vec{a}^2$ are spatial operators such that $\vec{a} = e^{j\frac{2\pi}{3}} = -\frac{1}{2} + j\frac{\sqrt{3}}{2}$ and $\vec{a}^2 = e^{j\frac{4\pi}{3}} = -\frac{1}{2} - j\frac{\sqrt{3}}{2}$ (based on the definition, $e^{j\theta} = \cos\theta + j\sin\theta$). Note that variables are time dependent, but time dependency is not shown in the equations for the sake of simplicity (They are actually written as, $k_{sa}(t),\ k_{sb}(t)\ and\ k_{sc}(t)$). This form in (2.12) with 2/3 normalization factor is used is known as *non-power invariant transformation* in which the power calculated in the transformed system is not the same as in the a,b,c reference frame. In non-power invariant form, the magnitude of the space vector is equal to the amplitude of the sinusoidal steady-state phase variables. The resultant vector is named as *space vector* of the corresponding quantity. It is sometimes named as *complex space vector*. Here it must be noted that, in three-phase systems without a neutral wire, scalar addition of the instantaneous values of these variables yields zero,

$$k_{sa} + k_{sb} + k_{sc} = 0\,. \tag{2.13}$$

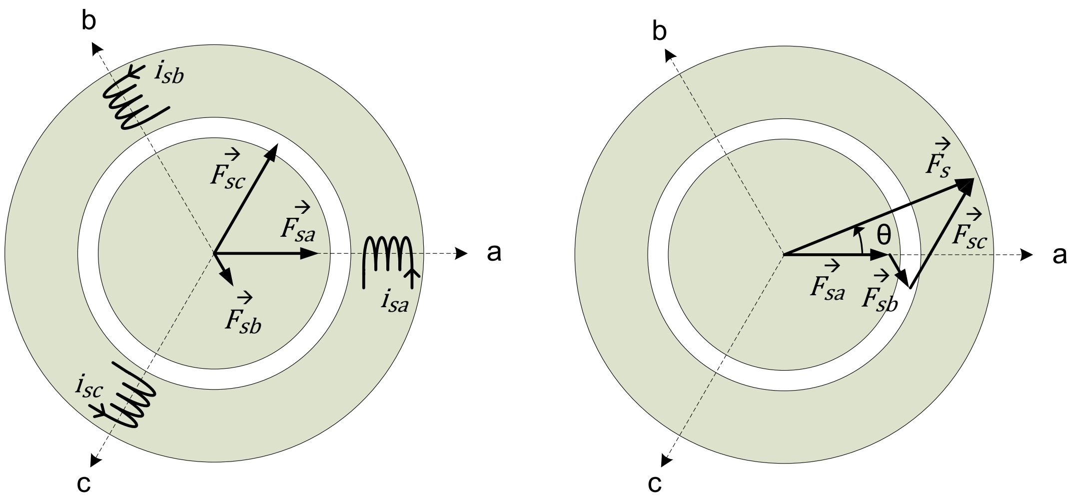

Figure 2.2. Resultant stator mmf represented as a space vector.

As an inverse transformation, phase variables can be obtained by projecting the space vector of that quantity on the corresponding phase axis as demonstrated in Figure 2.3.

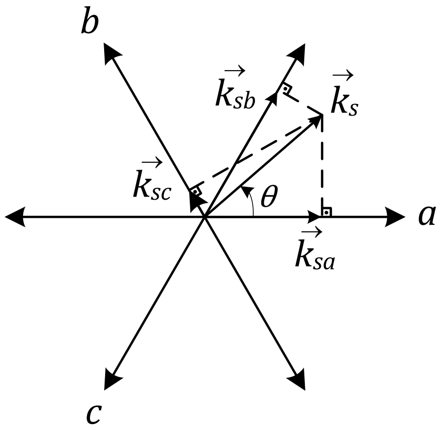

Figure 2.3. Projection of the space vector on the a-, b- and c-axis.

Real part of the complex space vector is equal to the phase-a variable,

$$Re\left(\vec{k}^a\right) = \frac{2}{3}\left[k_{sa} - \frac{k_{sb}}{2} - \frac{k_{sc}}{2}\right] = k_{sa}\ . \tag{2.14}$$

Similarly, phase-b and –c variables can be obtained from complex space vector as,

$$k_b = Re(\vec{a}^2\vec{k}^a) \tag{2.15}$$

$$k_c = Re\left(\vec{a}\vec{k}^a\right)\ . \tag{2.16}$$

Using space vector theory, voltage equation of the stator can be written as:

$$\vec{v}_s^a = R_s\vec{i}_s^a + \frac{d}{dt}\vec{\lambda}_s^a \tag{2.17}$$

where,

$$\vec{v}_s^a = \tfrac{2}{3}[v_{sa} + \vec{a}v_{sb} + \vec{a}^2v_{sc}], \tag{2.18}$$

$$\vec{i}_s^a = \frac{2}{3}[i_{sa} + \vec{a}i_{sb} + \vec{a}^2i_{sc}] \tag{2.19}$$

$$\vec{\lambda}_s^a = \frac{2}{3}[\lambda_{sa} + \vec{a}\lambda_{sb} + \vec{a}^2\lambda_{sc}]\ . \tag{2.20}$$

$\vec{v}_s^a$, $\vec{\imath}_s^a$ and $\vec{\lambda}_s^a$ are the stator voltage, current and flux linkage space vectors respectively. Note that, space vectors are written with respect to the a-axis. Stator flux linkage space vector can be written in terms of phase inductances and current space vector using (2.5)-(2.7),

$$\vec{\lambda}_s^a = \left(L_{ls} + \frac{3}{2}L_{ms}\right)\vec{\imath}_s{}^a + \lambda_{PM}e^{j\theta_r} \, . \tag{2.21}$$

Using (2.21), stator voltage equation (2.17) becomes:

$$\vec{v}_s^a = R_s\vec{\imath}_s^a + \left(L_{ls} + \frac{3}{2}L_{ms}\right)\frac{d}{dt}\vec{\imath}_s^a + \frac{d}{dt}(\lambda_{PM}e^{j\theta_r}) \tag{2.22}$$

using chain rule of differentiation, (2.22) becomes:

$$\vec{v}_s^a = R_s\vec{\imath}_s^a + \left(L_{ls} + \frac{3}{2}L_{ms}\right)\frac{d}{dt}\vec{\imath}_s^a + \lambda_{PM}\frac{d}{dt}\left(e^{j\theta_r}\right) + e^{j\theta_r}\frac{d}{dt}(\lambda_{PM}) \, . \tag{2.23}$$

The magnitude of the flux linkage with the stator phase windings due to the flux produced by the permanent magnets is nearly constant. Variation in rotor temperature alters the rotor flux but, this variation with time is considered to be negligible. Variation depends on the magnet type. For example, flux linkage of a samarium-cobalt magnet decreases by (2-3) % for each 100^0C rise in temperature. For neodymium magnets this variation is (12-13) % and for ceramic magnets 19% [2]. Therefore, the term $\frac{d}{dt}(\lambda_{PM})$ in (2.23) is assumed to be zero, then,

$$\vec{v}_s^a = R_s\vec{\imath}_s^a + \left(L_{ls} + \frac{3}{2}L_{ms}\right)\frac{d}{dt}\vec{\imath}_s^a + jw_r\lambda_{PM}e^{j\theta_r} \tag{2.24}$$

where $w_r = \frac{d\theta_r}{dt}$ is the angular speed of the rotor flux.

2.4 Transformation to a Reference Frame Rotating at an Arbitrary Speed

In the preceding section, the resultant air-gap mmf produced by the three-phase stator windings is replaced by a single mmf space vector, $\overrightarrow{\mathrm{F}_s}$. Let us think a two-phase winding rotating at an angular speed w_x as shown in Figure 2.4. If suitable currents flow through the two-phase windings, they can produce the same resultant air-gap mmf as the stationary three-phase windings produce.

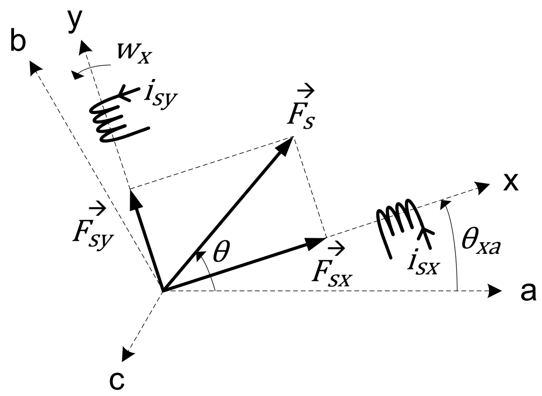

Figure 2.4. mmf space vector, $\overrightarrow{F_s}$ and constituents on x-y axis.

Three-phase stator variables represented along the a-, b- and c-axes can be transformed into variables in orthogonal x- and y-axes by;

$$k_{sx} = \frac{2}{3}[k_{sa}\cos\theta_{xa} + k_{sb}\cos(\theta_{xa} - \frac{2\pi}{3}) + k_{sc}\cos(\theta_{xa} - \frac{4\pi}{3})] \tag{2.25}$$

$$k_{sy} = \frac{2}{3}[-k_{sa}\sin\theta_{xa} - k_{sb}\sin\left(\theta_{xa} - \frac{2\pi}{3}\right) - k_{sc}\sin(\theta_{xa} - \frac{4\pi}{3})] \tag{2.26}$$

where θ_{xa} is the angle between the phase a-axis and x-axis. Inverse transformations are written as,

$$k_{sa} = k_{sx}\cos\theta_{xa} - k_{sy}\sin\theta_{xa} \tag{2.27}$$

$$k_{sb} = k_{sx}\cos\left(\theta_{xa} - \frac{2\pi}{3}\right) - k_{sy}\sin\left(\theta_{xa} - \frac{2\pi}{3}\right) \tag{2.28}$$

$$k_{sc} = k_{sx}\cos\left(\theta_{xa} - \frac{4\pi}{3}\right) - k_{sy}\sin\left(\theta_{xa} - \frac{4\pi}{3}\right). \tag{2.29}$$

Space vectors can be written in complex vector notation,

$$\vec{k}_s^x = k_{sx} + jk_{sy} \tag{2.30}$$

where superscript “x” designates the reference axis. (2.30) is written in polar form as,

$$\vec{k}_s^x = |\vec{k}_s^x| e^{j(\theta - \theta_{xa})}. \tag{2.31}$$

Space vector can also be written with respect to the a-axis,

$$\vec{k}_s^a = |\vec{k}_s^x| e^{j\theta} = \vec{k}_s^x e^{j\theta_{xa}}. \tag{2.32}$$

Equation (2.32) is referred as “*rotation transformation”*. Stator voltage equation (2.17) can be transformed into x-y reference frame with the help of (2.32),

$$\vec{v}_s^x e^{j\theta_{xa}} = R_s \vec{i}_s^x e^{j\theta_{xa}} + e^{j\theta_{xa}} \frac{d}{dt} \vec{\lambda}_s^x + jw_x \vec{\lambda}_s^x e^{j\theta_{xa}} \tag{2.33}$$

where $w_x = \frac{d}{dt}(\theta_{xa})$ is the angular speed of the x-y winding set. Dividing both sides of (2.33) by $e^{j\theta_{xa}}$,

$$\vec{v}_s^x = R_s \vec{i}_s^x + \frac{d}{dt} \vec{\lambda}_s^x + jw_x \vec{\lambda}_s^x . \tag{2.34}$$

Using (2.30), voltages developed in x- and y-windings are written as,

$$v_{sx} = R_s i_{sx} + \frac{d}{dt} \lambda_{sx} - w_x \lambda_{sy} \tag{2.35}$$

$$v_{sy} = R_s i_{sy} + \frac{d}{dt} \lambda_{sy} + w_x \lambda_{sx} . \tag{2.36}$$

Flux linkage equation (2.21), can be transformed into x-y reference frame in a similar manner,

$$\vec{\lambda}_s^x = \left(L_{ls} + \frac{3}{2} L_{ms}\right) \vec{i}_s^x + \lambda_{PM} e^{j(\theta_r - \theta_{xa})} . \tag{2.37}$$

x- and y-winding flux linkages are written as,

$$\lambda_{sx} = \left(L_{ls} + \frac{3}{2}L_{ms}\right) i_{sx} + \lambda_{PM} \cos(\theta_r - \theta_{xa}) \tag{2.38}$$

$$\lambda_{sy} = \left(L_{ls} + \frac{3}{2}L_{ms}\right) i_{sy} + \lambda_{PM} \sin(\theta_r - \theta_{xa}) \, . \tag{2.39}$$

x-y winding set has been chosen arbitrarily with angular speed w_x, thus it is named as *arbitrary reference frame*. In general, three reference frames are used, *stationary reference frame*, *synchronous reference frame* and *rotor reference frame*. For induction machines any one of them can be preferred however, for PMSMs "the rotor frame of reference is chosen because the position of the rotor magnets determines, independently of the stator voltages and currents, the instantaneous induced emfs and subsequently the stator currents and torque of the machine [2]".

Windings in rotor reference frame are generally named as d- and q-windings, which rotate at same angular speed with the rotor flux, w_r. d-axis is aligned with the axis of the flux produced by permanent-magnet as depicted in Figure 2.5.

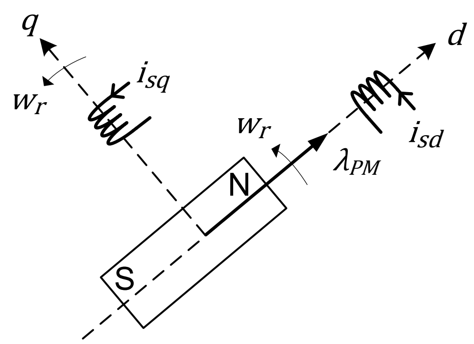

Figure 2.5. d- and q-windings rotating with angular speed of the rotor flux.

d- and q-axis voltage equations (2.35) and (2.36) are written as, (x-axis is named as d-axis and y-axis is named as q-axis),

$$v_{sd} = R_s i_{sd} + \frac{d}{dt}\,\lambda_{sd} - w_r \lambda_{sq} \tag{2.40}$$

$$v_{sq} = R_s i_{sq} + \frac{d}{dt}\,\lambda_{sq} + w_r \lambda_{sd} \tag{2.41}$$

d- and q-axis flux linkage equations (2.38) and (2.39) become,

$$\lambda_{sd} = \left(L_{ls} + \frac{3}{2}L_{ms}\right) i_{sd} + \lambda_{PM} \tag{2.42}$$

$$\lambda_{sq} = \left(L_{ls} + \frac{3}{2}L_{ms}\right) i_{sq}\ . \tag{2.43}$$

Note that, flux linkage equations no more depend on the rotor angle. Inductances appearing in the flux linkage equations are named as direct-axis inductance, L_d and quadrature-axis inductance, L_q; then flux linkage equations can be written as,

$$\lambda_{sd} = L_d i_{sd} + \lambda_{PM} \tag{2.44}$$

$$\lambda_{sq} = L_q i_{sq}\ . \tag{2.45}$$

Substituting (2.44) into (2.40) and (2.45) into (2.41) results in,

$$v_{sd} = R_s i_{sd} + L_d \frac{d}{dt}\ i_{sd} - w_r L_q i_{sq} \tag{2.46}$$

$$v_{sq} = R_s i_{sq} + L_q \frac{d}{dt}\ i_{sq} + w_r L_d i_{sd} + w_r \lambda_{PM} \tag{2.47}$$

where $\frac{d}{dt}\ \lambda_{PM}$ is assumed to be zero. According to these voltage equations, d- and q-winding equivalent circuits in rotor reference frame can be represented as in Figure 2.6.

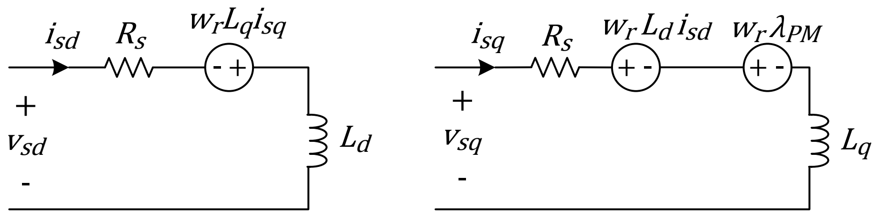

Figure 2.6. d- and q-winding equivalent circuits in rotor reference frame.

The block diagram of the rotor reference frame stator voltage equations is represented as in Figure 2.7 where p is the derivative operator.

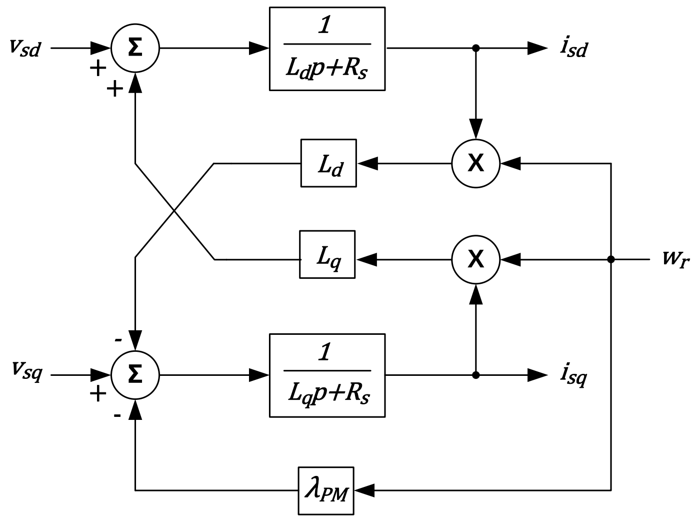

Figure 2.7. Block diagram of stator voltage equations in rotor reference frame.

Block diagram of the stator voltage equations can also be represented as in Figure 2.8, with the help of (2.40), (2.41), (2.44) and (2.45).

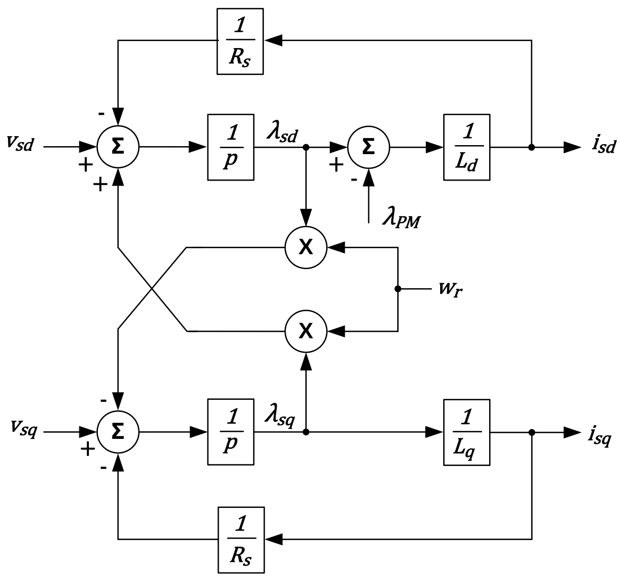

Figure 2.8. Alternative block diagram of stator voltage equations in rotor reference frame.

2.5 Electromagnetic Torque Generation

The electromagnetic power equation in the rotor reference frame is derived in APPENDIX A. The power transferred to the air gap which is generally named as electromechanical power, P_{em} can be written as,

$$P_{em} = \frac{3}{2} w_r \left[\left(L_d - L_q \right) i_{sd} i_{sq} + \lambda_{PM} i_{sq} \right] . \tag{2.48}$$

The mechanical output power is the product of the angular velocity and torque,

$$P_{em} = w_m T_{em} \tag{2.49}$$

where T_{em} is the electromagnetic torque and w_m is the mechanical angular speed of the rotor which is related to electrical angular rotor flux speed, w_r as:

$$w_r = \frac{P}{2} w_m \tag{2.50}$$

where P is the number of poles of the machine. Therefore electromagnetic torque becomes,

$$T_{em} = \frac{3}{2} \frac{P}{2} \left[\left(L_d - L_q \right) i_{sd} i_{sq} + \lambda_{PM} i_{sq} \right] . \tag{2.51}$$

The electromagnetic torque can also be written in terms of flux linkages,

$$T_{em} = \frac{3}{2} \frac{P}{2} \left[\lambda_{sd} i_{sq} - \lambda_{sq} i_{sd} \right] . \tag{2.52}$$

Electromagnetic torque consists of two parts. One of them, $\frac{3}{2}\frac{P}{2}(L_d - L_q) i_{sd} i_{sq}$ is the reluctance torque. Since the surface mounted PMSM is nearly non-salient ($L_d \approx L_q$), reluctance torque cannot be generated. The other part, $\frac{3}{2}\frac{P}{2}\lambda_{PM} I_{sq}$ is the permanent-magnet torque. Therefore electromagnetic torque can be approximated as,

$$T_{em} = \frac{3}{2} \frac{P}{2} \lambda_{PM} i_{sq} . \tag{2.53}$$

2.6 Electromechanical Equations

The acceleration of the equivalent inertia (J_{eq}) is determined by the net torque acting on that inertia,

$$T_{net} = J_{eq}\alpha_m = J_{eq}\frac{d}{dt}w_m = J_{eq}\frac{d^2}{dt^2}\theta_m \tag{2.54}$$

where α_m is the angular acceleration, T_{net} is the net torque on the shaft which can be written as,

$$T_{net} = T_{em} - T_l\,. \tag{2.55}$$

T_l is the load torque which includes torque applied externally on the shaft and the friction and windage torque. θ_m is the mechanical rotor angle which is related to electrical rotor flux angle as defined in (2.8).

J_{eq} is the total moments of inertia of the mechanical system which is the sum of the load inertia, J_l and rotor inertia, J_m;

$$J_{eq} = J_m + J_l\,. \tag{2.56}$$

Complete block diagram of the surface mounted PMSM is represented as in Figure 2.9.

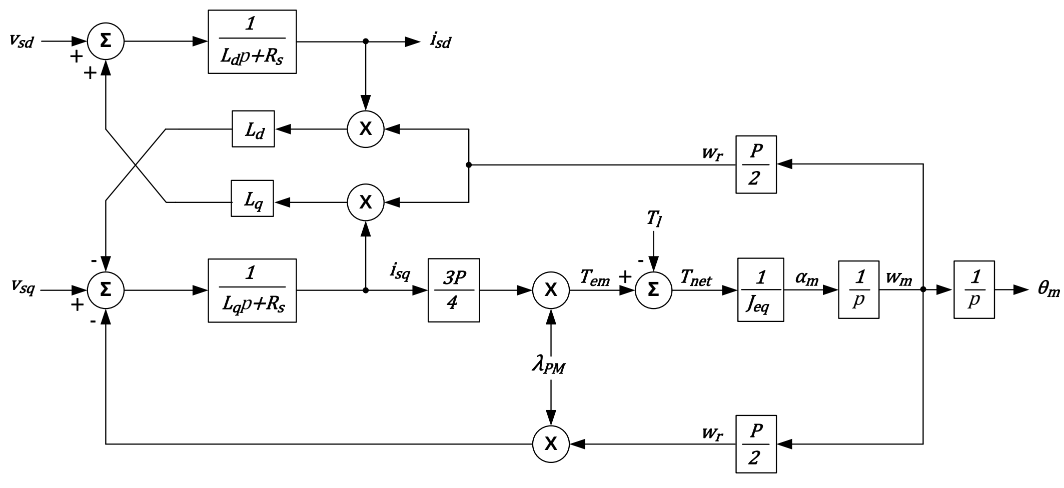

Figure 2.9. Complete block diagram of the surface mounted PMSM in rotor reference frame.

2.7 Torque Angle Control Strategies

Vector diagram of a surface-mounted PMSM in rotor reference frame is shown in Figure 2.10, where θ_r is the electrical angle between the rotor flux and stator phase-a axis. $\emptyset$ is the angle between the stator voltage space vector, $\vec{v}_s$ and current space vector, $\vec{\imath}_s$. It is named as the *power angle*. δ is the angle between rotor flux axis (d-axis) and the stator current space vector, $\vec{\imath}_s$ and it is called as the *torque angle*.

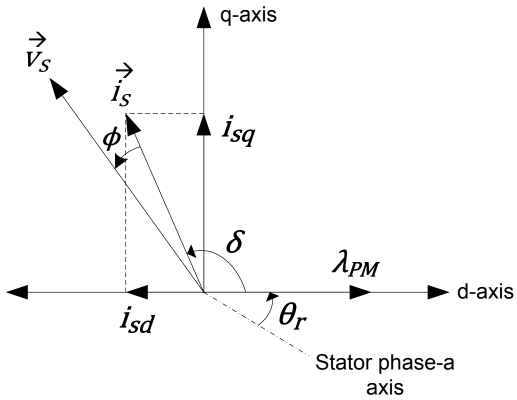

Figure 2.10. Vector diagram of a PMSM in rotor reference frame.

By controlling the torque angle, δ we can adjust some performance characteristics such as power factor, volt-ampere supplied to the machine, maximum achievable speed etc. Some of the torque angle control strategies to be found in the literature are,

- zero direct-axis current control (i.e. $\delta = 90^0$),
- unity power factor control (i.e. $\emptyset = 0^0$),
- constant air gap flux control,
- maximum torque per ampere control and
- flux weakening control (i.e. increasing i_{sd} current component to produce negative mmf with respect to λ_{PM} which reduces the effective net flux in d-axis).

Operations under different torque angle conditions are examined in APPENDIX B.

CHAPTER 3

PWM VOLTAGE-SOURCE INVERTER FOR PMSM SUPPLY

3.1 Introduction

Three-phase ac machine speed and position control require three-phase ac supply with adjustable amplitude and frequency therefore, the ac power line cannot be directly used. For this purpose power converters have been developed. Among the modern power converters, voltage-source inverters (VSIs) are the most widely used circuitries in these applications. A VSI is a circuit that converts the dc voltage into ac voltage with adjustable amplitude and frequency.

Two-level, three-phase VSI is the broadly utilized VSI type for three-phase loads. It consists of six power transistors and anti-parallel diodes as shown in Figure 3.1.

As for power semiconductors, in general, MOSFETs are used in low voltage applications approximately lower than 250 V due to their smaller device voltage drop compared to IGBTs. Since in this thesis, as a dc source a battery of 24 V is used, VSI is constructed with power MOSFETS.

In this chapter, two-level, three-phase VSI is analyzed in detail. A switching scheme, named as space vector pulse width modulation (SVPWM) is investigated.

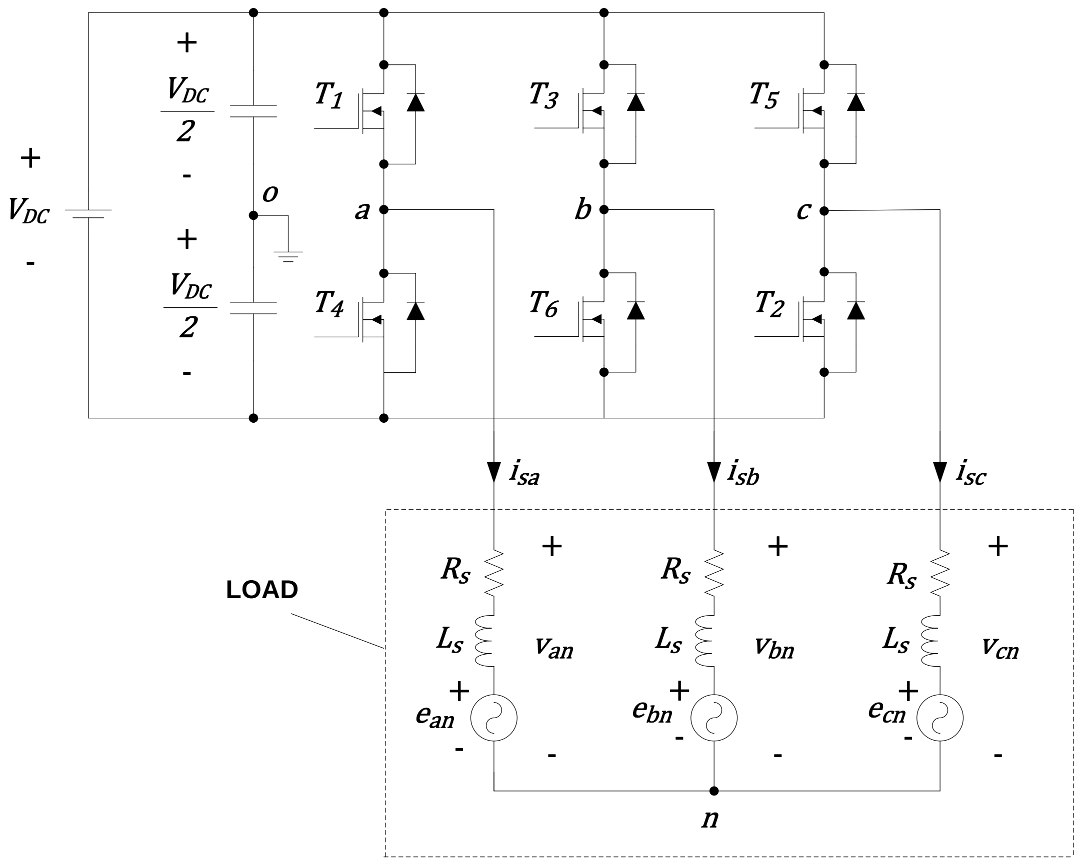

Figure 3.1 Circuit diagram of a two-level three-phase VSI connected to a star connected three-phase machine.

3.2 Two-Level Three-Phase Voltage-Source Inverter

If the power switches are assumed to be ideal, they short the drain terminal to the source terminal if their gates are biased and otherwise, they set open circuit like an ideal switch. Any phase of the three-phase VSI can be connected directly to the positive or negative terminal of the dc-link. However, two switches in one leg of the VSI cannot be in conducting state at the same time in order not to short the dc-link (shoot-through). In agreement with this condition, all possible states of a three-phase two-level VSI can be seen in Figure 3.2.

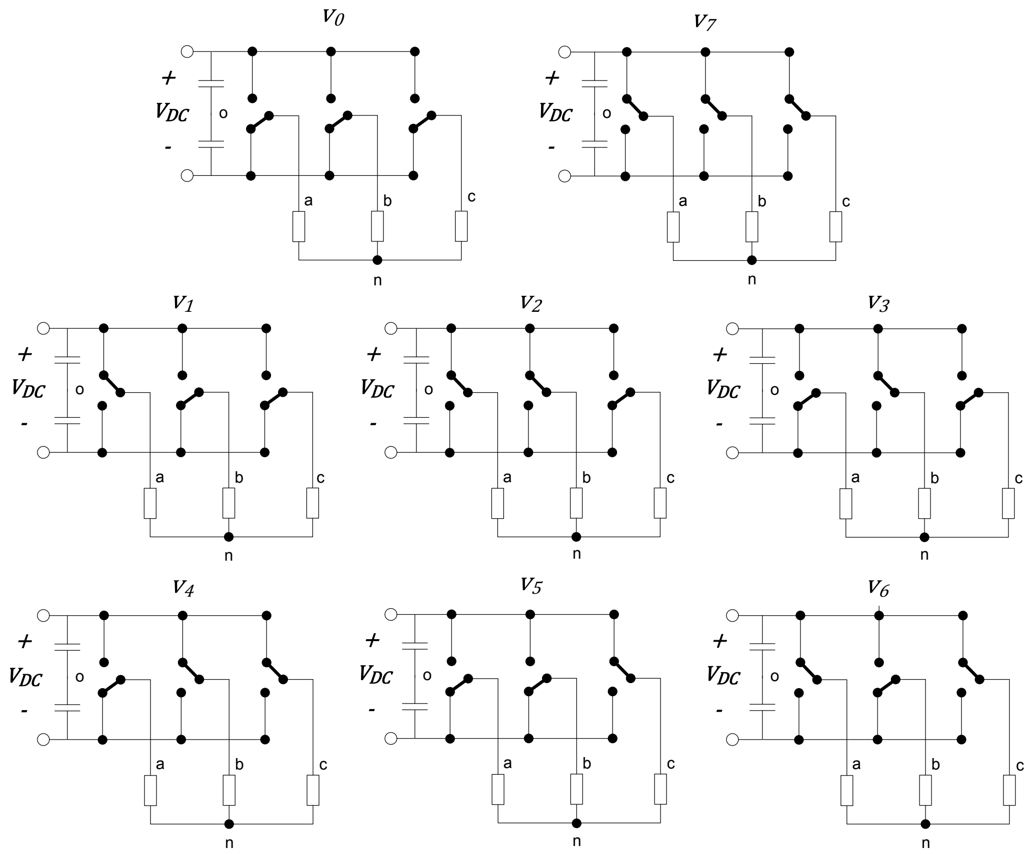

Figure 3.2. Two-level three-phase VSI states.

For every state of the VSI, shown in Figure 3.2, voltages between critical points are tabulated in Table 3.1. Voltage waveforms can be seen in Figure 3.3.

Table 3.1 Different voltage values for different states of the two-level three-phase VSI

q_a	q_b	q_c	V_{ao}	V_{bo}	V_{co}	V_{an}	V_{bn}	V_{cn}	V_{ab}	V_{bc}	V_{ca}	V_{no}
0	0	0	$-V_{DC}/2$	$-V_{DC}/2$	$-V_{DC}/2$	0 V	0 V	0 V	0 V	0 V	0 V	$V_{DC}/2$
1	0	0	$V_{DC}/2$	$-V_{DC}/2$	$-V_{DC}/2$	$2V_{DC}/3$	$-V_{DC}/3$	$-V_{DC}/3$	V_{DC}	0 V	$-V_{DC}$	$V_{DC}/6$
1	1	0	$V_{DC}/2$	$V_{DC}/2$	$-V_{DC}/2$	$V_{DC}/3$	$V_{DC}/3$	$-2V_{DC}/3$	0 V	V_{DC}	$-V_{DC}$	$-V_{DC}/6$
0	1	0	$-V_{DC}/2$	$V_{DC}/2$	$-V_{DC}/2$	$-V_{DC}/3$	$2V_{DC}/3$	$-V_{DC}/3$	$-V_{DC}$	V_{DC}	0 V	$V_{DC}/6$
0	1	1	$-V_{DC}/2$	$V_{DC}/2$	$V_{DC}/2$	$-2V_{DC}/3$	$V_{DC}/3$	$V_{DC}/3$	$-V_{DC}$	0 V	V_{DC}	$-V_{DC}/6$
0	0	1	$-V_{DC}/2$	$-V_{DC}/2$	$V_{DC}/2$	$-V_{DC}/3$	$-V_{DC}/3$	$2V_{DC}/3$	0 V	$-V_{DC}$	V_{DC}	$V_{DC}/6$
1	0	1	$V_{DC}/2$	$-V_{DC}/2$	$V_{DC}/2$	$V_{DC}/3$	$-2V_{DC}/3$	$V_{DC}/3$	V_{DC}	$-V_{DC}$	0 V	$-V_{DC}/6$
1	1	1	$V_{DC}/2$	$V_{DC}/2$	$V_{DC}/2$	0 V	0 V	0 V	0 V	0 V	0 V	$-V_{DC}/2$

Here q_a, q_b, q_c stand for the logic value of the corresponding phase such that, if it is equal to 1, the phase is connected to positive terminal of the dc-link and if it is equal to 0, the phase is connected to negative terminal of the dc-link. v_{ao}, v_{bo} and v_{co} are the voltages between the corresponding phase terminal points (i.e. a, b, and c) and the midpoint of the dc-link. v_{an}, v_{bn} and v_{cn} are the phase-to-neutral voltages, and v_{ab}, v_{bc}, v_{ca} are the line-to-line voltages which can be written as,

$$v_{ab} = v_{an} - v_{bn} \tag{3.1}$$

$$v_{bc} = v_{bn} - v_{cn} \tag{3.2}$$

$$v_{ca} = v_{cn} - v_{an} \,. \tag{3.3}$$

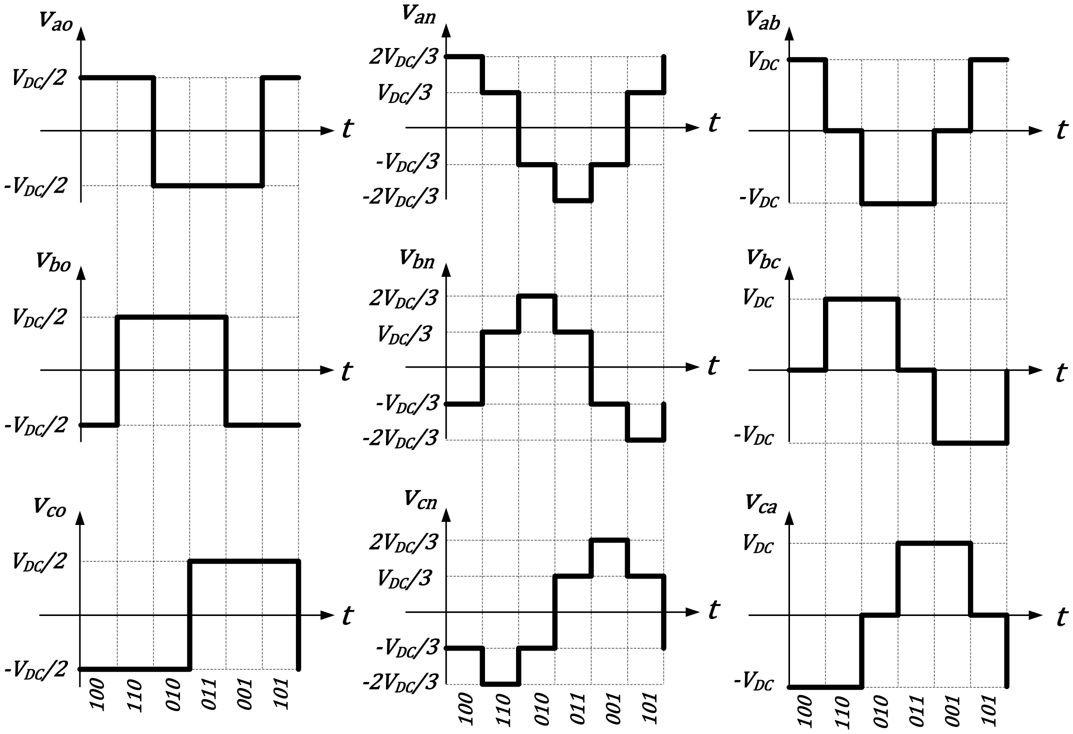

(a) (b) (c)

Figure 3.3. Typical two-level three-phase VSI voltage waveforms: (a) Phase-to-midpoint voltages, (b) Phase-to-neutral voltages, (c) Line-to-line voltages.

Voltage between neutral point of the load and the midpoint of the dc-link is v_{no} which is generally named as *common-mode voltage*. Noting that $v_{an} + v_{bn} + v_{cn} = 0$ and considering the mesh equations for each phase, common-mode voltage is written as in (3.7).

$$v_{ao} = v_{an} + v_{no} \tag{3.4}$$

$$v_{bo} = v_{bn} + v_{no} \tag{3.5}$$

$$v_{co} = v_{cn} + v_{no} \tag{3.6}$$

$$v_{no} = \frac{v_{ao} + v_{bo} + v_{co}}{3}. \tag{3.7}$$

3.3 Space Vector Pulse Width Modulation

2-axis stationary reference frame is named as α-β reference frame (sometimes named as α-β complex plane) where α-axis is aligned with a-axis and β-axis leads the α-axis by π/2 as demonstrated in Figure 3.4.

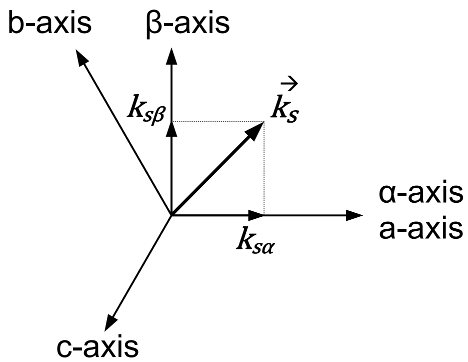

Figure 3.4. Components of the space vector in two-axis stationary reference frame.

By means of reference frame transformations (2.25) and (2.26), 3-phase quantities can be transformed into α-β reference frame. For different states of the VSI, phase-to-neutral voltages given in Table 3.1 can be transformed into α-β reference frame as tabulated in Table 3.2. Voltage space vectors are also given in the table.

Representing these voltages in α-β complex plane yields the diagram shown in Figure 3.5. Each of eight possible VSI states are represented by a vector, $\vec{v}_i$ (*i=0…7*) in the α-β complex plane. Six of them ($\vec{v}_1 \ldots \vec{v}_6$) are the *active vectors* and other two ($\vec{v}_0$ *and* $\vec{v}_7$) are *zero vectors*. All these eight vectors are called as *basic vectors*. Active vectors divide the complex plane into six equal-width sectors. Magnitudes of the active vectors are the same and equal to $\frac{2V_{DC}}{3}$.

Table 3.2 Phase-to-neutral voltages in α-β reference frame for different states of the two-level three-phase VSI

q_a	q_b	q_c	v_α	v_β	$\vec{v}_s^{\alpha}$	Space vector name
0	*0*	*0*	*0*	*0*	*0*	$\vec{v}_0$
1	*0*	*0*	$2V_{DC}/3$	*0*	$(2V_{DC}/3)e^{j0}$	$\vec{v}_1$
1	*1*	*0*	$V_{DC}/3$	$V_{DC}/\sqrt{3}$	$(2V_{DC}/3)e^{j\frac{\pi}{3}}$	$\vec{v}_2$
0	*1*	*0*	$-V_{DC}/3$	$V_{DC}/\sqrt{3}$	$(2V_{DC}/3)e^{j\frac{2\pi}{3}}$	$\vec{v}_3$
0	*1*	*1*	$-2V_{DC}/3$	*0*	$(2V_{DC}/3)e^{j\pi}$	$\vec{v}_4$
0	*0*	*1*	$-V_{DC}/3$	$-V_{DC}/\sqrt{3}$	$(2V_{DC}/3)e^{j\frac{4\pi}{3}}$	$\vec{v}_5$
1	*0*	*1*	$V_{DC}/3$	$-V_{DC}/\sqrt{3}$	$(2V_{DC}/3)e^{j\frac{5\pi}{3}}$	$\vec{v}_6$
1	*1*	*1*	*0*	*0*	*0*	$\vec{v}_7$

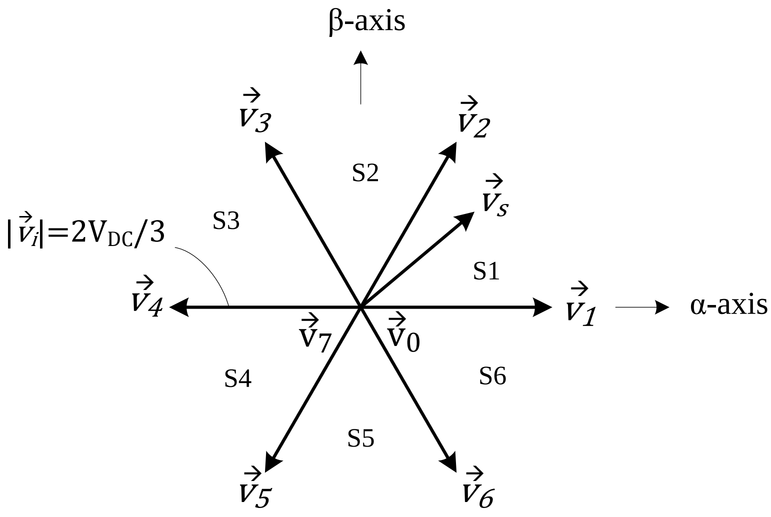

Figure 3.5. Basic voltage space vectors of the three-phase two-level VSI.

By employing basic vectors, the desired voltage space vector $\vec{v}_s$ can be generated with the following objectives,

- maximum utilization of the dc-link,
- maximum possible linear operation,
- minimum switching loss,
- minimum ripple in the phase currents and
- constant switching frequency f_c.

The reason for demanding constant switching frequency is the EMI requirements. Because, for a variable switching frequency, it is troublesome to design an EMI filter.

When the VSI is operated such that, the six active vectors are created in the phases sequentially, phase-to-neutral voltages have the waveform shown in Figure 3.6. This type of operation of the VSI is called as *six-step mode*. From Fourier analysis, when the VSI is operated in six-step mode, phase-to-neutral voltages contain fundamental component of the amplitude V_{m_6-step} which is given by (3.8) for a given dc-link voltage V_{DC}.

$$V_{m\_6-step} = \frac{2V_{DC}}{\pi}. \tag{3.8}$$

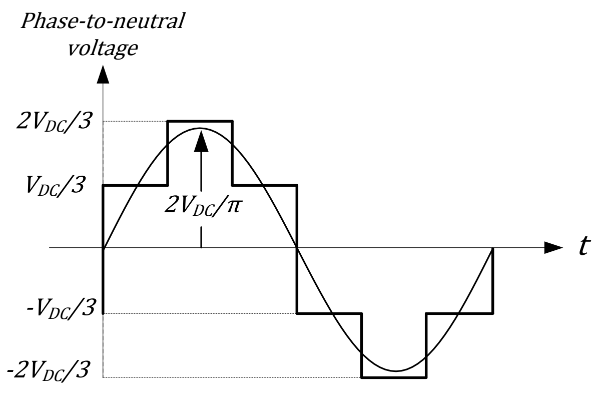

Figure 3.6. Phase-to-neutral voltage and its fundamental component when VSI is operated in six-step mode.

An important parameter in a PWM method is the *modulation index* which is the ratio of the stator voltage space vector amplitude to the six-step mode fundamental phase voltage amplitude. The modulation index, M_i varies between 0 and 1.

$$M_i = \frac{|\vec{v}_s\,|}{V_{m\_6-step}}\,. \tag{3.9}$$

The desired voltage space vector, $\vec{v}_s$ in Figure 3.5 can be approximated by a time average of basic vectors. In the literature, there are various PWM methods to construct the desired voltage vector. Some of them are sinusoidal PWM (SPWM), space sector PWM (SVPWM) and discontinuous PWM (DPWM). They use different basic vectors to construct the desired vector and they behave differently under previously mentioned performance criterions. The major difference of these methods is the selection of the zero vectors.

In sinusoidal PWM method, maximum achievable phase-to-neutral voltage amplitude is $\frac{V_{DC}}{2}$ therefore, the maximum modulation index can be calculated from (3.9) as,

$$M_{i-SPWM} = \frac{V_{DC}/_{2}}{2V_{DC}/_{\pi}} = 0.785\,. \tag{3.10}$$

In space vector PWM method the desired voltage space vector, is generated by using adjoining basic vectors and both of the zero vectors. Maximum attainable phase-to-neutral voltage in this method is $\frac{V_{DC}}{\sqrt{3}}$ and maximum modulation index becomes,

$$M_{i-SVPWM} = \frac{V_{DC}/_{\sqrt{3}}}{2V_{DC}/_{\pi}} = 0.907\,. \tag{3.11}$$

The *linear region* of the VSI is defined as the region where there is a linear relation between reference voltage and output voltage of the VSI. The linearity region for space vector PWM is restricted to a circle where the modulation index is between zero and 0.907 as seen in Figure 3.7. Linearity region of space vector PWM method is approximately %15 larger than the sinusoidal PWM method which means bigger utilization of the dc-bus.

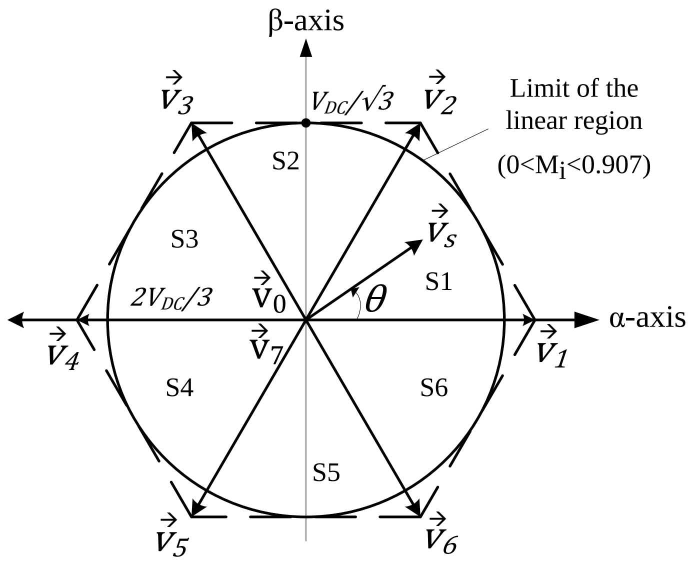

Figure 3.7. Linearity region of the space vector PWM method.

To construct the desired voltage space vector, the sector in which the desired vector lies must be found. Sector number can be decided from the angle between the desired voltage space vector and the α-axis (θ in Figure 3.7).

A voltage space vector, $\vec{v}_s$ in sector-1 can be constructed using basic vectors as shown in Figure 3.8. d_1 and d_2 are the duty factors of the vector $\vec{v}_1$ and vector $\vec{v}_2$ respectively,

$$d_1 = \frac{t_1}{t_s} \tag{3.12}$$

$$d_2 = \frac{t_2}{t_s} \tag{3.13}$$

where t_s is the switching period, t_1 is the total time in which the vector $\vec{v}_1$ is applied and t_2 is the total time in which the vector $\vec{v}_2$ is applied. Defining t_0 as the total time of the zero vectors then,

$$t_1 + t_2 + t_0 = t_s\ . \tag{3.14}$$

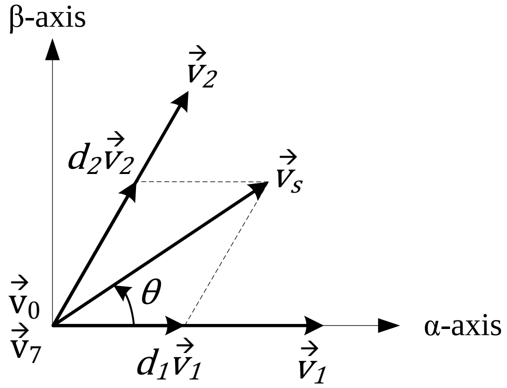

Figure 3.8. Voltage space vector generation using basic vectors.

Using geometric relations, the duty-factor d_2 is obtained as,

$$d_2|\vec{v}_2|\sin\frac{\pi}{3} = |\vec{v}_s|\sin\theta \tag{3.15}$$

$$d_2 = \sqrt{3}\frac{|\vec{v}_s|}{V_{DC}}\sin\theta \tag{3.16}$$

where $|\vec{v}_2| = \frac{2V_{DC}}{3}$. Similarly, duty-factor d_1 can be attained as,

$$d_1|\vec{v}_1| = |\vec{v}_s|\cos\theta - d_2|\vec{v}_2|\cos\frac{\pi}{3} \tag{3.17}$$

$$d_1 = \sqrt{3}\frac{|\vec{v}_s|}{V_{DC}}\sin\left(\frac{\pi}{3} - \theta\right). \tag{3.18}$$

Voltage space vectors in other sectors can be generated in a similar manner. Duty-factor of the zero vectors d_0 is calculated from,

$$d_0 = 1 - d_2 - d_1\,. \tag{3.19}$$

Equations (3.16), (3.18) and (3.19) are applicable to Sinusoidal PWM, space vector PWM and discontinuous PWM methods. However, the selection of the zero vectors is different in these methods. In space vector PWM method, both of the zero vectors are applied for equal time periods as seen in Figure 3.9.

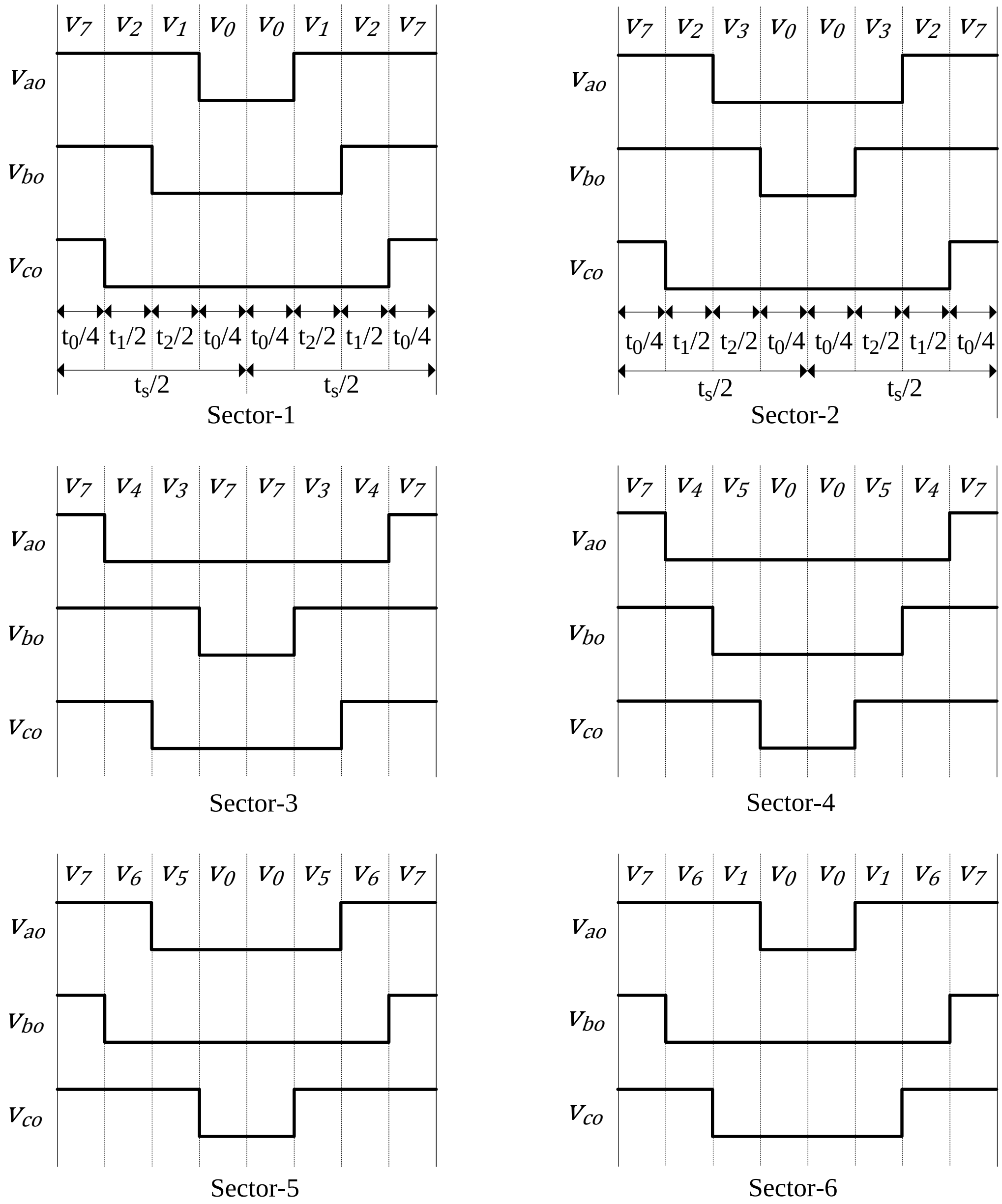

Figure 3.9. Pulse patterns for space vector PWM method.

On-times of the phase-a, -b and –c can be determined according to the sector number and duty factors of the basic vectors. For example, if the voltage space vector lies in sector-1, on-time of phase-c, t_c can be found from,

$$t_c = \frac{t_0}{2} \tag{3.20}$$

where t_0 is the total time of the zero vectors. On-time of phase-b, t_b and on-time of phase-c, t_c becomes,

$$t_b = \frac{t_0}{2} + t_2 \tag{3.21}$$

$$t_a = \frac{t_0}{2} + t_2 + t_1. \tag{3.22}$$

For other sectors, on-times of the phases can calculated in a similar manner.

In this thesis, pulse patterns are created within an FPGA. An up-down counter is generated and for each phase, switching signals are generated by comparing this counter with the pre-calculated control voltages of the corresponding phase. Control voltages, $v_{cont,a}$, $v_{cont,b}$ and $v_{cont,c}$ are determined within the DSP according to on-times of the phases,

$$v_{cont,a} = \frac{t_a}{t_s} v_{tri,max} \tag{3.23}$$

$$v_{cont,b} = \frac{t_b}{t_s} v_{tri,max} \tag{3.24}$$

$$v_{cont,c} = \frac{t_c}{t_s} v_{tri,max} \tag{3.25}$$

where $v_{tri,max}$ is the maximum value of the up-down counter. For sector-1, the triangular carrier signal and switching signals for phase-a, -b and –c are demonstrated in Figure 3.10.

Space vector PWM method corresponds to triangular signal with triplen harmonic zero-sequence signal injection in scalar PWM approach. In Figure 3.11, the modulation and zero-sequence signals for space vector PWM method is seen. Note that, phase-to-neutral voltage waveform is not affected by zero-sequence signal injection.

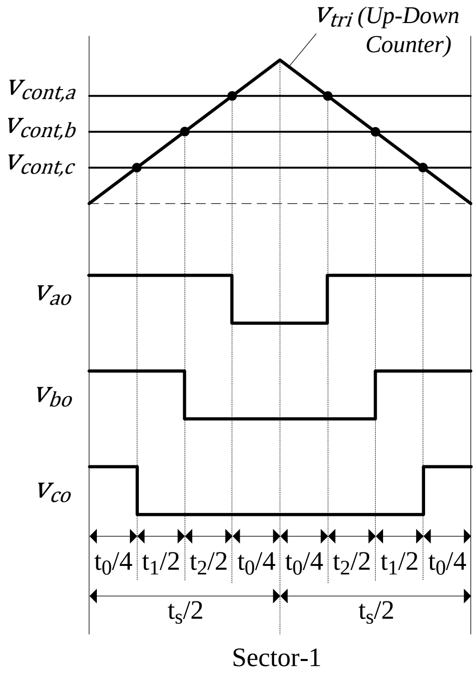

Figure 3.10. Switching signal generation with an up-down counter in the FPGA.

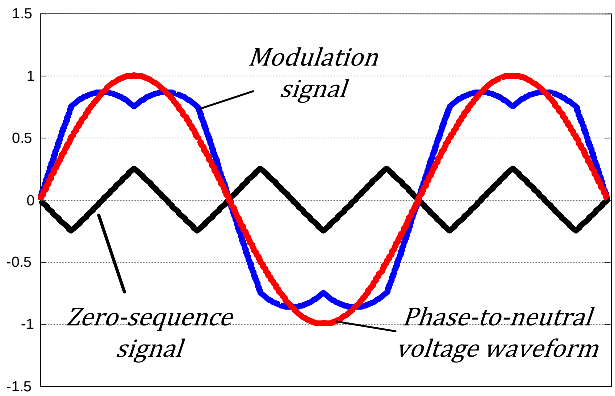

Figure 3.11. Modulation signal, zero sequence signal and phase-to-neutral voltage waveform in space vector PWM method.

Another issue for the PWM-VSI is the harmonic spectrum of the output voltages. This topic has been left out of the scope of this thesis. Detailed information can be found in [18], [19].

CHAPTER 4

CURRENT AND SPEED CONTROL OF PMSM WITH VECTOR CONTROL

4.1 Introduction

Vector control is a well-known and widely-used method which has been implemented in ac drives in order to improve the torque, the speed and the position control performances of ac machines [1]. Vector controlled ac machine can emulate the performance of a separately-excited dc machine for which the torque control is easy and effective. By implementing vector control, the torque output of the ac machine becomes proportional to the current supplied to the armature as in the dc machine.

In this chapter, vector control of the permanent-magnet synchronous machine (PMSM) and current regulation issues are reviewed. Speed control of the machine is discussed. Prior to the vector control, steady-state characteristics of the PMSM should be examined. Steady-state analysis of the surface-mounted PMSM can be found in APPENDIX C.

4.2 Vector Control of PMSM

A vector controller used in an ac machine drive controls both the amplitude and the phase of the current supplied to the machine. The vector control of the current leads to the control of the spatial orientation of the electromagnetic fields in the machine therefore, it is also called as *field-oriented control*. There are three requirements to be fulfilled in the realization of a vector control application;

1. generation of an independently controlled or constant field flux,

2. generation of an independently controlled armature mmf,
3. existence of an independently controlled spatial angle between the field flux and armature mmf axes.

If these three requirements are satisfied, the electromagnetic torque follows the behavior of the armature current; thus the electromagnetic torque can be controlled by controlling the armature current as in the dc machine.

Field flux in a surface-mounted PMSM is produced by permanent-magnets with constant amplitude. Therefore, first requirement of the vector control is satisfied.

If the amplitude and orientation of the stator current space vector are controlled then the second and third requirements are also satisfied.

To control the spatial angle between the mmf and the field flux, the spatial orientation of the field flux must be known. In surface-mounted PMSM, field flux is produced by permanent-magnets and its amplitude is nearly constant. The rotor flux angle (with respect to a stator phase) in synchronous machines can be directly determined from angular measurements on the rotor shaft (for an asynchronous machine, the shaft angle cannot be directly used for the rotor flux angle determination due to the slip speed). A vector control, based on the rotor flux angle, is called as *rotor flux oriented control*.

An important special case is illustrated in Figure B.1 in APPENDIX B where the stator current is on the q-axis ($\delta = 90^0$). This situation is generally referred as *the field orientation*. In this case, mmf and field fluxes are orthogonal to each other and there is no interaction between them.

Vector control of the ac machines is realized by transforming the stationary frame variables to a rotating reference frame and vice versa. In a synchronous machine, rotor rotates at a speed proportional to the frequency of the stator electrical excitation. Therefore, the angle obtained from an angular sensor on the rotor shaft can be used to transform the stator currents from stationary frame into the synchronous frame. Note that, for an asynchronous machine however, the shaft angle measurements cannot be directly used to transform the stator variables into synchronous frame because of the existence of the slip speed.

Magnetic axes used in transformations are depicted in Figure 4.1. α- and β-axes are defined in stationary frame and they are orthogonal to each other. d- and q-axes are orthogonal axes which are rotating at the frequency of the rotor flux. d-axis is chosen as the same axis of the permanent-magnet flux axis.

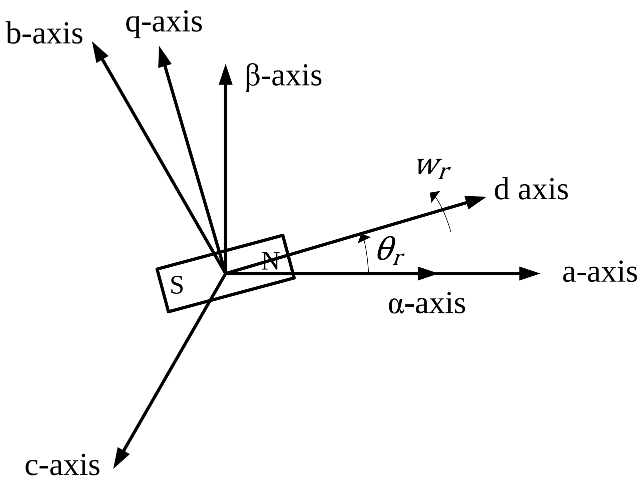

Figure 4.1. Magnetic axes system for the transformations.

Three-phase stator variables, k_{sa}, k_{sb} and k_{sc} can be transformed into two-phase stationary reference frame variables, $k_{s\alpha}$ and $k_{s\beta}$ by means of following relations,

$$k_{s\alpha} = k_{sa} \tag{4.1}$$

$$k_{s\beta} = \frac{1}{\sqrt{3}} k_{sa} + \frac{2}{\sqrt{3}} k_{sb} \ . \tag{4.2}$$

This transformation is called as *phase transformation.* Here, it is assumed that, the three-phase variables sum up to zero.

Similarly, two-phase stationary reference frame variables, $k_{s\alpha}$ and $k_{s\beta}$ can be transformed into synchronously rotating reference frame variables, k_{sd} and k_{sq} by means of following equations,

$$k_{sd} = k_{s\alpha} \cos\theta_r + k_{s\beta} \sin\theta_r \tag{4.3}$$

$$k_{sq} = -k_{s\alpha} \sin\theta_r + k_{s\beta} \cos\theta_r \ . \tag{4.4}$$

This transformation is called as *rotation transformation.* Inverse transformations are given in (4.5)-(4.9).

$$k_{sa} = k_{s\alpha} \tag{4.5}$$

$$k_{sb} = -\frac{1}{2}k_{s\alpha} + \frac{\sqrt{3}}{2}k_{s\beta} \tag{4.6}$$

$$k_{sc} = -k_{sa} - k_{sb} = -\frac{1}{2}k_{s\alpha} - \frac{\sqrt{3}}{2}k_{s\beta} \tag{4.7}$$

$$k_{s\alpha} = k_{sd}\cos\theta_r - k_{sq}\sin\theta_r \tag{4.8}$$

$$k_{s\beta} = k_{sd}\sin\theta_r + k_{sq}\cos\theta_r\ . \tag{4.9}$$

To understand the phase transformation, consider a balanced three-phase excitation,

$$k_{sa} = K\cos w_e t \tag{4.10}$$

$$k_{sb} = K\cos\left(w_e t - \frac{2\pi}{3}\right) \tag{4.11}$$

$$k_{sb} = K\cos\left(w_e t - \frac{4\pi}{3}\right) \tag{4.12}$$

where K is the magnitude of the sinusoidals. Substituting (4.10)-(4.12) into (4.1) and (4.2) yields,

$$k_{s\alpha} = K\cos w_e t \tag{4.13}$$

$$k_{s\beta} = \frac{K}{\sqrt{3}}\cos w_e t + \frac{K}{\sqrt{3}}\cos\left(w_e t - \frac{2\pi}{3}\right) \tag{4.14}$$

Using the relation, $\cos(a-b) = \cos a\cos b + \sin a\sin b$, (4.14) becomes;

$$k_{s\alpha} = K\cos w_e t \tag{4.15}$$

$$k_{s\beta} = K\sin w_e t\ . \tag{4.16}$$

The result shows that, balanced three-phase variables turn into balanced two-phase variables by the phase transformation.

Similarly, to understand how time-varying variables become dc quantities in synchronous reference frame, consider a balanced sinusoidal two-phase stationary reference frame variables such that, $k_{s\alpha} = K\cos w_e t$ and $k_{s\beta} = K\sin w_e t$. Substitution of (4.15) and (4.16) into (4.3) and (4.4), we get k_{sd} as,

$$k_{sd} = K\cos w_e t \cos\theta_r + K\sin w_e t \sin\theta_r \,. \tag{4.17}$$

Using the relation, $\cos(a-b) = \cos a \cos b + \sin a \sin b$, (4.17) becomes:

$$k_{sd} = K\cos(w_e t - \theta_r)\,. \tag{4.18}$$

k_{sq} can be obtained in a similar manner,

$$k_{sq} = K\sin(w_e t - \theta_r)\,. \tag{4.19}$$

The rotor flux angle θ_r, can be written in terms of the excitation frequency w_e,

$$\theta_r = \int_0^t w_e dt + \theta_{r0} \tag{4.20}$$

where θ_{r0} is rotor flux angle at $t = 0$. w_e is constant in steady-state,

$$\theta_r = w_e t + \theta_{r0}\,. \tag{4.21}$$

Substituting (4.21) into (4.18) and (4.19), k_{sd} and k_{sq} become,

$$k_{sd} = K\cos\theta_{r0} = c_1 \tag{4.22}$$

$$k_{sq} = K\sin(-\theta_{r0}) = c_2 \tag{4.23}$$

where c_1 and c_2 are also constants. We can conclude that, time-varying variables become constants in synchronously rotating reference frame.

As seen, time varying three-phase currents turn into time invariant currents in synchronous reference frame. Obtaining time invariant currents (at steady-state operation of the machine) is very useful. In ac machine current control, frequency of the phase currents increases as the machine speed increases. If we do not transform the currents into the synchronous reference frame, rather directly feed them into a controller, the response of the controller degrades as the machine speed increases because of the finite bandwidth of the controllers.

Synchronous frame current component i_{sd} is related with the net flux on the d-axis (according to (2.42)) therefore; the net flux on the d-axis can be controlled by controlling the flux component of the current, i_{sd}. i_{sq} is related with the electromagnetic torque of the machine (according to (2.53)) therefore, electromagnetic torque of the machine can be controlled by controlling the torque component of the current, i_{sq}. Control of these current components is explained in the following section.

4.3 Current Regulation

For the purpose of current control, various regulators are used such as hysteresis band, dead-beat, proportional-integral (P-I) controller etc. Among them, P-I controllers are well-known and widely employed current regulators. P-I current controllers can be implemented either in stationary reference frame or in synchronous reference frame. "The synchronous reference frame proportional-integral (P-I) current regulator has been the industrial standard for current regulation of ac machine drives for more than 20 years [15]". Stator currents in synchronous reference frame become dc quantities so that, the current controller has the ability to regulate the currents over a wide range of machine speeds [16].

Implementation of a synchronous frame P-I current regulator (SFCR) is shown in Figure 4.2. i_{sq}^* is the command for the torque component of the current and i_{sd}^* is the command for the flux component of the current. P-I controller is represented as $(K_p + \frac{K_i}{p})$, where K_p is the proportional gain and K_i is the integral gain and p is the derivative operator. In Figure 4.2, dq to αβ transform stands for (4.8) and (4.9), and abc to dq transform stands for (4.1)-(4.4). Space vector PWM (SVPWM) block calculates the modulation signals as explained in section 3.3. VSI gate signals are generated by comparing modulation signals with a common triangular signal. Rotor angle is measured by means of a shaft encoder and fed to transformations.

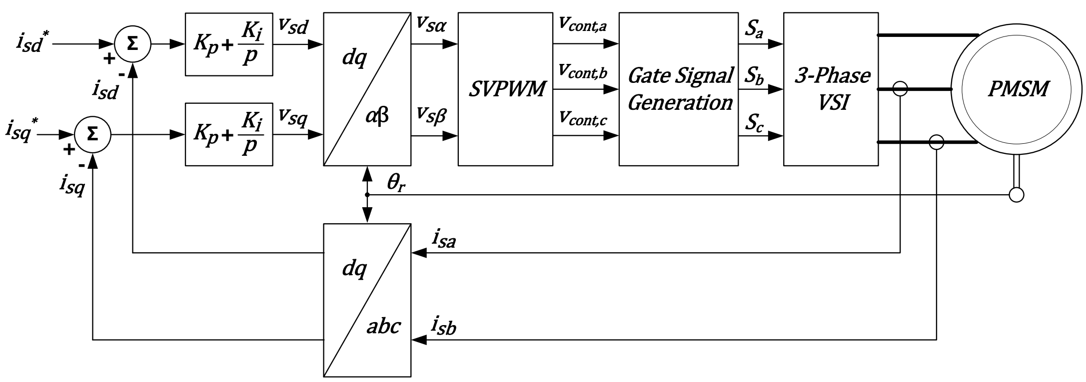

Figure 4.2. Implementation of synchronous frame P-I current regulator.

In three-phase three-wire connected ac supply systems, two phase currents are measured usually because, three-phase currents sum up to zero thus the third phase current can be obtained from the other two. However, in case of a significant current measurement error, it is better to measure all three-phase currents. All current sensors have offset error, gain error and a certain amount of nonlinearity. These erroneous measurements cause time variations, i.e. ripples in the transformed current components i_{sd} and i_{sq}. It has been shown that, three phase current measurement has lower ripple amplitude than two phase current measurement [6], [30].

Flux component of the current, i_{sd} is commanded to be zero as in Figure 4.3. It is commanded other than zero when a torque angle control strategy such as flux weakening control or unity power factor control is implemented. The command for the torque component of the current, i_{sq}^* is usually the output of the speed controller. A rate of change limiter on the current command is necessary to prevent the drastic build up of current error which can cause excessive overshoot. Limit for the rate of change for the current can be determined by considering machine time-constant and VSI voltage and current limits. Another reason for excessive overshoot is the *integral windup* which refers to the situation in a P-I controller where a large change in the reference signal occurs and the integral term accumulates a significant error during the rise. Accumulated error causes significant overshoot. This problem can be solved by disabling the integral function when the output of the controller saturates. This method is called as *integral anti-windup*.

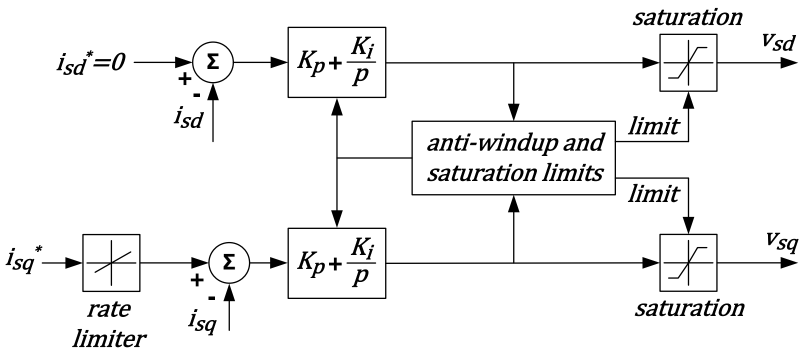

Figure 4.3. Synchronous frame P-I current regulator with zero direct current command and integral anti-windup.

The anti-windup action can be determined from VSI voltage limit, which depends on the switching method. For SVPWM method, limit of the VSI can be decided from (4.24).

Saturation limits for d- and q-axes are calculated such that the orientation of the voltage space vector is preserved.

$$\sqrt{{v_{sq}}^2 + {v_{sd}}^2} \leq \frac{V_{DC}}{\sqrt{3}}. \tag{4.24}$$

4.4 Speed Regulation

Speed control of the PMSM is usually implemented with P-I controllers as demonstrated in Figure 4.4 where K_{ps} is the proportional gain and K_{is} is the integral gain.

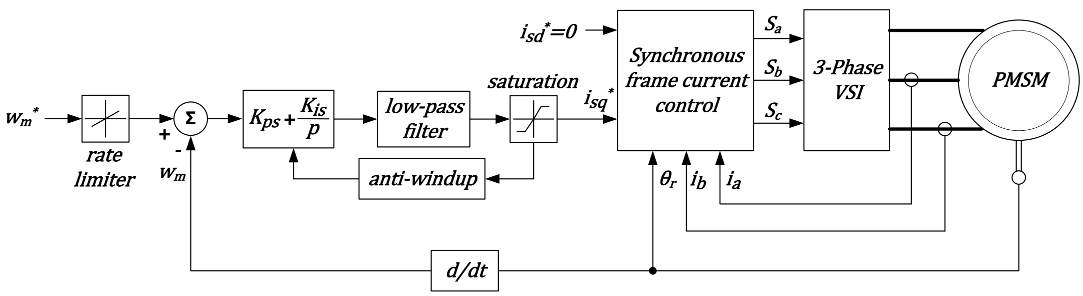

Figure 4.4. Implementation of the speed control loop.

Speed controller uses the speed command w_m^* as reference signal and mechanical speed of the machine w_m as feedback. Speed feedback can be obtained via a speed sensor or it can be derived from the rotor angle. The rate of change of the speed command must be limited to prevent excessive overshoot. The limitation on the rate of change of the speed corresponds to the limit on the acceleration. The bounds on the acceleration are determined by the maximum generated torque capability of the drive, maximum load torque and total inertia of the drive. Low-pass filtering is necessary for the current command to filter components at frequencies higher than the bandwidth of the current controller. A saturation block must be inserted at the input of the current command in order to limit the current command with the maximum current capability of the VSI and machine system. As explained in the current regulation part, when the output of the controller saturates, the integral action in the P-I controller must be disabled (integral anti-windup).

CHAPTER 5

ANALYSIS AND IMPROVEMENT OF TORQUE AND SPEED CONTROL PERFORMANCE OF PMSM DRIVE

5.1 Introduction

The output voltage of the VSI is distorted due to non-ideal behavior of the power switches. Effect of the nonideality of the VSI on the phase voltage and current is examined and a method, namely as volt-second, to compensate this distortion is presented in this chapter.

Frequency dependent couplings in the synchronous frame model of the PMSM are analyzed. Decoupling method to improve the current control performance is explained.

To increase the disturbance rejection capability of the speed control, a load torque estimator is designed. The angular acceleration required for load torque estimation is extracted through a Kalman filter from noisy velocity measurements.

5.2 Effect of VSI on Torque Control Performance

At the beginning, nonideal characteristics of the VSI are examined then, volt-second compensation method is described in this section.

5.2.1 Nonideal Characteristic of the VSI

In CHAPTER 3, the output voltages of the VSI are examined, assuming ideal power switches. However, in practice, output voltage of the VSI is distorted due to some non-ideal behavior of the power switches that means; actual waveforms deviate from the waveforms given in Figure 3.3. Nonideal characteristics cause a nonlinear relation between desired output voltage (reference voltage) and actual output voltage of the VSI. The source of nonlinearities can be listed as,

- blanking-time inserted before turning on the switches to prevent short circuit on the dc-link,
- finite turn-on and turn-off time of the switches,
- voltage drop on the switches,
- ripples on the dc-link voltage.

One leg of a three-phase VSI is shown in Figure 5.1. Load is a three-phase ac machine which is not depicted in the figure. V_{DC} is the dc-link voltage; i_a is the phase current; S_1 and S_4 are the ideal gate signals. S_1' and S_4' are the gate signals involving inserted dead-time, t_d. Ideal gate pulse patterns can be seen in Figure 5.2(a) where t_a represents the desired on-time of the corresponding phase. Dead-time insertion, delays the rising edge of the gate pulses by an amount of t_d as demonstrated in Figure 5.2(b). Output voltage of the VSI is v_{ao} which is named as *phase-to-midpoint voltage*.

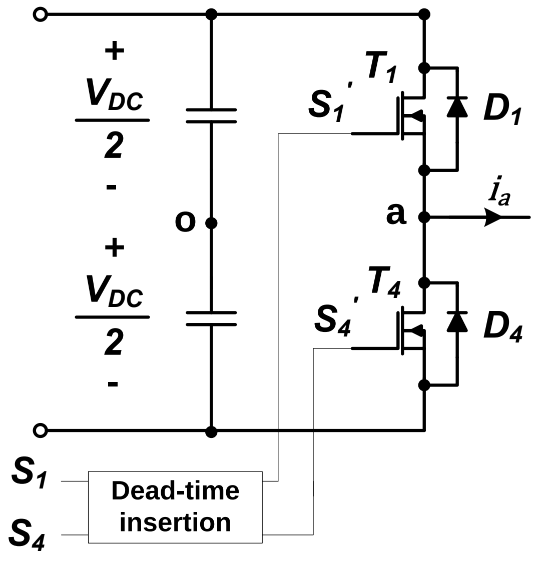

Figure 5.1. Circuit diagram of one leg of the three-phase VSI.

When both of the power switches on the same leg in a two-level VSI are in conducting state, the dc-link is shorted. This phenomenon is called as *shoot-through* of the dc-link. This causes burning out the power switches in that leg of VSI. Turn-on and turn-off of the two power switches in one leg of the VSI lasts a finite duration. Therefore, to avoid a short circuit in the dc-link, following turning-off one of the power switches in one leg of the VSI, a finite time must be inserted before turning-on the other power switch on the same leg. This period is generally called as *dead-time* or *blanking-time*. Duration of this period depends on the turn-on and turn-off times of the power switches; thereby gate capacitance of the power switch and the size of the gate resistor. The duration expands with increasing power rating of the power switches. During dead-time both of the switches are off. Since the load is inductive, it acts like a current source forcing one of the diodes to conduct according to the direction of the phase current. Therefore, during dead-time, the output voltage depends on the diode which is conducting and thus, it depends on the direction of the phase current. This causes a momentary loss of control of the output voltage.

Phase current from VSI to the load is defined as positive current, while the reverse direction is marked as negative. During dead-time, if i_a is positive, then diode D_4 is conducting; and if i_a is negative, then D_1 is conducting. When compared to ideal output voltage, there is a gain for negative current and loss for positive current in the actual output voltage as depicted in Figure 5.2(c) and Figure 5.2(d).

Phase-to-midpoint voltage v_{ao}, is also affected by turn-on/off times of the power switches. Turn-on time t_{on}, includes the delays of gating circuitry and the turn-on of the power switch. Turn-off time t_{off}, is defined in a similar manner. Turn-on time affects the phase-to-midpoint voltage just like the dead-time does. However, turn-off time acts the opposite way such that, there will be gain in the average voltage due to turn-off time when there is a loss due to dead-time and vice versa [27]. Therefore, an effective time which indicates the output voltage distortion can be defined as,

$$\Delta t = t_d + t_{on} - t_{off}. \tag{5.1}$$

Another source of nonlinearity is the voltage drop on the power switches. For a positive phase current, namely $i_a > 0$, when the top switch in one leg of the VSI is “on” and the bottom is “off”; the phase-to-midpoint voltage v_{ao} is equal to $(V_{DC}/2 - V_{DS})$ as shown in Figure 5.3(a). V_{DS} is the drain-source on-state voltage drop on the power MOSFET which can be written as,

$$V_{DS} = R_{DS}|i_a| \tag{5.1}$$

where R_{DS} is the on-state resistance of the power MOSFET. Similarly, for a negative phase current ($i_a < 0$) when the top switch is "on" and the bottom is "off"; the phase-to-midpoint voltage v_{ao} is equal to $(V_{DC}/2 + V_{DS})$ as seen in Figure 5.3(b). During the dead-time both switches are "off", and for a positive current, D_4 is conducting thus, phase-to-midpoint voltage v_{ao} is equal to $(-V_{DC}/2 - V_D)$ as demonstrated in Figure 5.3(e). V_D is the forward voltage of the diode which can be written as,

$$V_D = V_{D0} + R_D|i_a| \tag{5.2}$$

where V_{D0} is the threshold voltage for the diode and R_D is the on-state resistance of the diode [25]. In a similar manner, for other switching conditions and current directions, paths of the current in the VSI are demonstrated in Figure 5.3 and the phase-to-midpoint voltage is as tabulated in Table 5.1.

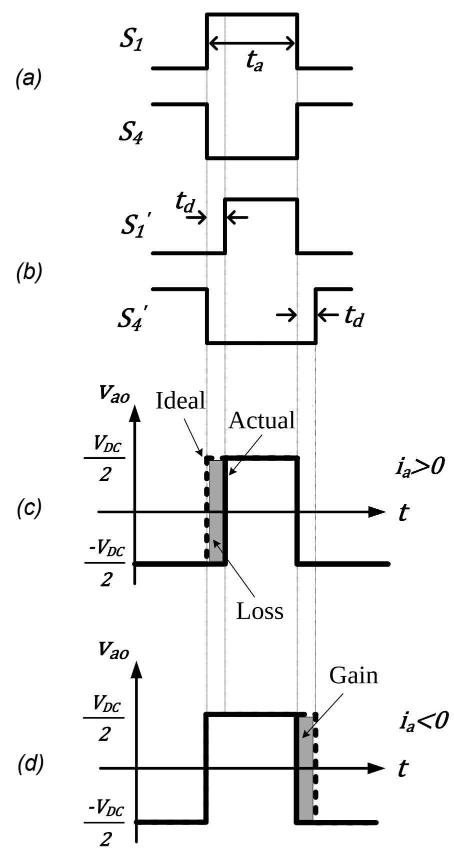

Figure 5.2. Effect of dead-time on the VSI output voltage waveform. (a) Ideal gate signals. (b) Gate signals with dead-time. (c) Phase-to-midpoint voltage for positive current. (d) Phase-to-midpoint voltage for negative current.

Table 5.1 MOSFET Inverter Output Voltage for Different Switching Conditions and Current Directions

	$i_a>0$	$i_a<0$
T_1: ON T_4: OFF	$v_{ao} = V_{DC}/2 - V_{DS}$	$v_{ao} = V_{DC}/2 + V_{DS}$
T_1: OFF T_4: ON	$v_{ao} = -V_{DC}/2 - V_{DS}$	$v_{ao} = -V_{DC}/2 + V_{DS}$
T_1: OFF T_4: OFF	$v_{ao} = -V_{DC}/2 - V_D$	$v_{ao} = V_{DC}/2 + V_D$

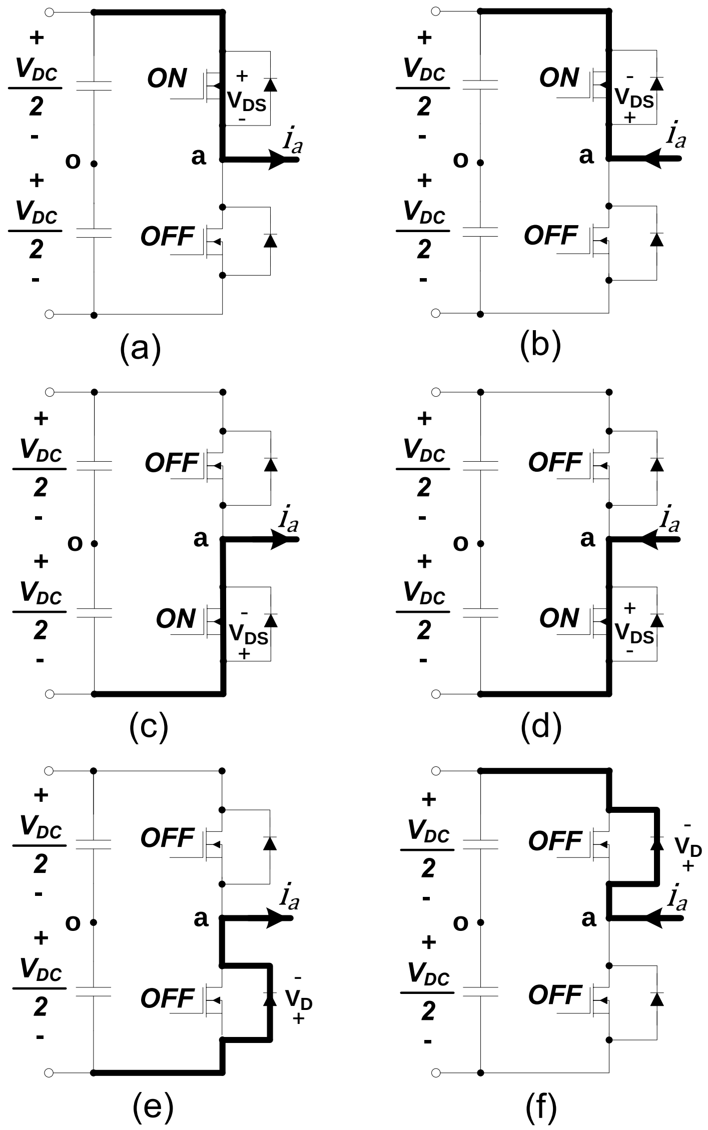

Figure 5.3 Path of the current for different switching conditions and current directions, (a) T_1: ON, T_4: OFF, $i_a>0$. (b) T_1: ON, T_4: OFF, $i_a<0$. (c) T_1: OFF, T_4: ON, $i_a >0$. (d) T_1: OFF, T_4: ON, $i_a <0$. (e) T_1: OFF, T_4: OFF, $i_a >0$. (f) T_1: OFF, T_4: OFF, $i_a >0$.

Effect of the nonideal characteristics (dead-time, turn-on/off times, voltage drop) on the output voltage of the VSI is demonstrated in Figure 5.4. In this figure, the thicker line is the desired phase-to-midpoint voltage and the thinner line is the actual phase-to-midpoint voltage. The deviation of the actual voltage from the ideal one is clearly seen.

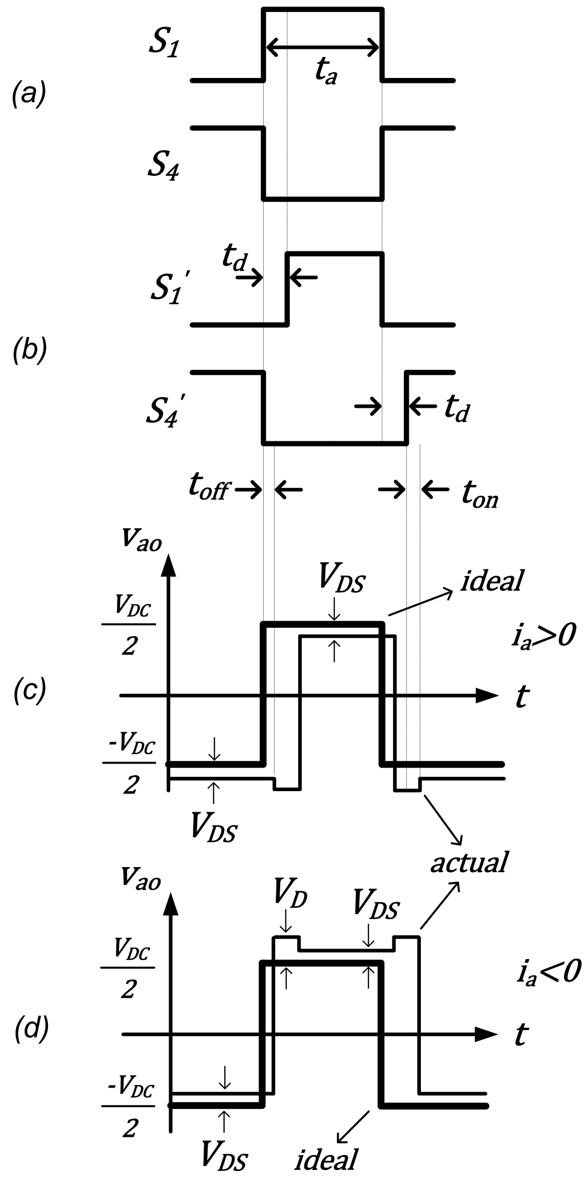

Figure 5.4. Gate pulse patterns and VSI output voltage for MOSFET inverter, (a) Ideal gate pulse patterns. (b) Gate pulse patterns with dead-time. (c) Ideal (thicker signal) and real (thinner) output voltages for positive phase current. (d) Ideal (thicker signal) and real (thinner signal) output voltages for negative phase current.

If the actual waveforms are examined, it can be noted that, in a VSI with MOSFET switches, diodes conduct only in dead-time period. For an IGBT however, inverter diodes conduct for the dead-time period and also for periods when the IGBT in parallel is reverse biased. MOSFETs conduct current when they are gated and reverse biased (acting like a resistor) while IGBT cannot (acting like a diode). Therefore, current flows through the MOSFET as in Figure 5.3 (b) and (c), not through the diode as it was the case in an IGBT inverter.

It is worth to mention that, if the current reaches to zero during the dead-time period, the instantaneous output voltage $v_{ao}(t)$, from current zero onward, is equal to back-emf of the corresponding phase where back-emf is either e_{an} or e_{bn} or e_{cn} for phase-a, -b and -c respectively [29], [33], [28]. This is known as *zero-current clamping* phenomenon.

In summary, considering the effects of non-idealities associated with the output voltage waveforms, VSI exhibits a non-linear characteristic due to the inserted blanking-time, finite turn-on and turn-off time of the power switches, switch voltage drop and ripple on the dc-link. The distorted output voltage of the VSI give rise to 6n±1 (n: 1, 2...) harmonics on the phase current waveforms [10], [24], [30]. These harmonics in stationary frame correspond to sixth harmonic in the synchronous frame [37] so generated torque is also distorted. This distortion is more severe at low speed operation of the machine and it increases with increasing switching frequency [20], [30].

In practice, there can be ripple components in dc-link. This ripple content directly affects the inverter output voltage and therefore affects the phase currents and the generated torque. In order to minimize this effect, bigger dc-link capacitance can be used however, it adds to the cost and volume of the design. Another solution to this problem is measuring the dc-link voltage and adjusting the switching signals accordingly.

5.2.2 Volt-Second Method to Compensate the Nonideal Characteristics of the VSI

Distorted output voltage of the VSI give rise to 6n±1 (n: 1, 2...) harmonics on the electromagnetic torque. Especially in low speed operation, these harmonics on the electromagnetic torque can be within the bandwidth of the drive and can cause speed fluctuations.

The nonlinearity of the VSI can be interpreted as a disturbance in the electric drive system. In a current regulated drive system, current regulator tries to reject the effects of disturbances thus, tries to correct the distortions on the current [24]. However, the current regulator has a finite bandwidth i.e. it cannot fully suppress the harmonics caused by the nonideal VSI. In order to increase the bandwidth of the SFCR, proportional and integral gains in the P-I controllers need to be increased. However, in practice these gains cannot be increased indefinitely since, this also causes sustained oscillations and sensor noise amplification.

To handle the distortion caused by VSI, a compensation algorithm should be used. It depends on modifying the reference (commanded) voltage so that, on the output of the VSI (with the error voltage introduced by the VSI) the desired average voltage is obtained.

Average phase-to-midpoint voltage of the VSI over one PWM carrier period, $\overline{v_{ao}}$ is attained by calculating the area under the actual voltage waveforms in Figure 5.4(c) and (d),

$$\overline{v_{ao}} = \left[\frac{t_a}{t_s} - \frac{1}{2}\right] V_{DC} - \left[\frac{\Delta t}{t_s}[V_{DC} - 2V_{DS} + 2V_D] + V_{DS}\right] sgn(i_a) \tag{5.3}$$

where t_s is the PWM carrier period and $sgn(.)$ is the sign function defined as,

$$sgn(i_a) = \begin{cases} sgn(i_a) = 1 \; if \; i_a > 0 \\ sgn(i_a) = 0 \; if \; i_a < 0 \end{cases} . \tag{5.4}$$

Substituting (5.1) and (5.2) into (5.3) we obtain,

$$\overline{v_{ao}} = \left[\frac{t_a}{t_s} - \frac{1}{2}\right] V_{DC} - \left[\left(1 - \frac{2\Delta t}{t_s}\right) R_{DS} + \frac{2\Delta t}{t_s} R_D\right] i_a - \frac{\Delta t}{t_s}[V_{DC} + 2V_{D0}] sgn(i_a) \tag{5.5}$$

where the relation $|i_a| sgn(i_a) = i_a$ is used. Average phase-to-midpoint voltages, $\overline{v_{bo}}$ and $\overline{v_{co}}$ for phase-b and –c respectively, can be obtained in a similar manner,

$$\overline{v_{bo}} = \left[\frac{t_b}{t_s} - \frac{1}{2}\right] V_{DC} - \left[\left(1 - \frac{2\Delta t}{t_s}\right) R_{DS} + \frac{2\Delta t}{t_s} R_D\right] i_b - \frac{\Delta t}{t_s}[V_{DC} + 2V_{D0}] sgn(i_b) \tag{5.6}$$

$$\overline{v_{co}} = \left[\frac{t_c}{t_s} - \frac{1}{2}\right] V_{DC} - \left[\left(1 - \frac{2\Delta t}{t_s}\right) R_{DS} + \frac{2\Delta t}{t_s} R_D\right] i_c - \frac{\Delta t}{t_s}[V_{DC} + 2V_{D0}] sgn(i_c) \tag{5.7}$$

where t_b and t_c are the commanded on-time durations for phase-b and –c. In a three-phase, three-wire connected and balanced load, using (3.4)-(3.7), average phase-to-neutral voltage for phase-a can be written as,

$$\overline{v_{an}} = \frac{2\overline{v_{ao}} - \overline{v_{bo}} - \overline{v_{co}}}{3}$$

$$= \left[\frac{2t_a - t_b - t_c}{3t_s}\right] V_{DC} - M_1 i_a - \frac{M_2}{3}[2sgn(i_a) - sgn(i_b) - sgn(i_c)] \qquad (5.8)$$

i_b and i_c are the phase currents for phase-b and -c respectively; and M_1 and M_2 are the intermediate variables defined as:

$$M_1 = \left[\left(1 - \frac{2\Delta t}{t_s}\right) R_{DS} + \frac{2\Delta t}{t_s} R_D\right] \qquad (5.9)$$

$$M_2 = \frac{\Delta t}{t_s}[V_{DC} + 2V_{D0}]. \qquad (5.10)$$

Commanded on-time durations can be represented as,

$$t_a = t_a^* + t_{com} sgn(i_a) \qquad (5.11)$$

where t_a^* is the desired on-time and t_{com} is the compensation time. Similar expressions can be written for other phases,

$$t_b = t_b^* + t_{com} sgn(i_b) \qquad (5.12)$$

$$t_c = t_c^* + t_{com} sgn(i_c)\,. \qquad (5.13)$$

Substituting (5.11)-(5.13) into (5.8),

$$\overline{v_{an}} = \left[\frac{2t_a^* - t_b^* - t_c^*}{3t_s}\right] V_{DC} - M_1 i_a$$

$$- \left[\frac{t_{com} V_{DC} - M_2}{3}\right] [2sgn(i_a) - sgn(i_b) - sgn(i_c)]\,. \qquad (5.14)$$

From (5.14), it can be concluded that, resistive voltage drops (here M_1) can be treated as a part of the phase resistance. Therefore, only the third term on the right hand side of (5.14) is the distortion voltage from the VSI which should be minimized by adjusting the compensation time as,

$$t_{com} = \Delta t \left[\frac{V_{DC} + 2V_{D0}}{V_{DC}}\right]. \tag{5.15}$$

Following the calculation of the compensation time, determination of the current directions is needed for (5.11)-(5.13). Current transducers can be used for this purpose however, when the phase current is close to zero, current polarity detection is quite difficult with a current transducer because of the switching ripple on the current waveform.

If the projection of the current space vector into phase axes given in Figure 2.3 is examined, it can be said that, current polarities can be determined from the current space vector angle. For example, if the current space vector is in the region where angle θ is between -30^0 and 30^0 then phase-a current is positive, phase-b current is negative and phase-c current is negative. For other regions, polarities of the phase currents are demonstrated in Figure 5.5 and tabulated in Table 5.2.

Current space vector angle θ is the sum of the torque angle δ and rotor angle θ_r as depicted in Figure 2.10. Rotor angle θ_r is measured through a position sensor and torque angle δ is already known for field orientation. When the current space vector is employed for current polarity detection, the switching ripple problems encountered in current transducer utilization are overcame.

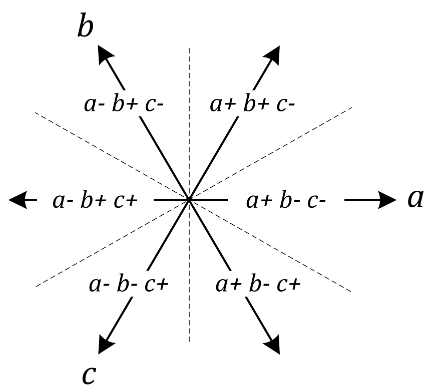

Figure 5.5. Phase current polarities for different current space vector angles.

Implementation of the VSI nonlinearity compensation algorithm within the current loop is shown in Figure 5.6. Compensation block uses dead-time, turn-on/off times, switch voltage drop, torque angle information and rotor angle information. It calculates the compensation times for all phases, according to these parameters and sensor feedbacks. Compensation times are added to the desired on-time durations.

If the estimated parameters match with the actual values then the nonlinear effect of the VSI can be cancelled with the modified desired on-time. When the estimated parameters deviate from the actual values, performance of the compensation algorithm degrades.

Table 5.2 Determination of current directions according to space vector angle

Current space vector angle	$sgn(i_a)$	$sgn(i_b)$	$sgn(i_c)$
$-30^0 < \theta < 30^0$	1	-1	-1
$30^0 < \theta < 90^0$	1	1	-1
$90^0 < \theta < 150^0$	-1	1	-1
$150^0 < \theta < 210^0$	-1	1	1
$210^0 < \theta < 270^0$	-1	-1	1
$270^0 < \theta < 330^0$	1	-1	1

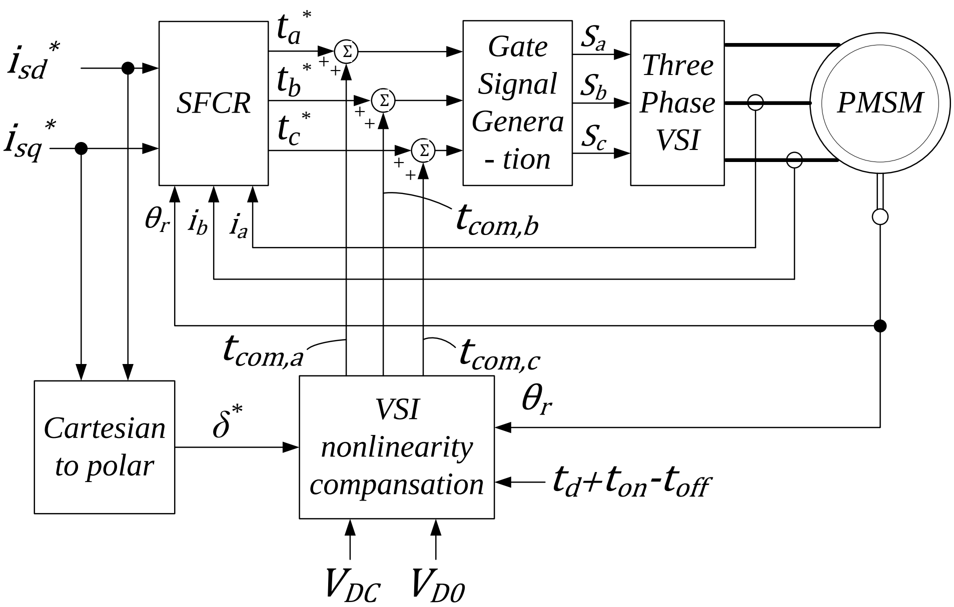

Figure 5.6. Implementation of the VSI nonlinearity compensation algorithm in a synchronous frame current regulator (SFCR) drive.

5.3 Effect of Coupled Variables on Torque Control Performance

In this section, frequency dependent couplings of the d- and q- axes variables in the synchronous frame model of the PMSM are analyzed. Then, decoupling method for these couplings to increase the current regulation performance is presented.

5.3.1 Analysis of the Coupled Variables in the Synchronous Frame Model of the PMSM

Block diagram of the synchronous frame P-I current controlled PWM-VSI fed PMSM drive in s-domain can be seen in Figure 5.7. T_p is the time-constant on the d- and q-axes. Since the machine is non-salient, i.e. $L_d = L_q$, time-constants are the same for d- and q-axes,

$$T_p = \frac{L_d}{R_s} = \frac{L_q}{R_s} . \tag{5.16}$$

Therefore, same controller parameters are used for both axes. T_c is the time-constant of the controller defined as,

$$T_c = \frac{K_p}{K_i} . \tag{5.17}$$

Variables are transformed into the s-domain through the Laplace transform,

$$L[f(t)] = F(s) . \tag{5.18}$$

PWM-VSI can be assumed as unity gain for the analysis in this section.

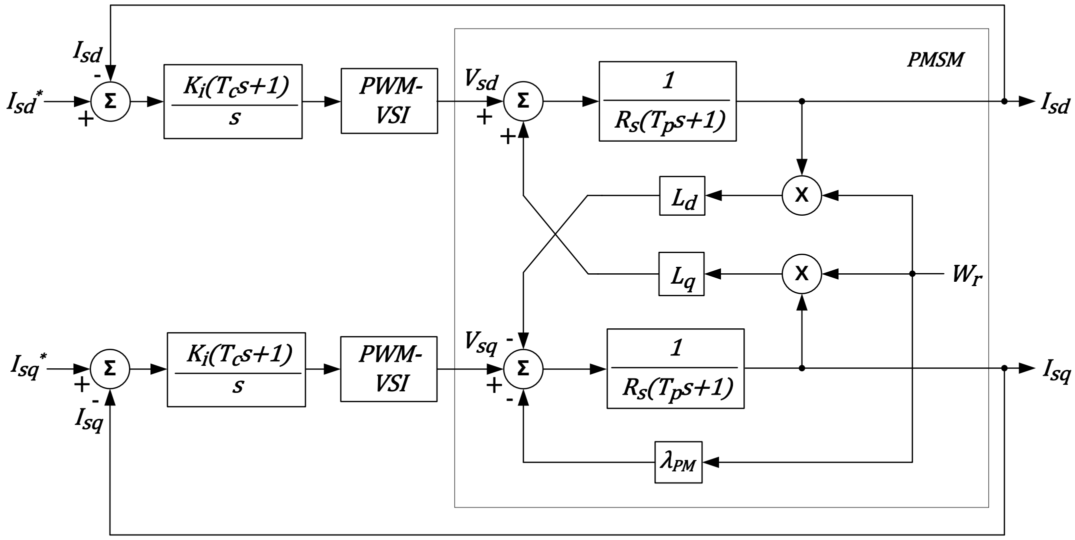

Figure 5.7. Synchronous frame P-I current regulated VSI fed PMSM drive.

The model of the PMSM in synchronous frame is a multiple-input multiple-output (MIMO) system. Also q- and d-axis state variables are cross coupled to each other. Therefore, to better analyze the system, an arrangement on the model can be done. d-axis current, I_{sd} can be written as,

$$I_{sd} = \frac{V_{sd} + W_r L I_{sq}}{R_s + Ls}. \tag{5.19}$$

Since the machine is non-salient, d- and q-axis inductances are shown as L where $L = L_d = L_q$. Inserting (5.19) into Laplace transformed form of (2.47), q-axis voltage-current relation becomes,

$$V_{sq} - \frac{L}{Ls + R_s} W_r V_{sd} - W_r \lambda_{PM} = \frac{(Ls + R_s)^2 + (W_r L)^2}{Ls + R_s} I_{sq}\,. \tag{5.20}$$

According to this relation block diagram can be represented as in Figure 5.8.

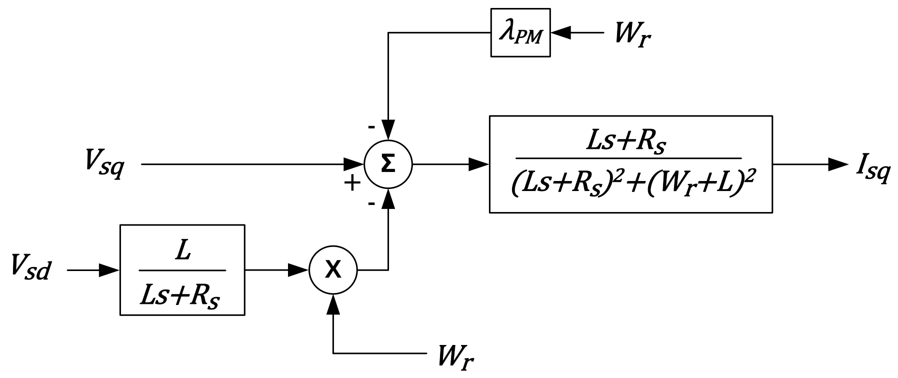

Figure 5.8. q-axis voltage-current relation block diagram.

According to this model, plant has two complex conjugate poles located at $\left(-\frac{R_s}{L} \pm jw_r\right)$. Conventional synchronous frame P-I current regulator add one pole at the origin and one zero at $\left(-\frac{K_i}{K_p}\right)$. In general, parameters of the P-I regulator are tuned to cancel the plant pole at zero speed such that, $\frac{K_i}{K_p} = \frac{R_s}{L}$. This is partially true for low speed operation, but when the speed gets higher, imaginary part of the plant pole gets higher and it moves away from the controller zero.

In order to understand effect of the cross-coupling between the d- and q-axes, and frequency dependency of this coupling, a simulation is performed. A three-phase RL load is represented in the synchronous frame. Then, synchronous frame P-I current regulators are implemented for current regulation. Resistance is set as 1 ohm and inductance as 2 mH. Parameters of the controller are tuned to cancel the plant pole such that K_p is “1” and K_i is “500”. Synchronous frequency is set as 50 Hz. Step functions are applied for d- and q-axes reference signals. Results are seen in Figure 5.9. It is seen that, when a change occurs in one of the axis, it causes a perturbation in the other axis. The same test is repeated for 200 Hz synchronous frequency and resultant currents are shown in Figure 5.10. As seen, when the synchronous frequency gets higher, effect of the cross-coupling increases and transient response of the controller degrades.

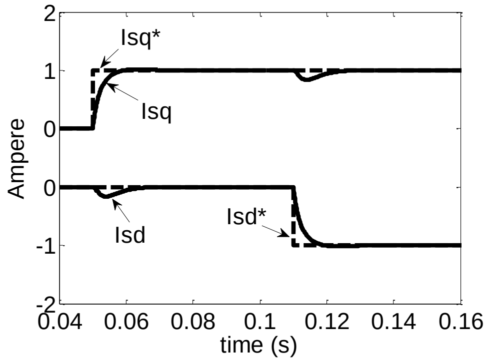

Figure 5.9. Cross-coupling effect when synchronous frequency is 50 Hz.

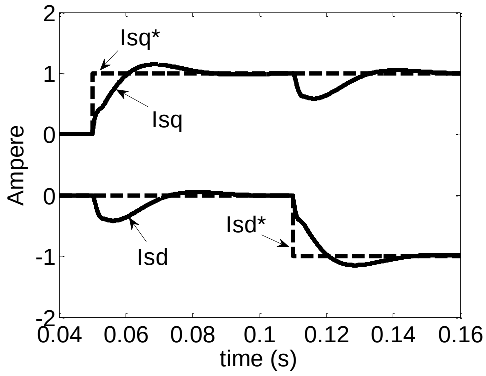

Figure 5.10. Cross-coupling effect when synchronous frequency is 200 Hz.

q-axis current I_{sq} can be written in terms of the current command (I_{sq}^{*}) and other state variables (I_{sd} and W_r) after some arrangement,

$$I_{sq} = \frac{K_i(T_c s + 1)}{K_i(T_c s + 1) + R_s s(T_p s + 1)} I_{sq}^{*} - \frac{\lambda_{PM} s}{K_i(T_c s + 1) + R_s s\left(T_p s + 1\right)} W_r$$

$$- \frac{L_d s}{K_i(T_c s + 1) + R_s s\left(T_p s + 1\right)} W_r I_{sd} \, . \quad (5.21)$$

The first term in (5.21) is related to the *command tracking* and other two are related to the *disturbance rejection* capability of the current regulator (I_{sd} *and* W_r may be interpreted as disturbance inputs on the q-axis).

To analyze the torque response of the drive system, q-axis current response should be examined (according to (2.53)). To examine the command tracking capability, reference input to output transfer function can be written as,

$$\left.\frac{I_{sq}}{I_{sq}^{*}}\right|_{W_r=0} = \frac{K_i(T_c s + 1)}{K_i(T_c s + 1) + R_s s(T_p s + 1)}\,. \tag{5.22}$$

Assuming the controller is tuned such that $T_c = T_p$ for pole-zero cancellation then,

$$\left.\frac{I_{sq}}{I_{sq}^{*}}\right|_{w_r=0} = \frac{K_i}{R_s s + K_i}\,. \tag{5.23}$$

Defining $T_p' = \frac{R_s}{K_p}$,

$$\left.\frac{I_{sq}}{I_{sq}^{*}}\right|_{W_r=0,\, I_{sd}=0} = \frac{1}{T_p' s + 1}\,. \tag{5.24}$$

Equation (5.24) shows a first order system behavior between the reference input and output. Therefore, we can say that, a synchronous frame P-I current controlled PMSM drive exhibits first-order system behaviour. It responds to step command with zero steady-state error and transient characteristic depends on the time constant, but it responds to ramp input with finite steady-state error. Similar results are valid for d-axis controller.

It is said that, d-axis current and rotor speed can be treated as disturbance inputs for q-axis. To analyze the disturbance rejection capability of the q-axis controller, disturbance to output transfer function can be written from,

$$\left.I_{sq}\right|_{I_{sq}^{*}=0} = -\frac{\lambda_{PM} s}{K_i(T_c s + 1) + R_s s\big(T_p s + 1\big)} W_r - \frac{L_d s}{K_i(T_c s + 1) + R_s s\big(T_p s + 1\big)} W_r I_{sd}\,. \tag{5.25}$$

The output should not respond to disturbance inputs. However, (5.25) shows a second-order system behaviour between the disturbance input and the output. For a step disturbance input, I_{sq} becomes zero at steady-state. However for a higher order input like ramp or parabola, steady-state error would not be zero.

For the d-axis current controller, similar transfer functions can be written for command tracking and disturbance rejection characteristics of the controller. Only difference is that, there is no voltage component on the d-axis due to permanent-magnet field so, only disturbance comes from the q-axis flux linkage.

In conclusion, PMSM drive with synchronous frame P-I controllers achieves desirable steady-state characteristics however, the transient response needs further enhancements.

5.3.2 Decoupling Method to Improve the Torque Control Performance

If the q-axis voltage to current relationship is examined, it is evident that, components related to the permanent-magnet flux linkage and d-axis flux linkage act as disturbance inputs on the q-axis. As for d-axis, component related to the q-axis flux linkage acts as a disturbance input on the d-axis.

Synchronous frame P-I current regulator, SFCR tries to reject these disturbances but it cannot reject them completely due to its limited bandwidth as remarked before.

To improve the disturbance rejection performance, another method should be used. If the disturbance inputs are known, a better disturbance rejection performance can be achieved by applying directly the necessary voltage to compensate the disturbances.

The implementation of the method on the q-axis is shown in Figure 5.11. $(-W_r L_d I_{sd})$ and $(-W_r \lambda_{PM})$ are the disturbance terms on the q-axis. $\left(W_r \hat{L}_d I_{sd}\right)$ and $\left(W_r \hat{\lambda}_{PM}\right)$ are the estimated values of the disturbances. $\hat{L}_d$ and $\hat{\lambda}_{PM}$ are the estimated values of the d-axis inductance and permanent-magnet flux linkage, respectively. PWM-VSI is represented as a gain, K_a. $\widehat{K}_a$ is the estimated transfer function of the PWM-VSI.

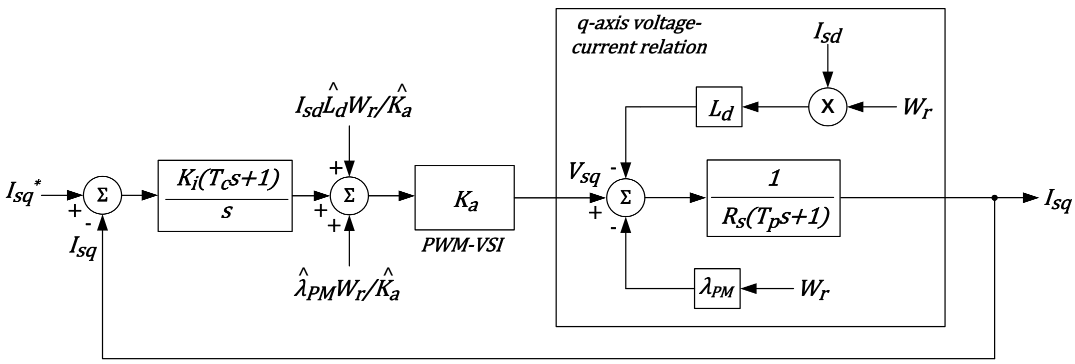

Figure 5.11. Implementation of the method that improves the disturbance rejection performance of the q-axis current controller.

When the method is implemented, the relationship between the output and the disturbance inputs becomes,

$$I_{sq}\big|_{I_{sq}^{*}=0} = -\frac{s}{K_i(T_c s+1)+R_s s(T_p s+1)} W_r\left(\lambda_{PM}-\hat{\lambda}_{PM}\frac{K_a}{\widehat{K}_a}\right)$$
$$-\frac{s}{K_i(T_c s+1)+R_s s(T_p s+1)} W_r I_{sd}\left(L_d-\hat{L}_d\frac{K_a}{\widehat{K}_a}\right). \tag{5.26}$$

If the estimated parameters ($\hat{L}_d$, $\hat{\lambda}_{PM}$) and transfer function of the PWM-VSI ($\widehat{K}_a$) match with the actual ones, output is not affected by the disturbances. When the actual parameters deviate from the estimated ones, performance of the method degrades, but, it still works unless the estimation errors ($\left|\lambda_{PM}-\hat{\lambda}_{PM}\frac{K_a}{\widehat{K}_a}\right|$ and $\left|L_d-\hat{L}_d\frac{K_a}{\widehat{K}_a}\right|$) become greater than the actual values (λ_{PM} and L_d).

The method can be applied on the d-axis in a similar manner. Disturbance term on the d-axis is $W_r L_q I_{sq}$. Complete block diagram of the method is shown in Figure 5.12.

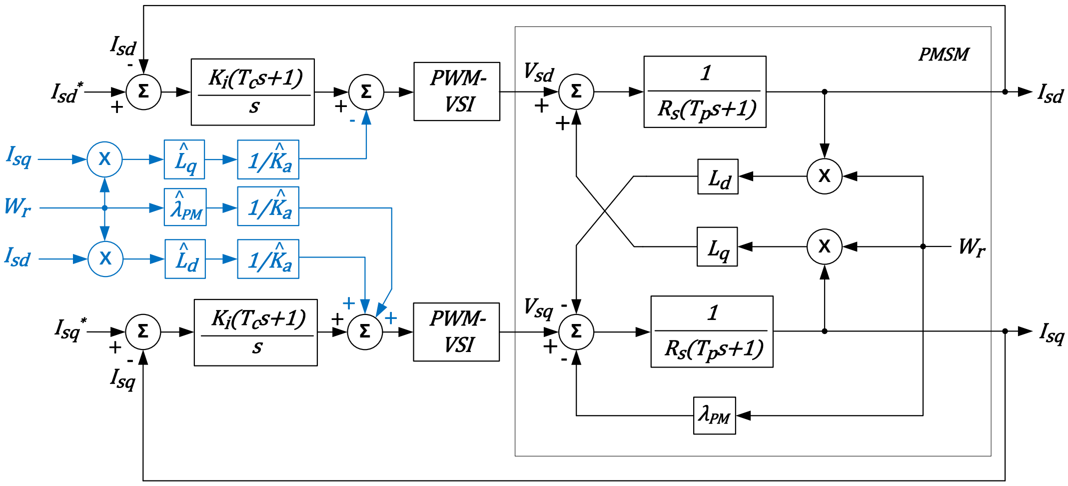

Figure 5.12 Implementation of the method that improves the disturbance rejection performance of synchronous frame current controller.

5.4 Speed Control Performance of PMSM Drive

In this section, performance of the conventional P-I speed controller is analyzed. Then, load torque estimation method is presented.

5.4.1 Analysis of Conventional P-I Speed Control

In general, PID controller or its variations are used to control the speed of a machine. Usually, the speed control loop is cascaded with a current control loop as demonstrated in Figure 5.13. Only q-axis voltage-current relation is depicted there since, q-axis current is the source of torque in a surface-mounted PMSM. T_{em} is the electromagnetic torque generated by the machine, T_l is the load torque and T_{net} is the net torque acting on the total moments of inertia of the mechanical system, J_{eq}. The total moments of inertia, J_{eq} is the sum of the rotor and load inertia as defined in (2.56).

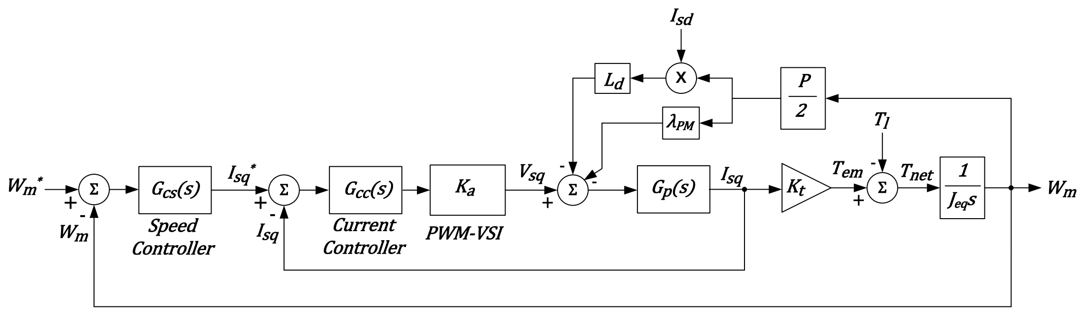

Figure 5.13. Cascaded speed and current control loops.

$G_{cc}(s)$ is the transfer function for the current controller,

$$G_{cc}(s) = \frac{K_p s + K_i}{s} \tag{5.27}$$

$G_p(s)$ is the transfer function between q-axis voltage and current,

$$G_p(s) = \frac{1}{Ls + R_s}. \tag{5.28}$$

K_t is the torque constant of the machine which is defined for the surface-mounted PMSM as,

$$K_t = \frac{3P}{4}\lambda_{PM}. \tag{5.29}$$

$G_{cs}(s)$ is the transfer function of the speed controller. Usually, P-I controllers are used for speed control purposes. Transfer function of the P-I speed controller is written as in (5.30) where K_{ps} is the proportional gain and K_{is} is the integral gain of the speed P-I controller.

$$G_{cs}(s) = \frac{K_{ps}s + K_{is}}{s}. \tag{5.30}$$

Assuming that, q-axis is decoupled from the d-axis and the rotor speed as explained in section 5.3.2 then, the speed control block diagram becomes as the one demonstrated in Figure 5.14. Transfer functions cascaded all in the current loop are replaced by a single transfer function $G_1(s)$ defined as;

$$G_1(s) = \frac{G_{cc}(s)K_aG_p(s)}{1 + G_{cc}(s)K_aG_p(s)} = \frac{K_aK_ps + K_i}{Ls^2 + (R_s + K_aK_p)s + K_aK_i}. \tag{5.31}$$

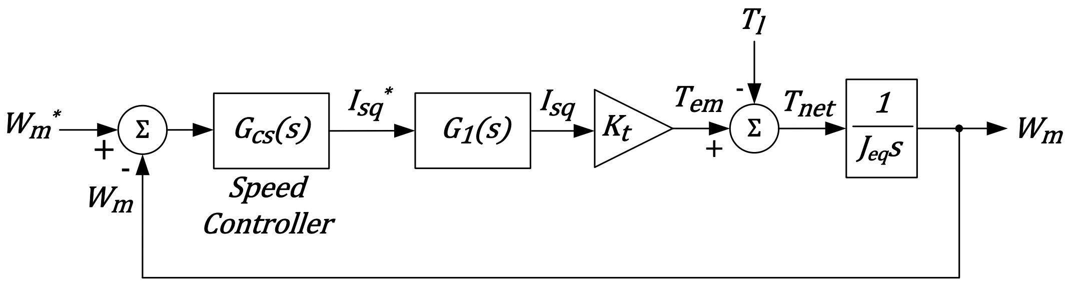

Figure 5.14. Block diagram of the speed control loop where the disturbance voltages on the q-axis are assumed to be decoupled.

Performance of the speed control loop can be evaluated from the transfer functions defined in (5.32) and (5.33). Transfer function in (5.32) is related with the command tracking capability of the speed control loop and transfer function in (5.33) is related with the disturbance rejection capability of the speed control loop.

$$\left.\frac{W_m}{W_m^*}\right|_{T_l=0} = \frac{G_{cs}(s)G_1(s)K_t}{J_{eq}s + G_{cs}(s)G_1(s)K_t} = \frac{G_1(s)K_t(K_{ps}s + K_{is})}{J_{eq}s^2 + G_1(s)K_t(K_{ps}s + K_{is})} \tag{5.32}$$

$$\left.\frac{W_m}{T_l}\right|_{W_m^*=0} = \frac{-1}{J_{eq}s + G_{cs}(s)G_1(s)K_t} = \frac{-s}{J_{eq}s^2 + G_1(s)K_t(K_{ps}s + K_{is})}. \tag{5.33}$$

Note that, T_l includes not only the load torque but also the other external torques such as, friction, windage, unbalance torque etc.

In general, current control loop, $G_1(s)$ is assumed to be ideal while analyzing the speed control loop since, the current control dynamics are very fast compared to the mechanical system dynamics. In accordance with this assumption, transfer functions in (5.32) and (5.33) become,

$$\left.\frac{W_m}{W_m^*}\right|_{T_l=0} = \frac{K_t K_{ps} s + K_t K_{is}}{J_{eq} s^2 + K_t K_{ps} s + K_t K_{is}} \tag{5.34}$$

$$\left.\frac{W_m}{T_l}\right|_{W_m^*=0} = \frac{-s}{J_{eq} s^2 + K_t K_{ps} s + K_t K_{is}}. \tag{5.35}$$

Second-order system relations are seen in the respective transfer functions. The performance of the speed control loop depends on the parameters of the P-I controller, K_{ps} and K_{is}. The performance of the controller increases with increasing controller gains, yet these parameters cannot be increased indefinitely since, this may degrade the stability of the system.

P-I controller actually works as an amplifier. It requires some error for the actuation and the actuation rate depends on the size of the error and gains of the amplifier. Ideally, gains can be tuned so large that a small error causes necessary actuation. However, due to practical reasons, gains cannot be set so large thus; a bigger error is needed for necessary actuation. Therefore, to increase the command tracking and disturbance rejection capability of the controller, different algorithms are needed.

5.4.2 Load Torque Estimation to Improve the Speed Control Performance

The disturbance rejection capability of the speed control loop can be increased if the information about the disturbance input is available. If so, the current needed to meet the load torque can be directly commanded. This provides the generation of the electromagnetic torque that compensates the disturbance torque thus, the speed of the machine is not interrupted.

However, it is not practical to measure the load torque. Instead, it can be estimated from the current and speed measurements and from the knowledge of the dynamics of the system. Such a configuration is depicted in Figure 5.15.

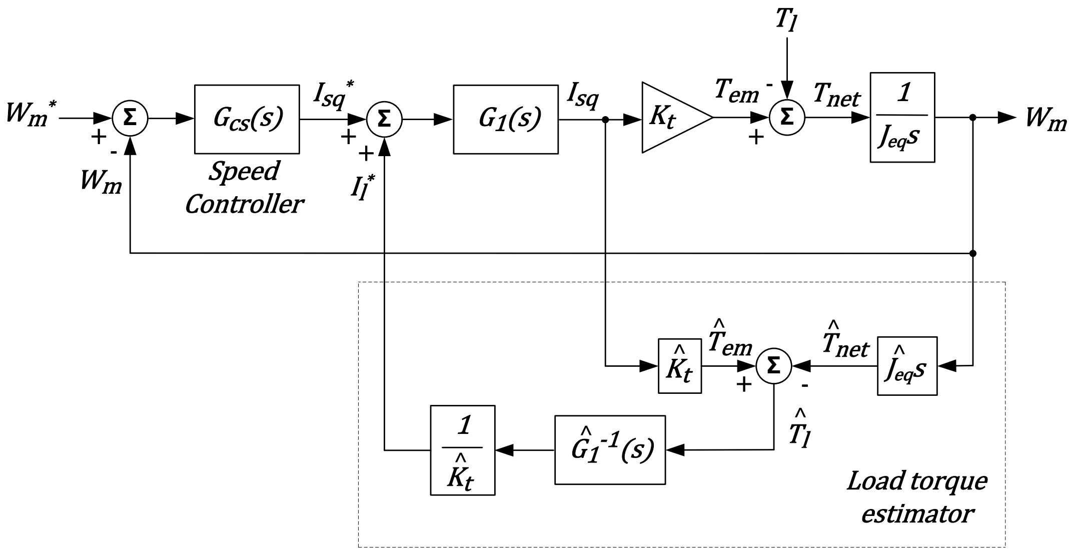

Figure 5.15. Load torque estimator used in speed control loop.

$\hat{J}_{eq}$ is the nominal value of the total inertia of the mechanical system and $\widehat{K}_t$ is the nominal value of the torque constant. $\widehat{G}_1(s)$ is the estimated transfer function of the current control loop. The load torque is estimated by means of the knowledge of the applied electromagnetic torque, $\widehat{T}_{em}$ and calculated net torque, $\widehat{T}_{net}$ acting on the inertia. Electromagnetic torque, $\widehat{T}_{em}$ can be obtained by multiplying the q-axis current with torque constant, $\widehat{K}_t$. Net torque acting on the inertia can be calculated by multiplying the angular acceleration with the inertia. The difference between the applied torque and the net torque corresponds to load torque which can be directly met by applying the necessary current to the machine.

Estimated load torque can be written as,

$$\widehat{T}_l = \widehat{K}_t I_{sq} - \hat{J}_{eq} W_m s\,. \tag{5.36}$$

To meet the estimated load torque, current command that will be added to reference current is calculated as,

$$I_l^* = \frac{\widehat{G}_1{}^{-1}(s)}{\widehat{K}_t}\left[\widehat{K}_t I_{sq} - \hat{J}_{eq} W_m s\right]. \tag{5.37}$$

The term $W_m s$ corresponds to angular acceleration which is written as,

$$W_m s = \frac{T_{em} - T_l}{J_{eq}} = \frac{K_t I_{sq} - T_l}{J_{eq}}. \tag{5.38}$$

Substituting (5.38) into (5.37),

$$I_l{}^* = \frac{\hat{G}_1{}^{-1}(s)}{\hat{K}_t}\left[\hat{K}_t I_{sq} - \frac{\hat{J}_{eq}}{J_{eq}}\left(K_t I_{sq} - T_l\right)\right]. \tag{5.39}$$

The net torque exerted on the inertia is the electromagnetic torque subtracted by the load torque,

$$T_{net} = T_{em} - T_l = K_t\left(I_{sq}^* + I_l{}^*\right)G_1(s) - T_l\,. \tag{5.40}$$

Substituting (5.39) into (5.40),

$$\begin{aligned} T_{net} &= K_t I_{sq}^* G_1(s) + G_1(s)\hat{G}_1{}^{-1}(s)\frac{K_t}{\hat{K}_t}\left[I_{sq}\hat{K}_t - \frac{\hat{J}_{eq}}{J_{eq}}\left(I_{sq}K_t - T_l\right)\right] - T_l \\ &= K_t I_{sq}^* G_1(s) + G_1(s)\hat{G}_1{}^{-1}(s) I_{sq} K_t\left(1 - \frac{K_t \hat{J}_{eq}}{\hat{K}_t J_{eq}}\right) \\ &\quad + \left(G_1(s)\hat{G}_1{}^{-1}(s)\frac{K_t \hat{J}_{eq}}{\hat{K}_t J_{eq}} - 1\right)T_l \end{aligned} \tag{5.41}$$

where the first term, $I_{sq}^* G_1(s) K_t$ can be defined as the reference torque, T_{ref},

$$T_{ref} = K_t I_{sq}^* G_1(s)\,. \tag{5.42}$$

If the estimated parameters $\left(\hat{J}_{eq}, \hat{K}_t \text{ and } \hat{G}_1{}^{-1}(s)\right)$ match with the actual ones then, the effect of the load torque is removed and only commanded torque is exerted on the inertia,

$$T_{net} = T_{ref}\,. \tag{5.43}$$

An interesting property of the load torque estimator is reported in [39]. Load torque estimator can handle parameter variations as well as counterbalancing the load torque. When the torque equation given in (5.41) is examined it can be seen that, second term accounts for the parameter variations.

To understand how load torque estimator handles parameter variations, now assume that the load torque is zero. The closed loop transfer function of the driver-motor pair, $G_1(s)$ can be assumed as unity since, the time constant of the electrical system is much smaller than the mechanical system. With these assumptions (5.41) becomes,

$$T_{net} = K_t I_{sq} + K_t I_{sq}\left(1 - \frac{K_t \hat{J}_{eq}}{\hat{K}_t J_{eq}}\right). \tag{5.44}$$

Note that, the closed loop transfer function of the driver-motor pair, $G_1(s)$ is assumed as unity therefore, $I_{sq}^* = I_{sq}$.

When the parameters are equal to nominal values then, the net torque is equal to commanded torque. However, if the parameters deviate from the nominal values, net torque is increased or decreased according to deviation. For example, if torque constant K_t is equal to nominal value ($K_t = \hat{K}_t$) but, the inertia is increased by an amount of ΔJ_{eq} then net torque is increased such that,

$$T_{net} = I_{sq} K_t + I_{sq} K_t\left(\frac{\Delta J_{eq}}{\hat{J}_{eq} + \Delta J_{eq}}\right). \tag{5.45}$$

Similarly, let's assume inertia is equal to nominal value but, the torque constant is increased by ΔK_t then, the net torque is decreased such that,

$$T_{net} = I_{sq} K_t + I_{sq} K_t\left(\frac{-\Delta K_t}{\hat{K}_t}\right). \tag{5.46}$$

In conclusion, load torque estimation not only counterbalances the load torque but also handles the inertia and torque constant variations.

In order to estimate the load torque some parameters and measurements are necessary. Needed parameters are torque constant and inertia. Needed measurements are the q-axis current and angular acceleration ($W_m s$). It has been shown that, nominal values of the torque constant and inertia are sufficient for load torque estimator and the nominal values can be obtained by an offline experiments. q-axis current is already available for closed-loop current control purpose. The phase currents are measured with a current transducer and q-axis current is obtained from the phase currents by means of reference frame transformations. However, angular acceleration information is not easy to attain. Transducers for angular acceleration measurement are not economical [41]. It can be derived from angle or velocity measurements but it requires differentiation which amplifies the sensor noise. In this study, an observer is used for this purpose. Acceleration information is obtained from noisy velocity measurements by means of a Kalman filter.

5.4.2.1 Discrete-Time Kalman Filter

The Kalman filter tries to estimate the state $x[k]$ of a discrete-time linear stochastic difference equation given as,

$$x[k] = Ax[k-1] + Bu[k-1] + w[k-1]$$
$$y[k] = Cx[k] + v[k] \tag{5.47}$$

where A is the state transition matrix, B is the input matrix, $x[.]$ is the state vector, $u[.]$ is the input vector. C is the output matrix, $y[.]$ is output vector. Note that, state transition, input and output matrices are assumed to be time invariant. $w[k]$ is defined as the *process noise* which is zero-mean with normal probability distribution,

$$w[k] \sim (0, Q)\,. \tag{5.48}$$

$v[k]$ is defined as the *measurement noise* which is also zero-mean with normal probability distribution,

$$v[k] \sim (0, R)\,. \tag{5.49}$$

It is assumed that, the process noise and measurement noise are independent of each other.

Filter uses the system dynamics and noisy measurements to estimate the state. *A priori* state estimate (denoted as $\hat{x}_k^-$) is defined as the estimate of the state at time step k without the measurement at that time step. *A posteriori* state estimate (denoted as $\hat{x}_k^+$) is defined as the estimate of the state at time step k with the measurement at that time step.

A priori state estimation error is defined as,

$$e_k^- = x_k - \hat{x}_k^-\,. \tag{5.50}$$

Similarly, *A posteriori* state estimation error is written as,

$$e_k^+ = x_k - \hat{x}_k^+\,. \tag{5.51}$$

Covariance of the estimation errors is denoted as P_k,

$$P_k^- = E\left[e_k^- e_k^{-T}\right] \tag{5.52}$$

$$P_k^+ = E\left[e_k^+ {e_k^+}^T\right]. \tag{5.53}$$

A priori state estimate can be propagated from a *posteriori* state estimate in time according to system difference equation,

$$\hat{x}_k^- = A\hat{x}_{k-1}^+ + Bu_{k-1}\,. \tag{5.54}$$

Substituting (5.54) into (5.52) and taking expectation results in,

$$P_k^- = AP_{k-1}^+ A^T + Q \tag{5.55}$$

Equations (5.54) and (5.55) are known as *time update (prediction)* equations of the Kalman filter.

After the actual measurement is obtained, *a posteriori* state estimate can be calculated by adding a weighted difference between the actual measurement $y_k$and predicted measurement $C\hat{x}_k^-$ to the *a priori* state estimate,

$$\hat{x}_k^+ = \hat{x}_k^- + K(y_k - C\hat{x}_k^-) \tag{5.56}$$

where K is the *gain* matrix. The difference between the actual measurement and predicted measurement $(y_k - C\hat{x}_k^-)$ is called as *measurement innovation*. The gain matrix K is chosen such that minimizing the *a priori* state estimate error covariance which result in,

$$K = P_k^- C^T (CP_k^- C^T + R)^{-1}. \tag{5.57}$$

Last equation in discrete-time Kalman filter is the *a posteriori* state estimate covariance which is obtained by substituting the *a posteriori* state estimate into (5.53) using (5.54) and (5.57) which results in,

$$P_k^+ = P_k^- - KCP_k^-. \tag{5.58}$$

Equations (5.56), (5.57) and (5.58) are the *measurement update (correction)* equations of the Kalman filter.

Detailed information and derivations about Kalman filter can be found in [40].

5.4.2.2 Estimation of Angular Acceleration with Kalman Filter

The discrete time version of the Newtonian system with constant acceleration is formulated as in (5.59) [40],

$$\begin{bmatrix}\theta_m[k]\\ w_m[k]\\ \alpha_m[k]\end{bmatrix} = \begin{bmatrix}1 & T_s & T_s^2\\ 0 & 1 & T_s\\ 0 & 0 & 1\end{bmatrix}\begin{bmatrix}\theta_m[k-1]\\ w_m[k-1]\\ \alpha_m[k-1]\end{bmatrix} \tag{5.59}$$

where T_s is the sample period. System does not have a driving input that means, B is the zero matrix. State transition matrix is,

$$A = \begin{bmatrix}1 & T_s & T_s^2\\ 0 & 1 & T_s\\ 0 & 0 & 1\end{bmatrix}. \tag{5.60}$$

Acceleration information is obtained from velocity measurement so that output matrix C is defined as,

$$C = \begin{bmatrix}0 & 1 & 0\end{bmatrix}. \tag{5.61}$$

Kalman filter equations require process noise and measurement noise covariance matrices. Measurement noise covariance matrix can be acquired by offline experimental tests. Non-zero-mean noise components can be cancelled out by compensating the offset at the start of every operation.

However, it is difficult to obtain the process noise covariance since, the process noise is a hypothetical noise added to model. In general, it is tuned according to frequency response of the filter. If the process noise covariance grows, filter relies on the measurement heavily. This results a better frequency response in terms of attenuation and phase delay however, this also causes noise amplification. If the process noise covariance is decreased, the sensor noise is suppressed vigorously but, the frequency response of the filter is degraded. Therefore, an optimum point should be set for process noise covariance value.

Initial values of the *a posteriori* state estimate and state estimate error covariance are also required for the filter. Initial *a posteriori* state estimate can be set to zero but state estimate error covariance should not be set to zero since it results that the filter always believe $\hat{x}_k^+ = 0$. An arbitrary non-zero value should be used for the initial *a posteriori* estimate error covariance. It affects only initial estimates of the filter but, it eventually converges to the correct state.

Following the estimation of the angular acceleration with Kalman filter, net torque acting on the inertia can be found by multiplying the angular acceleration with the inertia. Applied electromagnetic torque is obtained from current measurement and torque constant. Estimated load torque is the difference between the applied electromagnetic torque and calculated net torque. The current needed to compensate the load torque is directly added to the current command. Block diagram of the estimation and compensation algorithm is demonstrated in Figure 5.16.

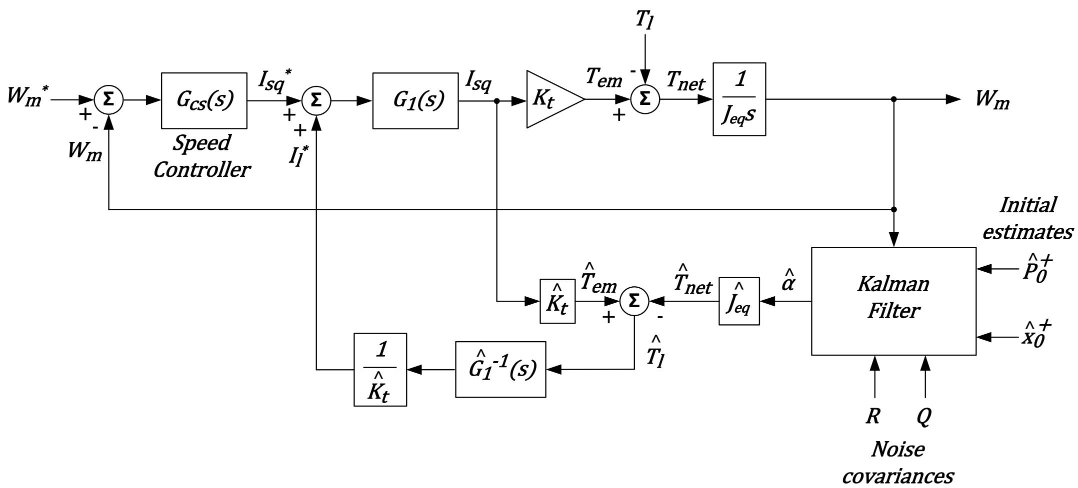

Figure 5.16. Load torque estimation with Kalman filter.

CHAPTER 6

SIMULATION AND EXPERIMENTAL RESULTS

6.1 Introduction

Simulation and experimental results are given in this chapter. First, simulation model in Simulink is described. Tuning of the controller parameters is explained. Then, the proposed methods to improve torque and speed control performance are verified on this model. Second, the experimental setup is demonstrated. Proposed algorithms are also validated with experimental tests.

6.2 Simulation Model

Simulation studies are conducted in Matlab/Simulink software. Mathematical model of the PMSM derived in CHAPTER 2, is implemented in the simulation as shown in Figure D.1 in APPENDIX D, with the parameters of the machine used in experiments, as listed in Table 6.3.

Nonlinear inverter nature is investigated in SimPowerSystems software. SimPowerSystems software operates in the Simulink environment and works together with Simulink to model electrical systems. Power MOSFET modules in the SimPowerSystems library are employed in order to construct the 3-phase VSI with the parameters given in Table 6.1.

To interface the VSI with the mathematical model of the machine, controlled voltage/current sources and voltage/current measurement blocks in the SimPowerSystems library are utilized.

Table 6.1. Parameters of the VSI used in the simulation.

On-state resistance of the MOSFET	5 Ohm	Threshold voltage of the diode	0.65 V
On-state resistance of the diode	0.12 mH	dc Bus voltage	24 V

Vector control algorithm is also implemented in the Simulink as shown in Figure D.2 in APPENDIX D. Stationary frame currents are sampled and transformed into synchronous frame. Sampling frequency is set to 10 KHz as in the experimental work. Discrete time P-I controllers are employed for d- and q-axes current regulation. Anti-windup and saturation algorithms are utilized as described in section 4.3. Space vector PWM scheme is applied as explained in section 3.3. Lastly, a triangular carrier signal is generated and it is compared with the outputs of the space vector PWM block. MOSFET gate signals are generated according to this comparison.

The complete block diagram of the simulation model is shown in Figure D.3 in APPENDIX D. Output of the vector controller is connected to gates of the MOSFETs in the VSI which feeds the PMSM. Currents flowing through the phases of PMSM are measured and they are sampled by the vector controller.

Volt-second compensation method, decoupling algorithm and load torque estimation are implemented and tested according to this simulation model. For speed control studies, inverter is modelled as a unity gain in order to accelerate the simulation. Throughout the simulation studies, simulation step size is adjusted to 1 microsecond.

6.3 Tuning of Current Controller Parameters

The block diagram of the vector controlled PMSM drive is shown in Figure 5.7 in which two separate P-I controllers are employed for d- and q-axis current regulation. Same controller parameters can be used since; both axes have the same inductance and resistance values.

Current controller parameters should be adjusted according to the poles of the plant. In general, the zero of the P-I current controller is chosen such that, it cancels the plant pole,

$$\frac{K_i}{K_p} = \frac{R_s}{L}. \tag{6.1}$$

This relation tells the ratio of the proportional constant (K_p) and integral constant (K_i). In order to determine the parameters, another relation is needed.

When the plant pole is cancelled by the controller zero, the open-loop transfer function of the current control loop (for one of the axis) becomes,

$$G_{OL}(s) = \frac{K_i}{R_s s}. \tag{6.2}$$

A second requirement on the parameters can be written by setting the closed-loop bandwidth of the system to a desired frequency. Usually, closed-loop bandwidth is approximately equal to the gain-crossover frequency of the open-loop transfer function. Gain-crossover frequency is the frequency where the magnitude of the open-loop transfer function is equal to unity. Replacing "s" by "jw" in the open-loop transfer function,

$$|G_{OL}(jw)| = \left|\frac{K_i}{R_s j w_c}\right| = 1\ . \tag{6.3}$$

Then, the parameters of the current controllers can be determined according to (6.1) and (6.3).

In this thesis, current controller is tuned for 300 Hz bandwidth so, integral constant, K_i is found from (6.3) as 128. According to (6.1), proportional constant, K_p is determined as 0.24.

The open loop transfer function has a single pole at the origin therefore; its phase angle is constant at -90^0 as seen in Figure 6.1. The gain margin is infinite and phase margin is 90^0.

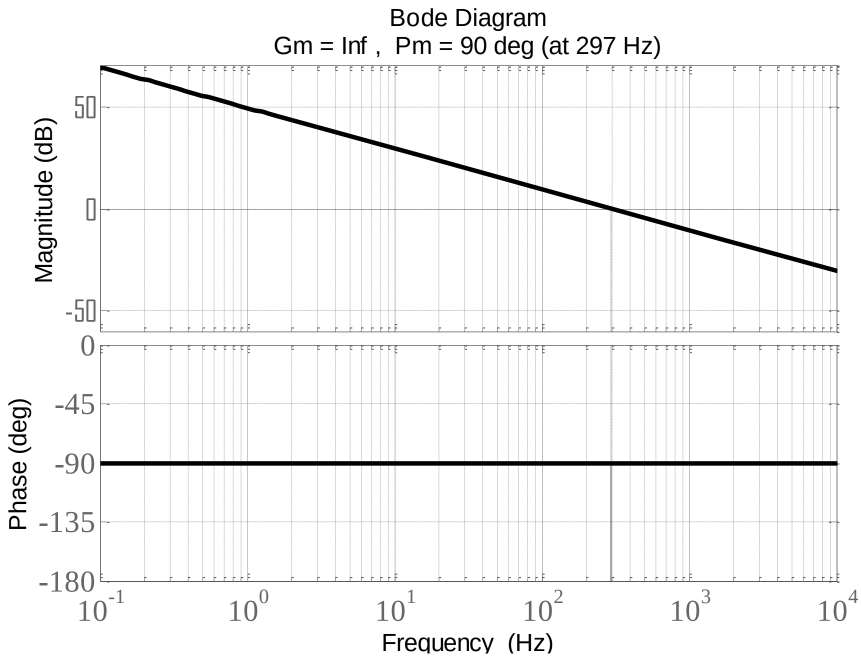

Figure 6.1. Open-loop Bode diagram of the current control loop.

6.4 Simulation Results of the Volt-Second Compensation

In order to test the volt-second compensation algorithm, synchronous frame P-I current regulator is implemented as shown in Figure D.3 in APPENDIX D and current waveforms are examined. Then, compensation algorithm is added to the system as demonstrated in Figure 5.6 and performance improvement is analyzed.

PWM carrier period is set to 100 microseconds by setting the frequency of the triangular carrier signal to 10 KHz. In order to simulate the nonlinearity of the VSI, 2.2 microsecond delay is inserted before the rising edge of the gate signals (2 microseconds for dead-time and 0.2 microseconds for turn-on time). Similarly, 0.7 microsecond delay is inserted before the falling edge of the gate signals to simulate the turn-off time of the switches as seen in Figure D.4 in APPENDIX D. Parameters of the power MOSFET model are adjusted according to Table 6.1.

Parameters of the synchronous frame P-I current controller (SFCR) are listed in Table 6.2.

Tests are done when machine operates at a speed of 300 rpm. 10 Ampere quadrature-axis synchronous frame current (i_{sq}) is commanded. Direct-axis current (i_{sd}) is commanded as zero. Phase current waveform under these conditions is presented in Figure 6.2.

If the machine was supplied by an ideal source, phase current waveform would be purely sinusoidal. However, due to the nonidealities in the VSI, phase current waveform is distorted as seen in Figure 6.2.

Table 6.2. Parameters of the SFCR in the simulation.

Proportional constant, K_p	0.24
Integral constant, K_i	128

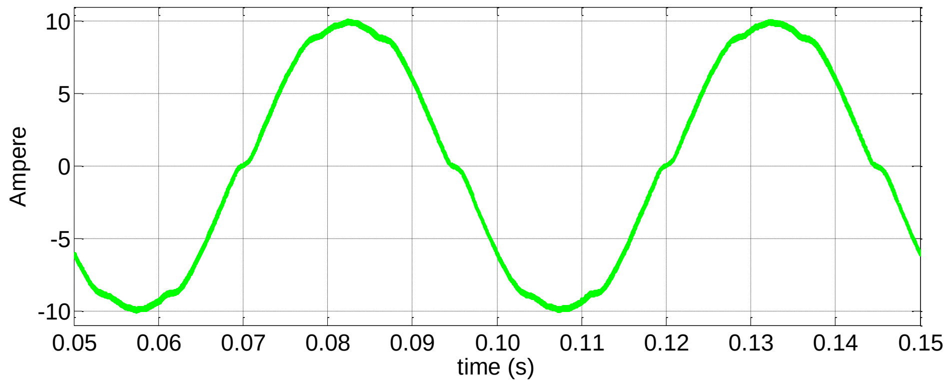

Figure 6.2. Phase current waveform with synchronous frame P-I current regulator when machine operates at 300 rpm in the simulation.

q- and d-axes currents are shown in Figure 6.3. Synchronous frame currents would be constant if the VSI was ideal. However, an oscillation exists on the current waveforms due to the nonideal characteristics of the VSI. Frequency of the oscillations is sixth times the synchronous frequency as explained in section 5.2.1.

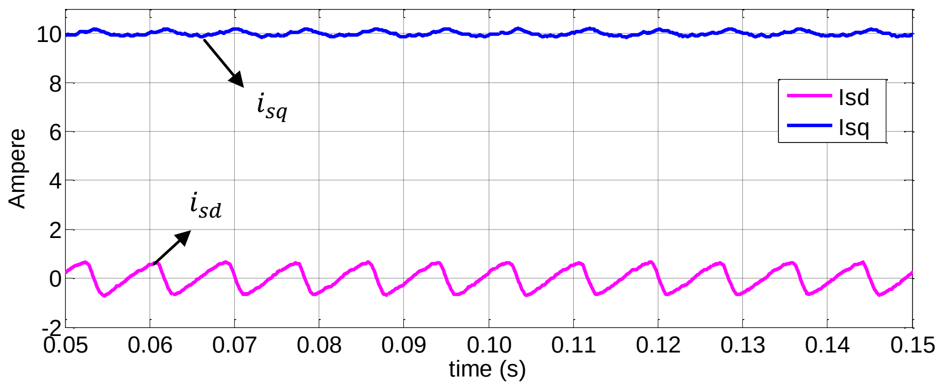

Figure 6.3. Synchronous frame currents with synchronous frame P-I current regulator when machine operates at 300 rpm in the simulation.

In the second part of the test, volt-second compensation algorithm is implemented as explained in section 5.2.2. Polarities of the phase currents are determined from current space vector angle according to Table 5.2.

Space vector angle is the summation of the torque angle δ and rotor angle θ_r as depicted in Figure 2.10. Torque angle is set to ninety degree (zero direct-axis current). The implementation of the algorithm is seen in Figure D.5 in APPENDIX D.

Under the same conditions with the first test (machine operates at 300 rpm, q- and d-axes currents are commanded as 10 and 0 Ampere respectively) phase current is observed again and effect of the volt-second compensation algorithm is examined. Phase current waveform is shown in Figure 6.4. As compared to Figure 6.2, it is clear that, the quality of phase current waveform is improved significantly. The distortion on the current waveform due to nonideal characteristics of the VSI is nearly vanished. It has become very close to a pure sinusoid which is expected for an ideal VSI.

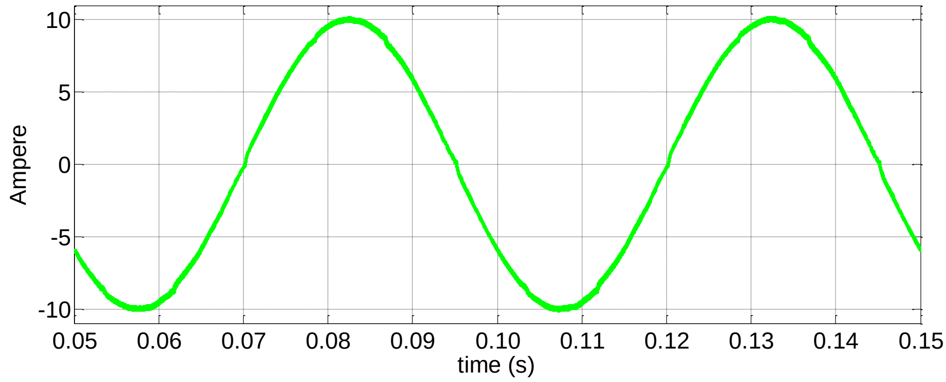

Figure 6.4. Phase current waveform with volt-second compensation algorithm when machine operates at 300 rpm in the simulation.

Synchronous frame currents are shown in Figure 6.5. A considerable decrease in the magnitude of the ripples on the synchronous frame currents is seen as compared to Figure 6.3. There is still some distortion on the synchronous frame currents especially on the d-axis. The reason of this distortion is the *zero-current clamping* phenomenon which cannot be solved with volt-second compensation.

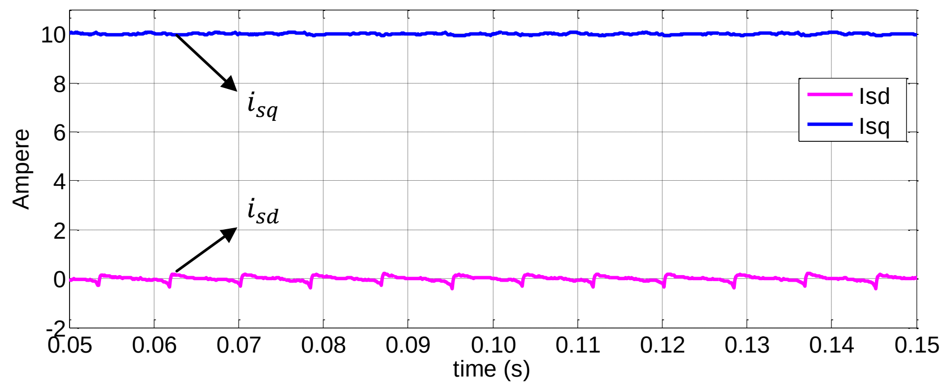

Figure 6.5. Synchronous frame currents with compensation algorithm when machine operates at 300 rpm in the simulation.

6.5 Simulation Results of the Decoupling Method

In this section, effects of the disturbance inputs on the current loop are examined. Besides that, decoupling method to improve the disturbance rejection capability of the current controller is also examined.

In order to adjust the shaft speed, a continuous-time P-I speed controller is designed in the simulation as demonstrated in Figure D.3 in APPENDIX D. This controller tries to regulate the shaft speed by controlling the load torque.

Parameters for the synchronous frame current regulator are not changed and used as in the preceding section.

In the tests, the quadrature-axis synchronous frame current (i_{sq}) is set to 10 Ampere. The d-axis current (i_{sd}) is commanded as zero. Since the motor speed acts like disturbance both on the d- and q-axes, effects of the speed variation on the axes are investigated in these tests. During the tests, the shaft speed is controlled by the load drive.

In the first test, the load drive changes the shaft speed sinusoidally. The frequency of the sinusoidal is 2 Hz and magnitude of it is 600 rpm, as shown in Figure 6.7. Synchronous frame currents under these conditions are demonstrated in Figure 6.6. In this figure, i_{sd}^* and i_{sq}^* are the commanded d- and q-axes currents. i_{sd} and i_{sq} are the actual d- and q-axes currents.

Although a constant current is commanded, it is observed that, there exists an oscillation on the q-axis current. The frequency of this oscillation is the same with the frequency of the shaft speed. The reason of this oscillation is the speed depended coupling terms present in the system as can be seen in Figure 5.7.

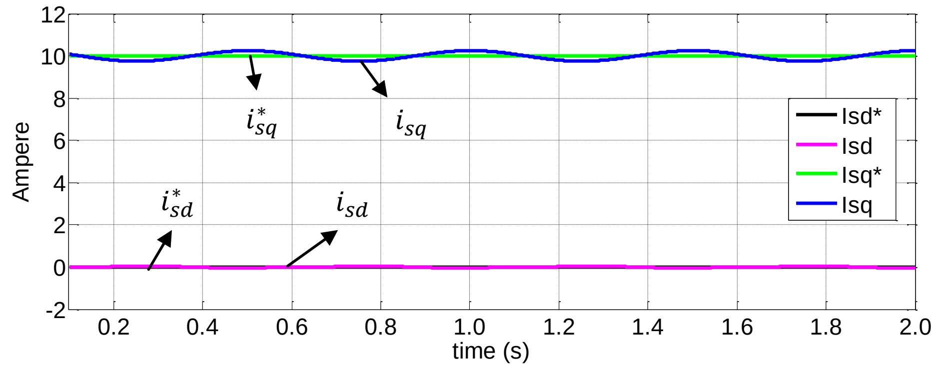

Figure 6.6. d- and q-axes currents when the shaft speed changes sinusoidally (magnitude: 600 rpm, frequency: 2 Hz) in the simulation.

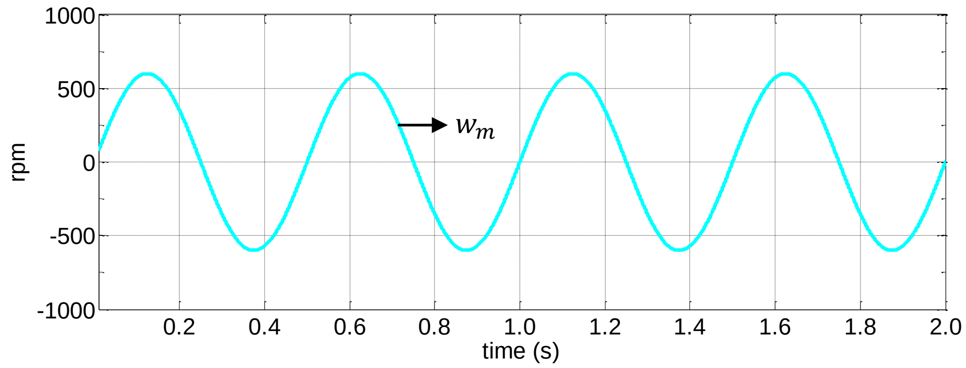

Figure 6.7. Sinusoidally varying shaft speed (magnitude: 600 rpm, frequency: 2 Hz) in the simulation.

In the second test, the load drive changes the shaft speed sinusoidally again. The frequency of the sinusoidal is 5 Hz and magnitude of it is 600 rpm, as shown in Figure 6.9. Synchronous frame currents under these conditions are demonstrated in Figure 6.8.

An oscillation on the synchronous frame currents with the same frequency of the shaft speed is observed again. However, the magnitude of the oscillation is increased. This result is expected since; the performance of the current controller degrades when the frequency of the disturbance input increases.

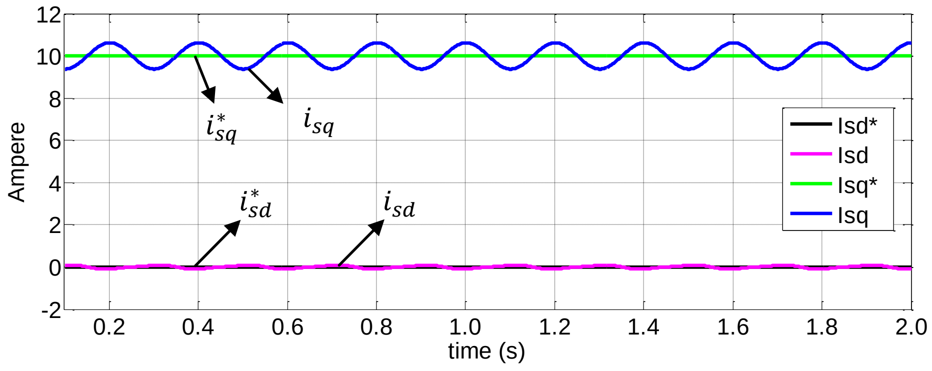

Figure 6.8. d- and q-axes currents when the shaft speed changes sinusoidally (magnitude: 600 rpm, frequency: 5 Hz) in the simulation.

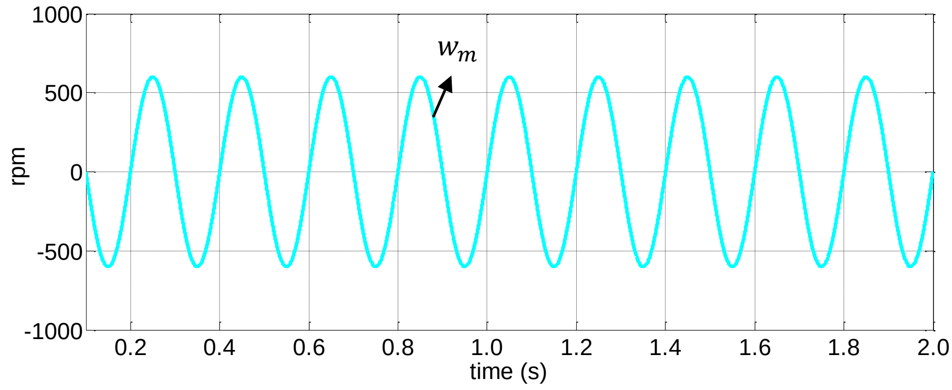

Figure 6.9. Sinusoidally varying shaft speed (magnitude: 600 rpm, frequency: 5 Hz) in the simulation.

In the third test, a 600 rpm step change occurs on the shaft speed as demonstrated in Figure 6.11. In the meantime, synchronous frame currents are shown in Figure 6.10. As can be seen, a perturbation occurs in the d- and q-axes currents when a change occurs in the shaft speed.

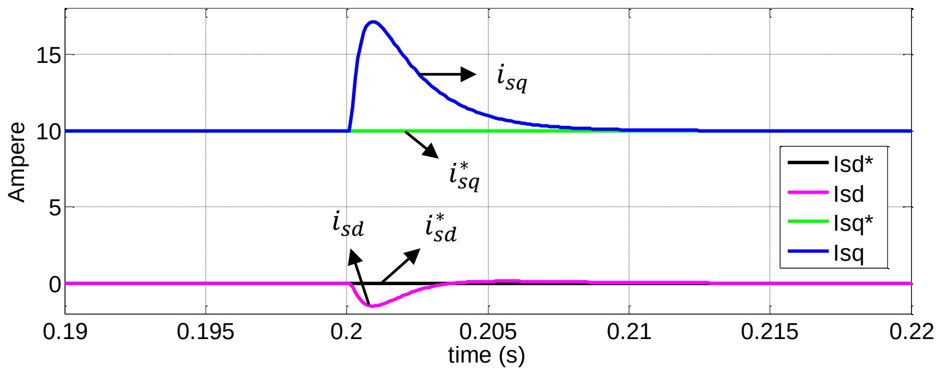

Figure 6.10. d- and q-axes currents when a 600 rpm step change occurs on the shaft speed in the simulation.

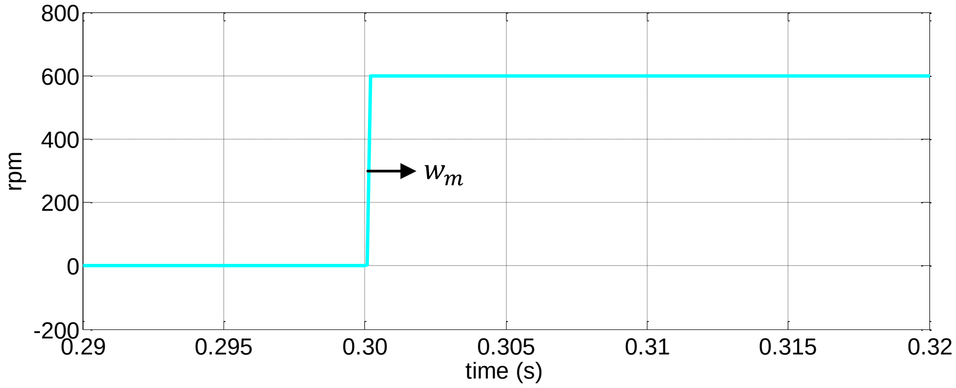

Figure 6.11. 600 rpm step change on the shaft speed in the simulation.

To improve the response of the current controller, decoupling method is implemented in the simulation as demonstrated in Figure D.6 in APPENDIX D. Same tests so far in this section are repeated with the decoupling method. The results can be seen in Figure 6.12, Figure 6.13 and Figure 6.14.

Oscillations on the synchronous frame currents nearly vanished when the decoupling method is implemented as shown in Figure 6.12 and Figure 6.13 as compared to Figure 6.6 and Figure 6.8 respectively.

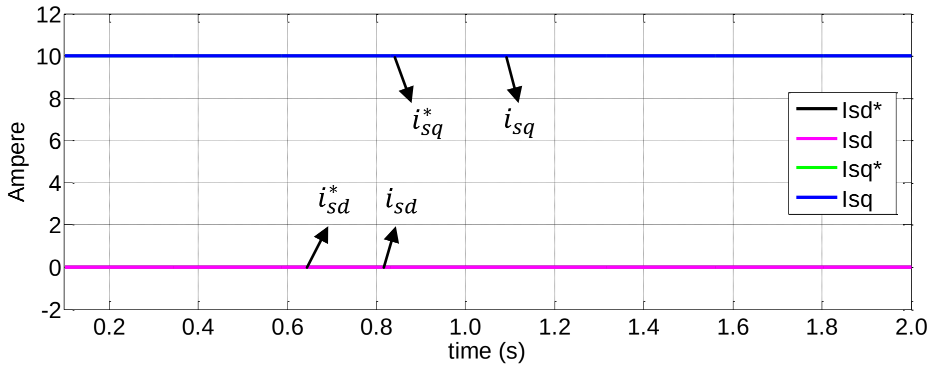

Figure 6.12. d- and q-axes currents with the decoupling method when the shaft speed changes sinusoidally (magnitude: 600 rpm, frequency: 2 Hz) in the simulation.

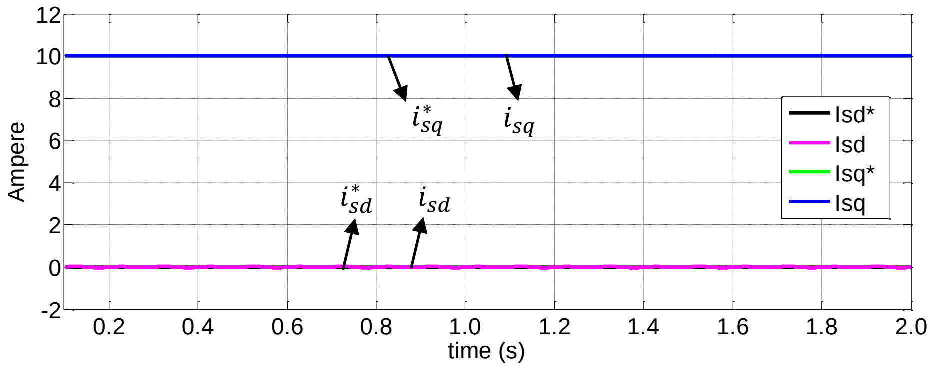

Figure 6.13. d- and q-axes currents with the decoupling method when the shaft speed changes sinusoidally (magnitude: 600 rpm, frequency: 5 Hz) in the simulation.

Synchronous frame currents with the decoupling method when a step change occurs on the shaft speed are seen in Figure 6.14. As compared to the case where the decoupling method is not implemented (Figure 6.10), a considerable improvement is achieved on the transient response after the implementation of the decoupling method.

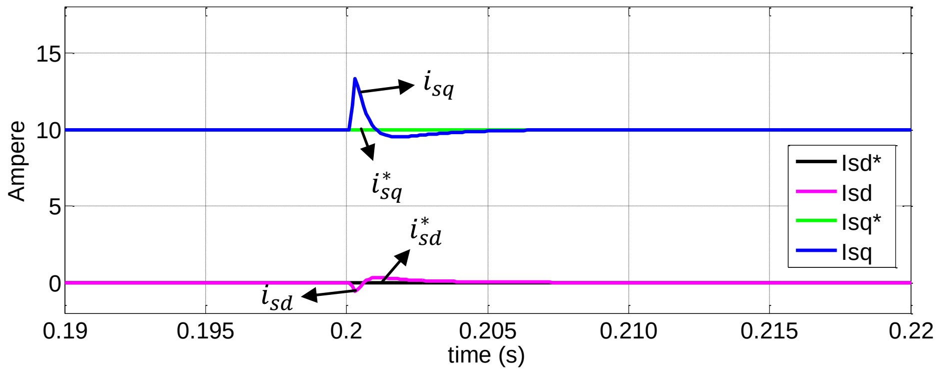

Figure 6.14. d- and q-axes currents with the decoupling method when a 600 rpm step change occurs on the shaft speed in the simulation.

6.6 Tuning of the Speed Controller Parameters

The bandwidth of the speed control loop should be selected to be one tenth of that for the current loop. Therefore, current control loop can be assumed as unity for speed controller design. The bandwidth of the current control loop was adjusted to 300 Hz, so the bandwidth of the speed control loop is set to 30 Hz. When the current loop is assumed to be unity, the open-loop transfer function can be written as (6.4).

$$G_{OL}(s) = \frac{K_t\left(K_{ps}s + K_{is}\right)}{Js^2} \tag{6.4}$$

where K_{ps} and K_{is} are the proportional and integral constants of speed loop P-I controller. These parameters can be selected according to some design criterions such as the closed-loop bandwidth and phase margin.

The closed-loop bandwidth is desired to be one tenth of that for the current loop, 30 Hz as noted before. The gain-crossover frequency of the open-loop transfer function is approximately equal to the closed-loop bandwidth. Gain-crossover frequency is the frequency where the magnitude of the open-loop transfer function is equal to unity,

$$|G_{OL}(jw)| = \left|\frac{K_t\left(K_{ps}jw_c + K_{is}\right)}{J(jw_c)^2}\right| = 1\,. \tag{6.5}$$

Another design criterion is the phase margin (PM) which should be adjusted greater than 45^0, typically to 60^0. The phase margin is the difference between the phase curve and -180^0 at the point corresponding to the gain-crossover frequency,

$$\mathrm{PM} = \arg\left(G_{OL}(jw_c)\right) - (-180^0) = arg\left(\frac{K_t\left(K_{ps}jw_c + K_{is}\right)}{J(jw_c)^2}\right) + 180^0 \tag{6.6}$$

where $\arg(.)$ is the argument function which gives the phase of the transfer function.

The proportional and integral constants are found as 0.27 and 30 respectively, for 30 Hz bandwidth and 60^0 phase margin, using (6.5) and (6.6). Bode plot of the open-loop transfer function of the speed control loop is seen in Figure 6.15.

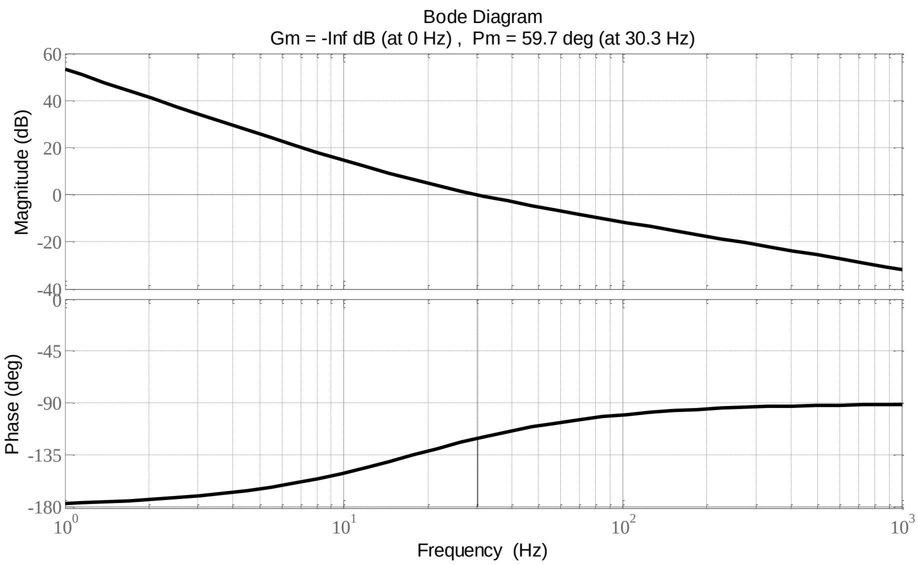

Figure 6.15. Open-loop Bode plot of the speed control loop.

6.7 Simulation Results of the Load Torque Estimator

In this section, the performance of the speed control loop is investigated under different load torque conditions. The current control loop is assumed to be ideal in this part therefore, torque controller and motor pair is replaced by the torque constant K_t. This assumption is done in order to accelerate the simulation because, a few seconds of simulation time is necessary to analyze the speed controller performance and this is not possible with a very small simulation step size which is required to simulate the current control loop.

The performance of the conventional P-I speed controller is tested under different load torque conditions. Then, the load torque estimator is implemented and performances are compared.

Tests are conducted when a constant speed of 600 rpm is commanded. Load drive is commanded to regulate the desired load torque. In Figure 6.16 and Figure 6.17, the speed responses of the drive system are seen when a sinusoidal load torque is applied with frequency 1 Hz and 5 Hz, respectively. In the figures the pink signal shows the desired speed. The cyan signal shows the speed response of the drive system. The blue signal is the applied load torque. As seen, although a constant speed of 600 rpm is commanded, there exists an oscillation on the speed response at the same frequency with the applied load torque. The amplitude of the oscillations increases with the increasing frequency, as can be followed from the comparison of the variables shown in Figure 6.16 and Figure 6.17.

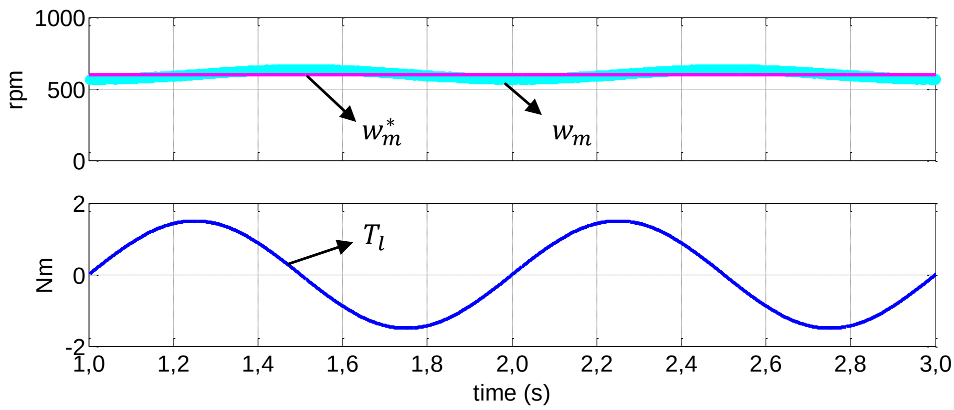

Figure 6.16. Speed command (pink signal), actual speed (cyan signal) and applied load torque (blue signal) in the simulation. Frequency of the load torque is 1 Hz.

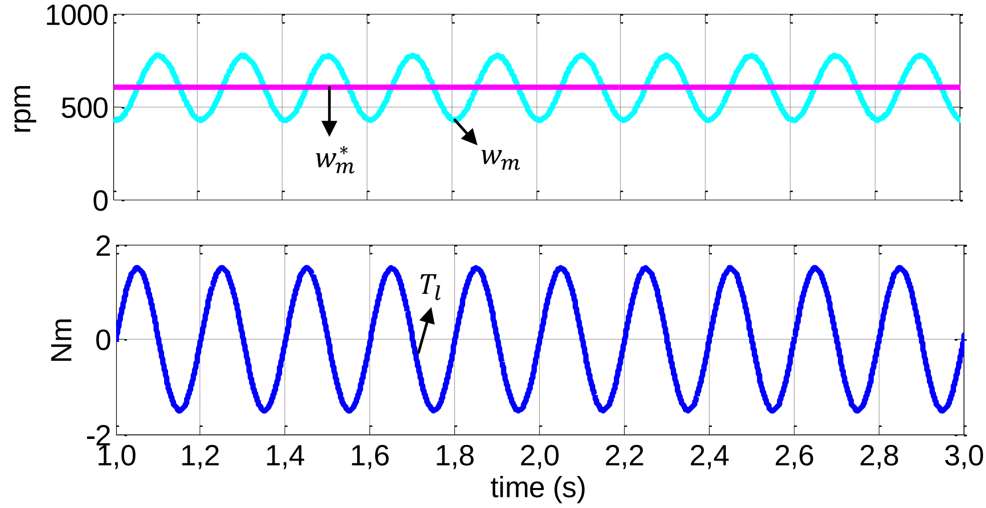

Figure 6.17. Speed command (pink signal), actual speed (cyan signal) and applied load torque (blue signal) in the simulation. Frequency of the load torque is 5 Hz.

The speed controller response can be seen in Figure 6.18 when a step load torque is applied. As can be seen, a perturbation occurs on the shaft speed when the load torque changes. The speed controller rejects this disturbance with a poor transient response.

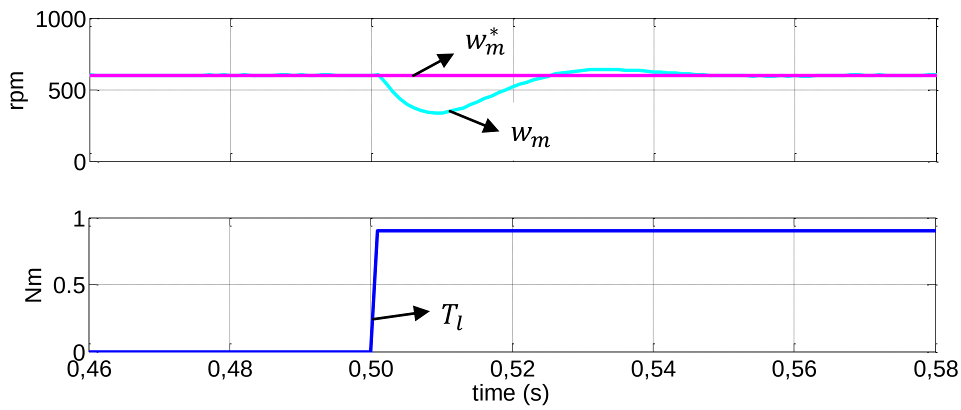

Figure 6.18. Speed command (pink signal), actual speed (cyan signal) and applied load torque (blue signal) in the simulation.

In the second part, load torque estimation algorithm is added to control loop as explained in section 5.4.2 and same tests so far in this section are conducted again. The block diagram of the implementation is seen in Figure 5.16. The load torque is attained by subtracting the net torque from the electromagnetic torque. The electromagnetic torque is calculated by multiplying the q-axis current with the torque constant. The net torque is obtained by multiplying the angular acceleration with the total moments of inertia of the mechanical system.

Angular acceleration is extracted from the velocity measurement by means of a Kalman filter. In order to simulate the noisy velocity measurement, a hypothetical noise with zero-mean is added to the speed measurement. Kalman filter parameters (noise covariances) are set according to the simulated noise.

Speed control response of the drive system with load torque estimator is shown in Figure 6.19 when a sinusoidal load torque with frequency 1 Hz is applied. As seen, oscillations on the speed are nearly vanished compared to that in Figure 6.16 in which the load torque estimator is not implemented. For a sinusoidal load torque with frequency 5 Hz, results are presented in Figure 6.20. Oscillations did not completely vanish but, the amplitude of the oscillation as compared to that in Figure 6.17 is decreased significantly.

The speed controller response when a step load torque is applied is presented in Figure 6.21. It is clear that, the transient response of the speed control loop is improved significantly with load torque estimation.

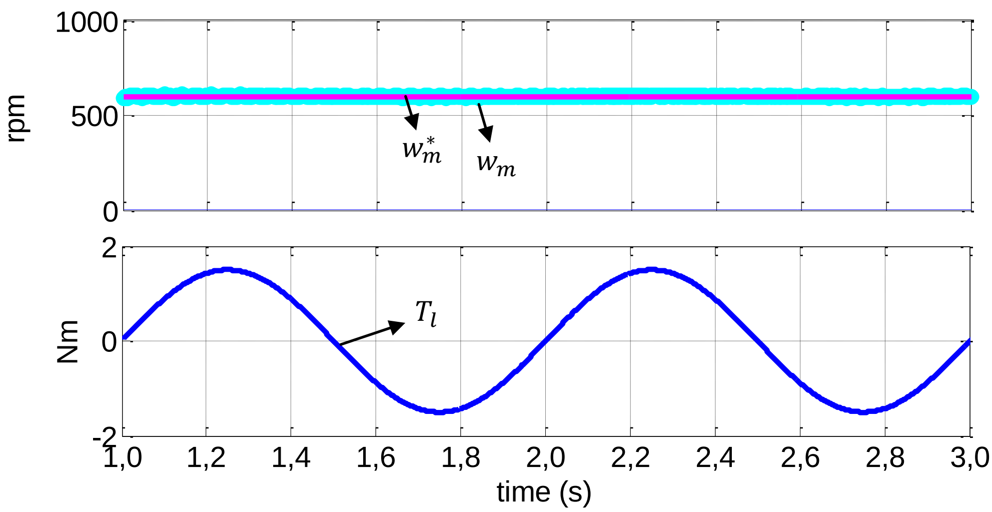

Figure 6.19. Speed command (pink signal), actual speed (cyan signal) and applied load torque (blue signal) with load torque estimator in the simulation. Frequency of the load torque is 1 Hz.

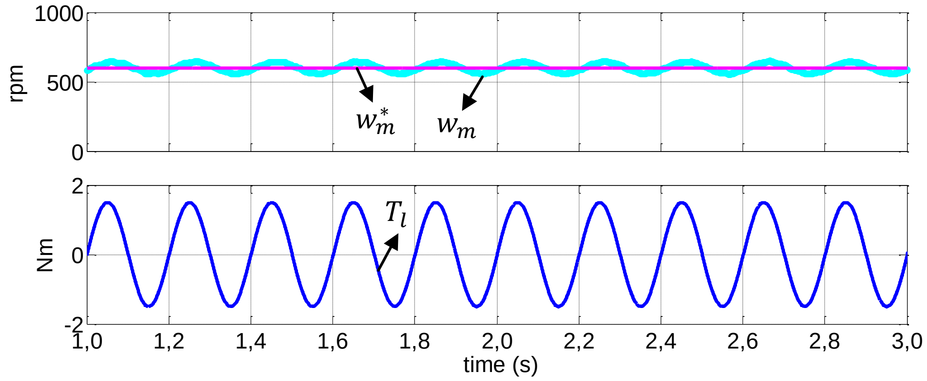

Figure 6.20. Speed command (pink signal), actual speed (cyan signal) and applied load torque (blue signal) with load torque estimator in the simulation. Frequency of the load torque is 5 Hz.

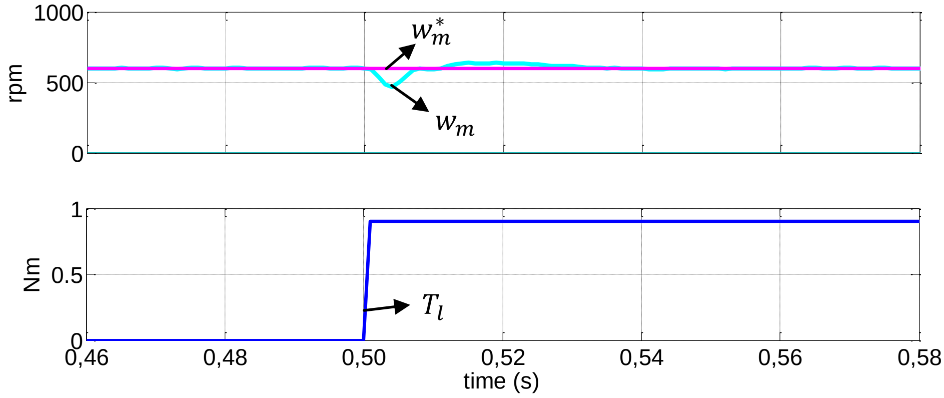

Figure 6.21. Speed command (pink signal), actual speed (cyan signal) and applied load torque (blue signal) with load torque estimator in the simulation.

6.8 Experimental Setup

The drive system has been built and experimental tests are conducted in a laboratory environment. Block diagram of the system is shown in Figure 6.22. Two-level 3-phase VSI module “VWM 270-0075X2” from power semiconductor manufacturer IXYS is used to supply the machine. The VSI module is composed of six power MOSFETs. As a dc source, a battery of 24 V is used. 4.4 mF capacitance is connected to the supply rail of the VSI as near as possible. Half-bridge gate drivers “IX6R11” from IXYS are utilized to bias the gates of the VSI. The gate resistors are chosen to be 10 Ohm. To bias the gates on the same leg of the VSI, 2 isolated voltages are used. Isolated dc/dc converters are utilized for this purpose as demonstrated in Figure 6.23. Digital components should be isolated from the high-power side for the purpose of protection therefore; opto-isolators are used between them.

A surface-mounted permanent-magnet synchronous machine from servo system manufacturer MOOG with the parameters listed in Table 6.3 is used. Another machine with the same parameters is utilized for the load drive. Shafts of the two machines are coupled to each other with mechanical couplings. Two phase currents are measured with current transducers “LEM LA 35-NP”. Measured phase currents are passed through low-pass filters to filter the high-frequency noise from the transducer and the switching harmonics. Then, phase-current information is sampled with analog-to-digital converters (ADC). To detect the rotor angle, a resolver sensor is employed. The output of a resolver sensor composed of two modulated sinusoids. Resolver-to-digital converters (RDC) are utilized to process these modulated signals. The outputs of the RDC are the angle and velocity of the rotor.

A custom DSP-FPGA board is used for digital control of the drive system. On this board, all external interfaces are connected to FPGA. Control loops and algorithms are implemented in the DSP. It takes the inputs (phase currents, rotor angle and velocity) from FPGA, process the necessary functions and gives the outputs back to the FPGA. PWM carrier signal is generated in the FPGA by means of an up-down counter. Duty factors (calculated by DSP) are compared with this counter and PWM signals are constructed within the FPGA. Then, PWM signals are supplied to the gate driver circuitry for current amplification. To monitor the internal signals such as rotor angle, velocity, synchronous frame currents etc. digital-to-analog converters (DAC) are utilized. In order to apply different reference signals (sinusoids with different frequency or step) to the controller, additional ADCs are employed. Signal generator is used for the reference signals.

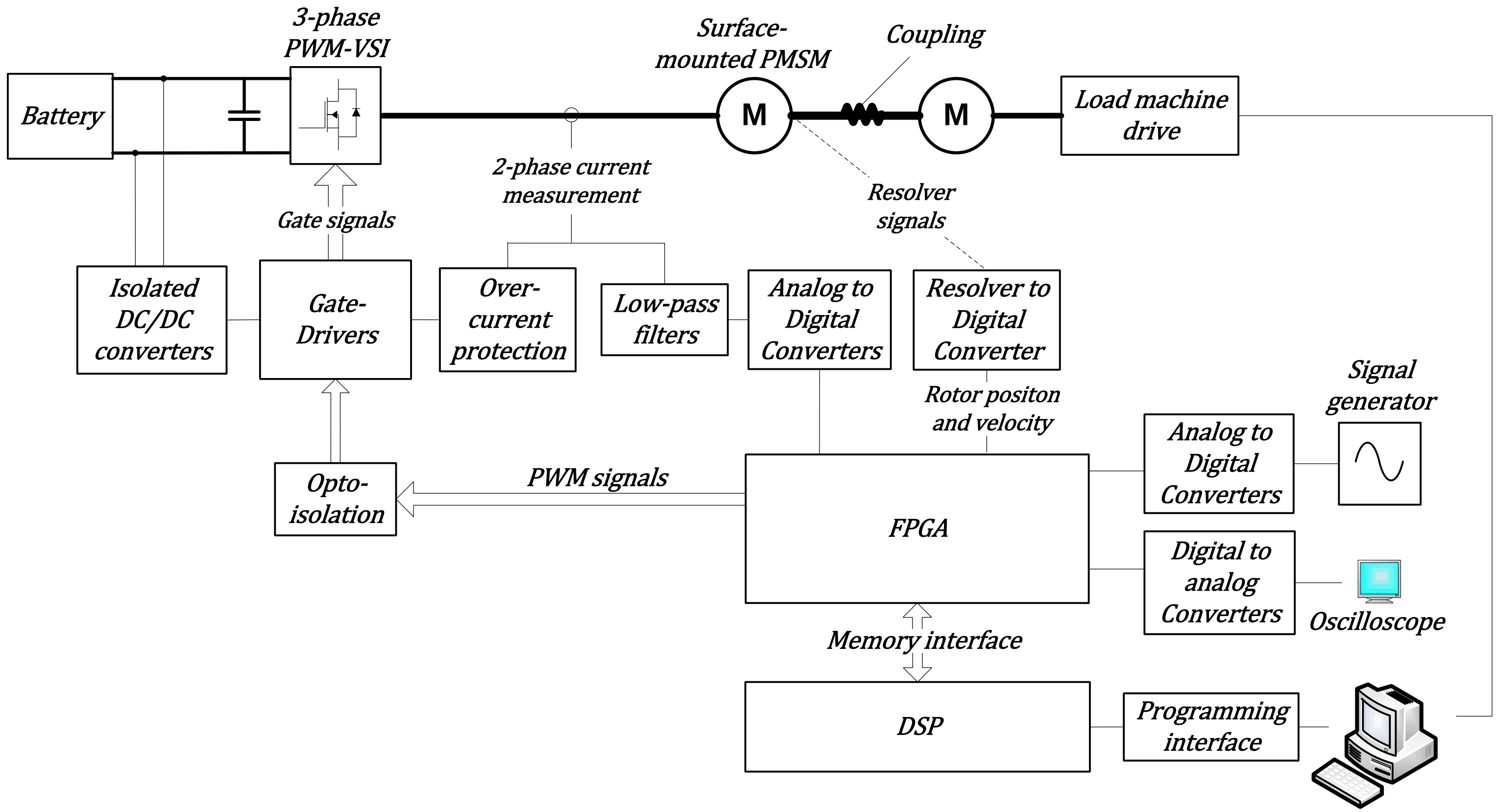

Figure 6.22. Block scheme of the experimental setup.

Table 6.3. Parameters of the test machine.

Pole pair	4	Stator resistance	0.068 Ω
Rated power	385 W	Stator inductance	0.079 mH
Rated speed	2300 rpm	Torque constant	0.086 Nm/Arms
Rated current	18.5 A	Rated torque	1.6 Nm
d-axis inductance	0.12 mH	q-axis inductance	0.12 mH
Rotor inertia	0.5 kgcm^2		

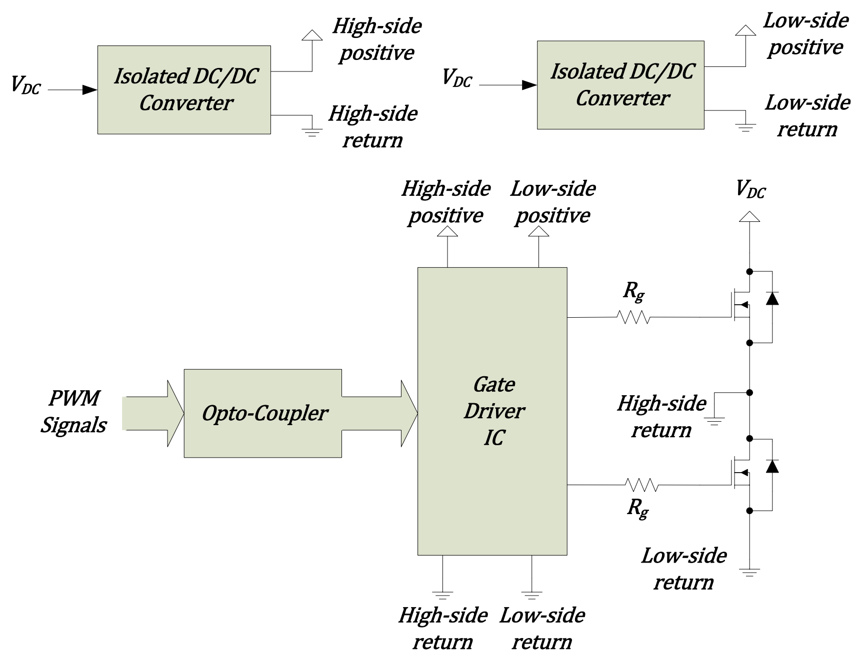

Figure 6.23. Gate drive circuitry for one leg of the inverter.

“TMS320C6713”, a DSP from Texas Instruments (TI) is programmed via its software Code Composer Studio by means of a debugger. The control loops and algorithms are developed in the Matlab/Simulink software and the generated C-code is transferred to Code Composer Studio software. Then, the code is compiled and loaded to the DSP.

Load machine is controlled with a two-axis servo controller manufactured by ASELSAN Inc. which has torque and speed control capability. Its interface is the CANopen protocol. A USB to CAN adapter is used to send commands to the servo controller via a PC. A picture of the experimental setup is given in Figure 6.24.

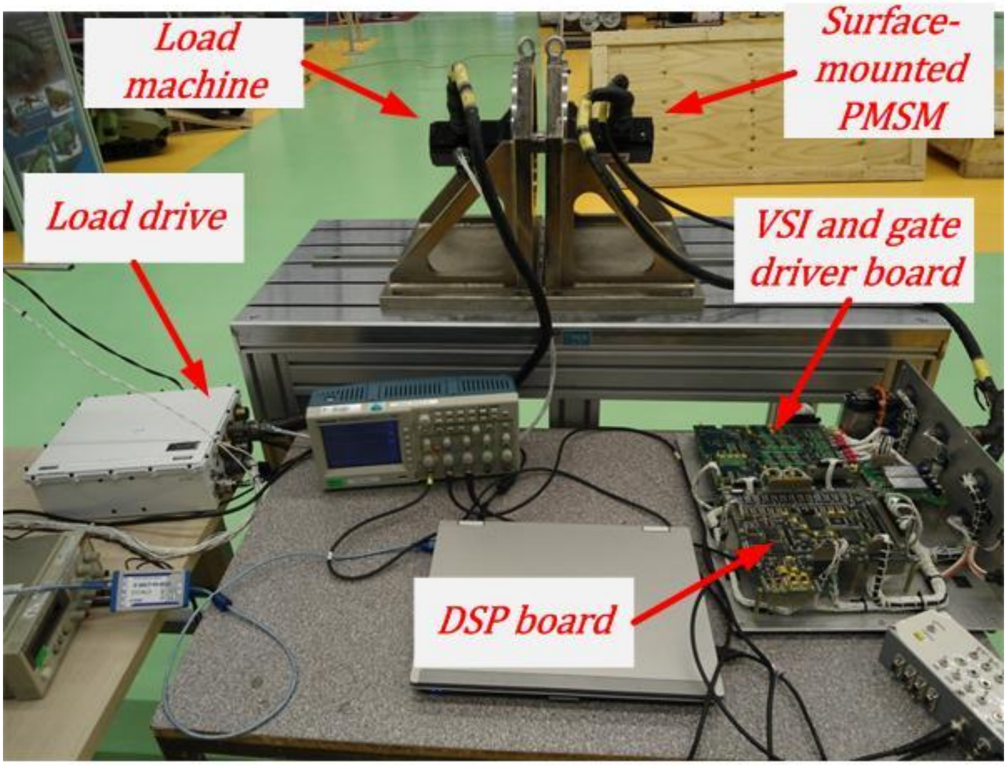

Figure 6.24. Experimental setup.

6.9 Experimental Results of the Volt-Second Compensation

In order to test the volt-second compensation algorithm, firstly, synchronous frame P-I current regulator is implemented then, compensation algorithm is added to control loop and results are compared.

Triangular carrier signal of 10 KHz is generated within the FPGA. Dead-time is adjusted to 2 microseconds. Synchronous frame current regulator is implemented in the DSP. Sampling frequency is set to 10 KHz. P-I controllers are utilized with parameters provided in Table 6.4. Same parameters are used for q- and d-axis current regulators. Parameters are tuned such that the bandwidth of the closed-loop system is approximately 300 Hz. Space vector PWM algorithm is implemented within the DSP as explained in section 3.3.

Table 6.4. Parameters of the P-I current controllers in experimental work.

Proportional constant, K_p	0.25
Integral constant, K_i	130

Tests are conducted at two different operating speeds of the machine, 300 rpm and 600 rpm, to investigate the response of the control loop and volt-second compensation algorithm at different frequencies. 10 Ampere quadrature-axis synchronous current (i_{sq}) is commanded. Direct-axis current (i_{sd}) is commanded as zero. Load servo drive is commanded to regulate the shaft speed.

Phase current is measured by a clamp meter and monitored on an oscilloscope. When machine operates at 300 rpm, the measured phase current is as shown in Figure 6.25. The frequency of the phase current is 20 Hz as expected according to (6.7).

$$n_s = \frac{120 f_e}{P}\,. \tag{6.7}$$

The synchronous speed n_s is 300 rpm and number of poles is 8 so, the excitation frequency is 20 Hz.

Distortion in the phase current waveform is evident. Fast Fourier Transform (FFT) of the current is also provided in the figure. In section 5.2.1, it is stated that, distorted output voltage of the VSI give rise to 6n±1 (n: 1, 2...) harmonics on the phase current waveform. Experimental results confirm this statement. There exists 5^{th} and 7^{th} harmonic components in frequency spectrum (100 Hz and 140 Hz). Frequency of the harmonics is shown with cursors at the upper right of the screenshot. The zero-level of the current is shown with the channel number of the scope at the left sight of the screenshot.

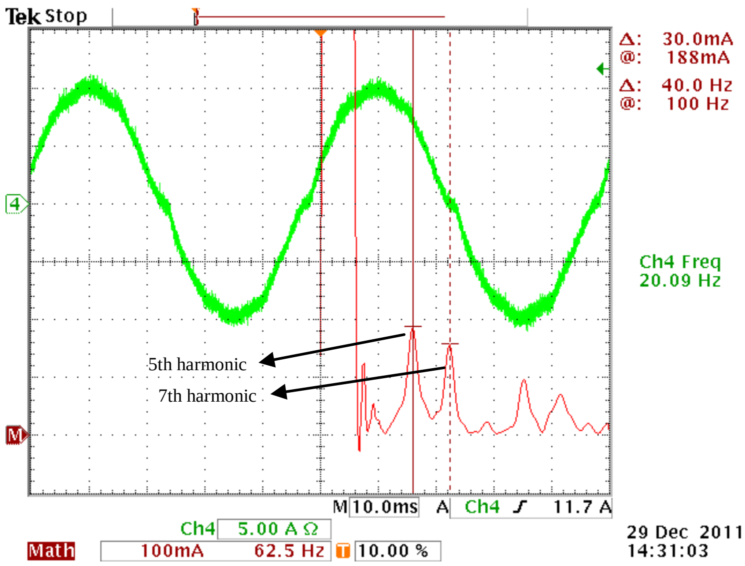

Figure 6.25. Phase current waveform and FFT of the phase current with synchronous frame P-I current regulator obtained experimentally when machine operates at 300 rpm.

In section 5.2.1, it is also stated that, distorted output voltage of the VSI give rise to sixth harmonic on the synchronous frame currents (i_{sq} and i_{sd}). Synchronous frame currents calculated within the DSP, are also monitored via digital-to-analog converters. These waveforms are presented in Figure 6.26. As noted, there exist ripple at the sixth harmonic of the fundamental frequency (120 Hz) on the current waveforms. Frequency of the ripple is shown with cursors at the upper right of the screenshot. The zero-level of the current is shown with the channel number of the scope at the left sight of the screenshot. Zero-levels of the channel-1 and channel-2 are at the same level. In the figure, a division in the vertical-axis corresponds to 2.5 Ampere.

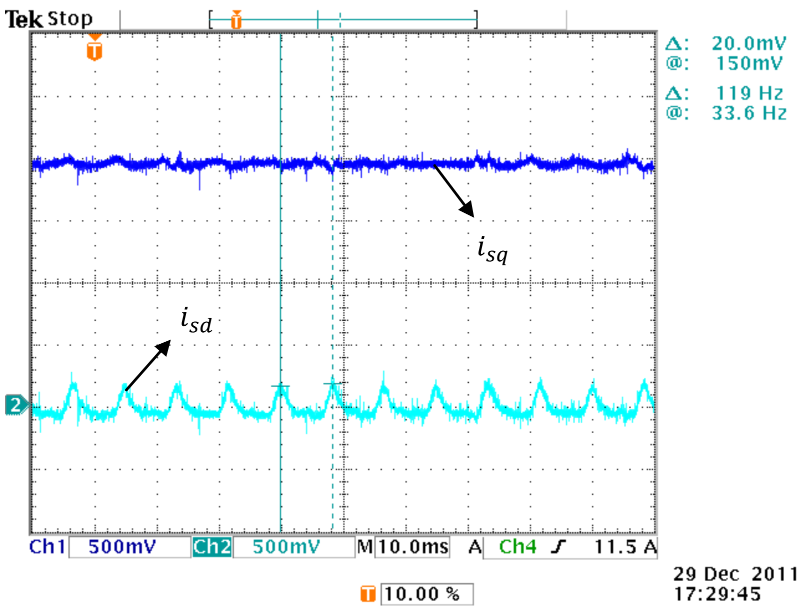

Figure 6.26. Synchronous frame current waveforms with synchronous frame P-I current regulator obtained experimentally when machine operates at 300 rpm. quadrature-axis current (blue), direct-axis current (light-blue) (2.5A per division)

Phase current and FFT of the phase current is also monitored when the machine operates at 600 rpm. Phase current waveform and FFT of the phase current and synchronous frame currents are shown in Figure 6.27 and Figure 6.28 respectively. Fundamental frequency is 40 Hz for 600 rpm synchronous speed. The phase current waveform is still distorted and 5^{th} and 7^{th} harmonics components exist in frequency spectrum (200 Hz and 280 Hz). In Figure 6.28, the zero-level of the current is shown with the channel number of the scope at the left sight of the screenshot. Zero-levels of the channel-1 and channel-3 are at the same level. In the figure, a division in the vertical-axis corresponds to 2.5 Ampere.

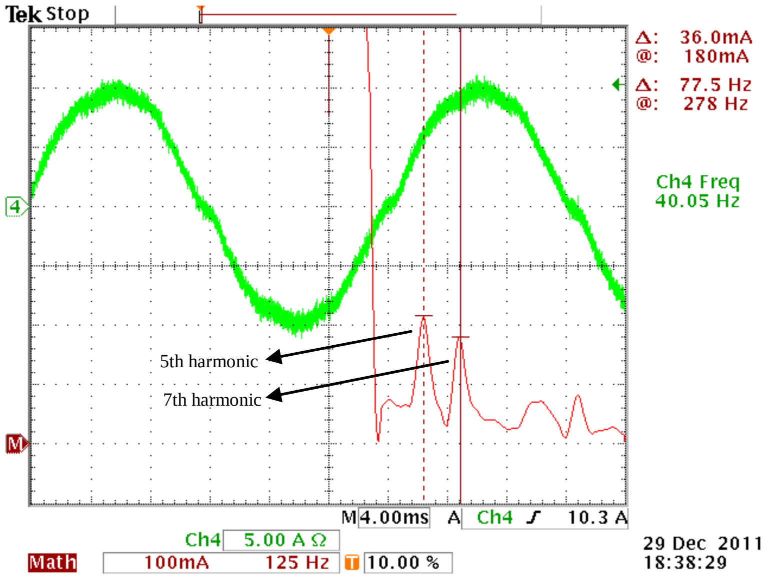

Figure 6.27. Phase current waveform and FFT of the phase current with synchronous frame P-I current regulator obtained experimentally when machine operates at 600 rpm.

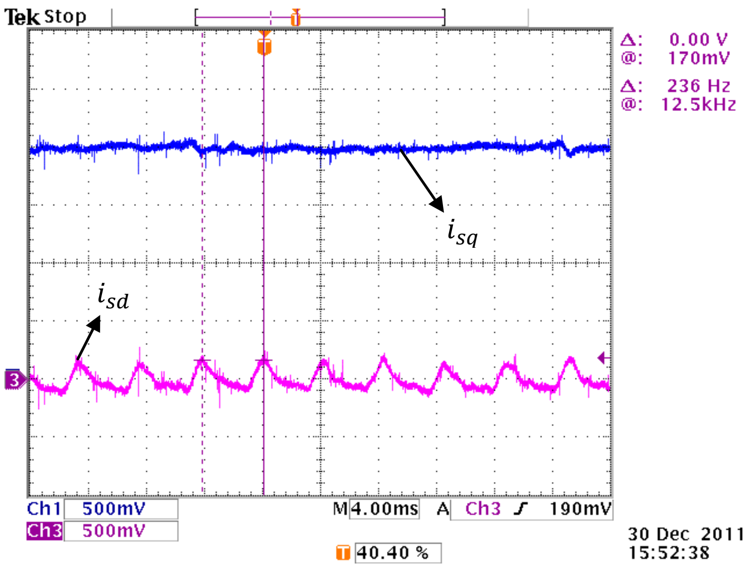

Figure 6.28. Synchronous frame current waveforms with synchronous frame P-I current regulator obtained experimentally when machine operates at 600 rpm. quadrature-axis current (blue), direct-axis current (magenta) (2.5A per division)

In the second part of the test, volt-second compensation algorithm is implemented as explained in section 5.2.2 and as demonstrated in Figure 5.6. Diode forward voltage drop is found with an off-line experiment as 0.65 V. Turn-on/off times are found approximately as 0.2 and 0.7 microseconds respectively. Polarities of the phase currents are determined according to current space vector angle as in Table 5.2. As stated before, this angle is the summation of the torque angle δ and rotor angle θ_r. Torque angle is set to ninety degree (zero direct-axis current). Rotor angle θ_r is measured via the resolver sensor. Compensation times which are the outputs of the volt-second compensation block are added to the desired on-time values calculated by SFCR as demonstrated in Figure 5.6.

When the machine operates at 300 rpm, with volt-second compensation algorithm, phase current waveform and FFT of the phase current are shown in Figure 6.29. Synchronous frame currents are presented in Figure 6.30. In the figures, the zero-level of the currents are shown with the channel number of the scope at the left sight of the screenshot. In Figure 6.30, zero-levels of the channel-1 and channel-2 are at the same level and a division in the vertical-axis corresponds to 2.5 Ampere.

As can be seen, quality of the phase current waveform is improved significantly and 5^{th} and 7^{th} harmonic components are diminished to zero. The ripples on the synchronous frame currents are nearly vanished.

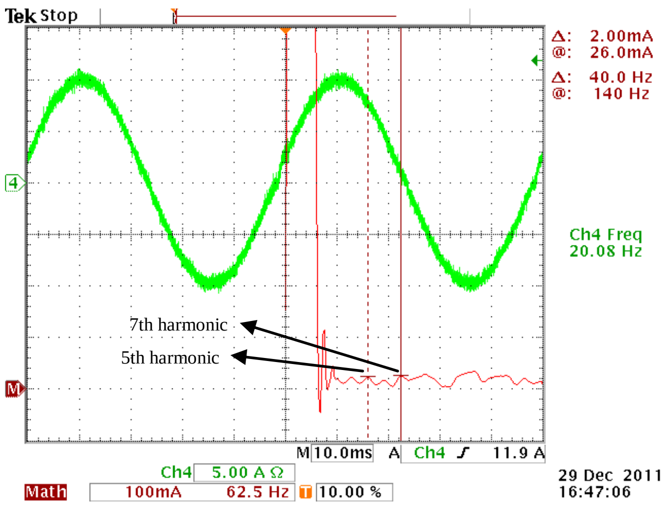

Figure 6.29. Phase current waveform and FFT of the phase current with volt-second compensation algorithm obtained experimentally when machine operates at 300 rpm.

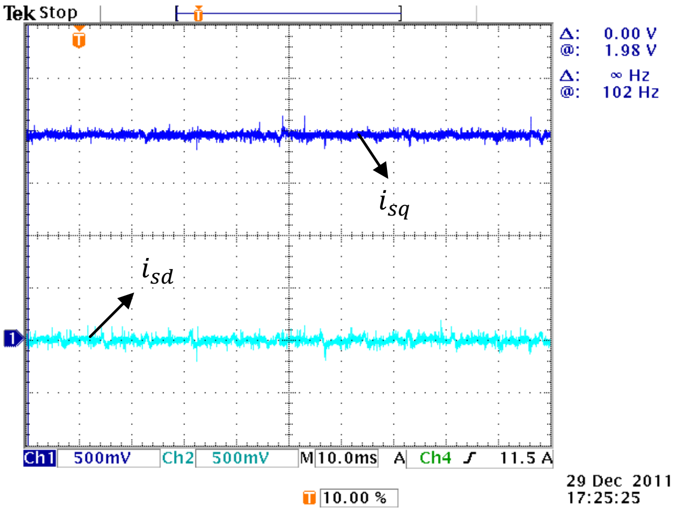

Figure 6.30. Synchronous frame currents with volt-second compensation algorithm obtained experimentally when machine operates at 300 rpm. quadrature-axis current (blue), direct-axis current (light-blue) (2.5A per division)

To test the algorithm at a different frequency, machine is operated at 600 rpm and same measurements are taken again. The results are given in Figure 6.31 and Figure 6.32. In the figures, the zero-level of the currents are shown with the channel number of the scope at the left sight of the screenshot. In Figure 6.32, zero-levels of the channel-1 and channel-3 are at the same level and a division in the vertical-axis corresponds to 2.5 Ampere.

As observed, volt-second compensation algorithm still improves the phase waveform quality and suppresses the ripples on the synchronous frame currents. However, it is also evident that the results are not perfect as in 300 rpm case because, it becomes more difficult to match the compensation voltage with the disturbance voltage caused by the inverter when the frequency increases due to the inherent delays in the sampling and digital processing.

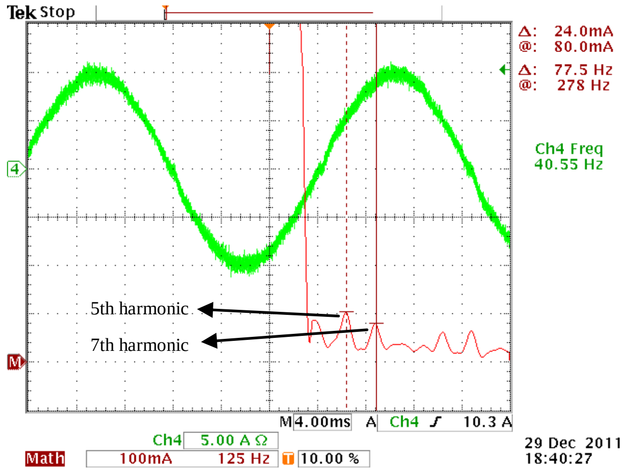

Figure 6.31. Phase current waveform and FFT of the phase current with volt-second compensation algorithm obtained experimentally when machine operates at 600 rpm.

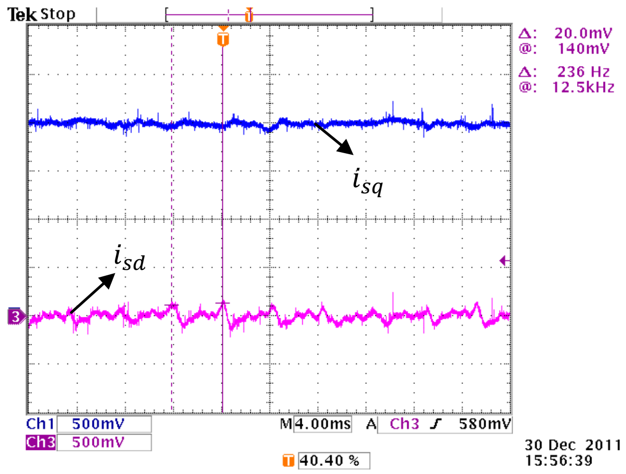

Figure 6.32. Synchronous frame currents with volt-second compensation algorithm obtained experimentally when machine operates at 600 rpm. quadrature-axis current (blue), direct-axis current (magenta) (2.5A per division)

Result of the experiments in this section can be summarized as follows: P-I controllers can reject the disturbance voltage caused by the non-ideal VSI, up to a certain extent, since they have a finite bandwidth. Due to practical reasons, it is not possible to increase the bandwidth indefinitely. Therefore, disturbance rejection capability of the drive system can be improved by implementing the proposed compensation algorithm. The experimental results show the effectiveness of this method. Phase current distortion has been reduced. Magnitude of the ripples on the synchronous frame currents has been decreased. To determine the direction of the current, rotor angle information is used rather than using current transducers. Therefore, the problems regarding to switching nature of the current has been eliminated.

The performance of the algorithm decreases with increasing frequency of the electrical excitation nevertheless, its contribution is still positive. With the volt-second compensation algorithm, there is still some distortion in the phase current especially when the corresponding phase or other phase currents cross the zero. This is due to the *zero-current clamping* phenomena.

6.10 Experimental Results of the Decoupling Method

In section 5.3.1, it has been explained that, components related to the permanent-magnet flux linkage and d-axis flux linkage can be interpreted as disturbance inputs on the q-axis. As for d-axis, component related to the q-axis flux linkage can be treated as a disturbance input. In this section, effects of these disturbance inputs are examined. Method to improve the disturbance rejection capability of the controller is examined.

Load servo drive is commanded with sinusoidal signals for speed regulation at different frequencies. Parameters of the P-I current controllers are set again as given in Table 6.4.

First test is done when the load servo drive changes the shaft speed sinusoidally. The frequency of the sinusoidal is 2 Hz and magnitude of it is 600 rpm. The drive system under test is commanded with 10 Ampere constant q-axis synchronous frame current (i_{sq}). d-axis current (i_{sd}) is commanded as zero. In Figure 6.33, shaft speed (cyan signal) and q-axis current (blue signal) are shown. The zero-level of the shaft speed and q-axis current are shown with the channel numbers of the scope at the left sight of the screenshot. In the figure, for the shaft speed; one volt corresponds to 240 rpm and for the q-axis current; a division in the vertical-axis corresponds to 2.5 Ampere.

From the figure it is seen that, there exists an oscillation on the q-axis current with the same frequency of the shaft speed although a constant current of 10 Ampere is commanded.

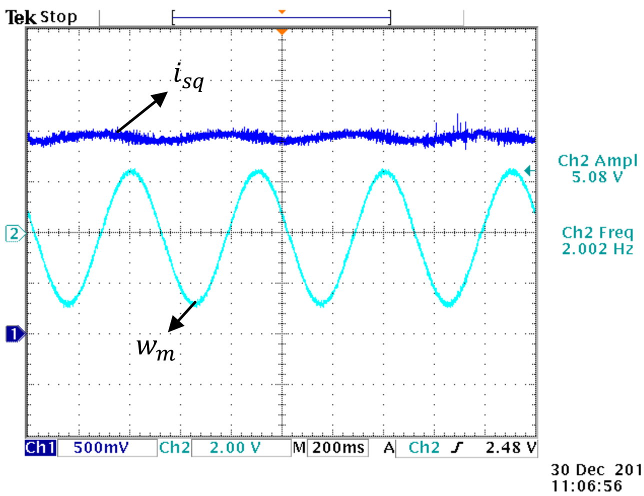

Figure 6.33. Shaft speed (cyan signal, 240 rpm per volt) and q-axis current response (blue signal, 2.5A per division) obtained experimentally when the shaft speed changes sinusoidally (magnitude: 600 rpm, frequency: 2 Hz).

Similar test is conducted when the load servo drive changes the shaft speed sinusoidally again. The frequency of the sinusoidal is 5 Hz and magnitude of it is 600 rpm. Shaft speed and q-axis current are shown in Figure 6.34. Oscillation on the q-axis current is clearer for this case.

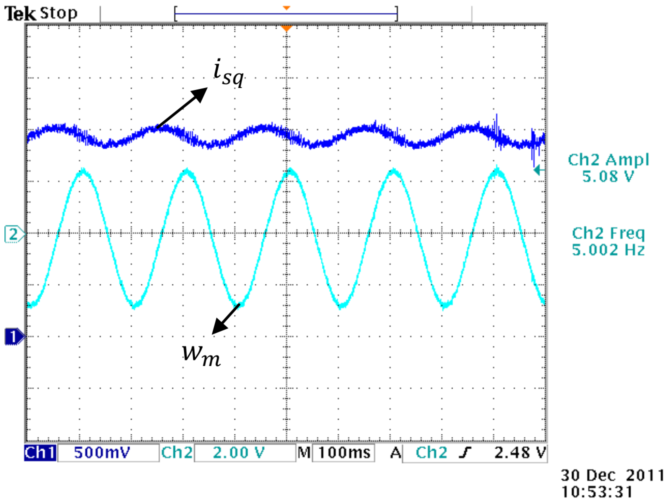

Figure 6.34. Shaft speed (cyan signal, 240 rpm per volt) and q-axis current response (blue signal, 2.5A per division) obtained experimentally when the shaft speed changes sinusoidally (magnitude: 600 rpm, frequency: 5 Hz).

Another test is done when a step change occurs on the shaft speed. A distortion on the q-axis current is observed when the shaft speed changes rapidly as depicted in Figure 6.35.

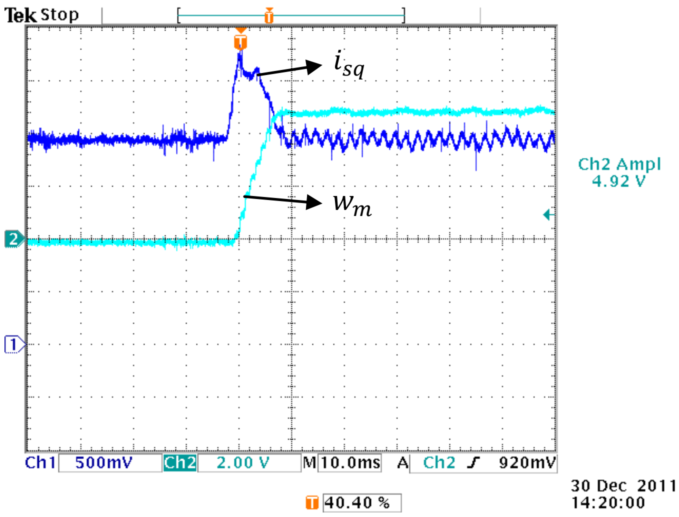

Figure 6.35. Shaft speed (cyan signal, 240 rpm per volt) and q-axis current response (blue signal, 2.5A per division) obtained experimentally when a 600 rpm step change occurs on the shaft speed.

To improve the response of the current controller, decoupling method described in section 5.3.2 is implemented as demonstrated in Figure 5.12. q- and d- axes inductances are found approximately as 0.13 mH with an off-line test. Gain of the inverter is assumed to be unity.

Same tests are repeated with the decoupling method. First test is done when the load servo drive changes the shaft speed sinusoidally. The frequency of the sinusoidal is 2 Hz and magnitude of it is 600 rpm. The tested drive system is commanded with 10 Ampere constant q-axis synchronous current, i_{sq}. d-axis current, i_{sd} is commanded as zero. The results can be seen in Figure 6.36. The zero-level of the shaft speed and q-axis current are shown with the channel numbers of the scope at the left sight of the screenshot. In the figure, for the shaft speed; one volt corresponds to 240 rpm and for the q-axis current; a division in the vertical-axis corresponds to 2.5 Ampere.

Oscillations on the q-axis current nearly vanished with the implemented decoupling method. The results for the 5 Hz case are demonstrated in Figure 6.37.

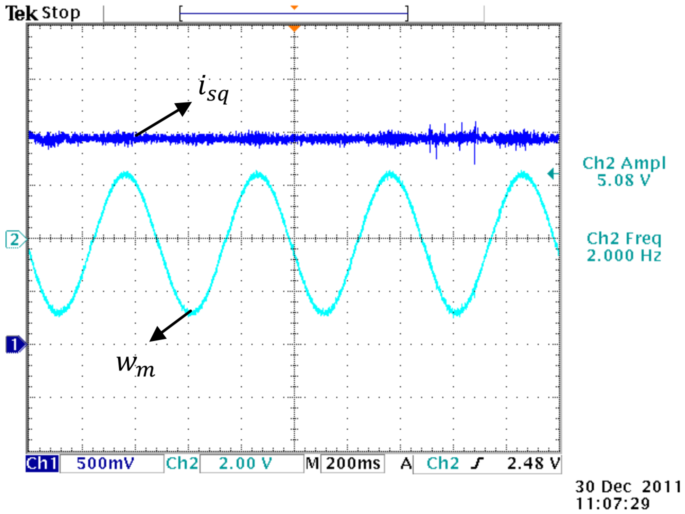

Figure 6.36. Shaft speed (cyan signal, 240 rpm per volt) and q-axis current response (blue signal, 2.5A per division) with decoupling method obtained experimentally when the shaft speed changes sinusoidally (magnitude: 600 rpm, frequency: 2 Hz).

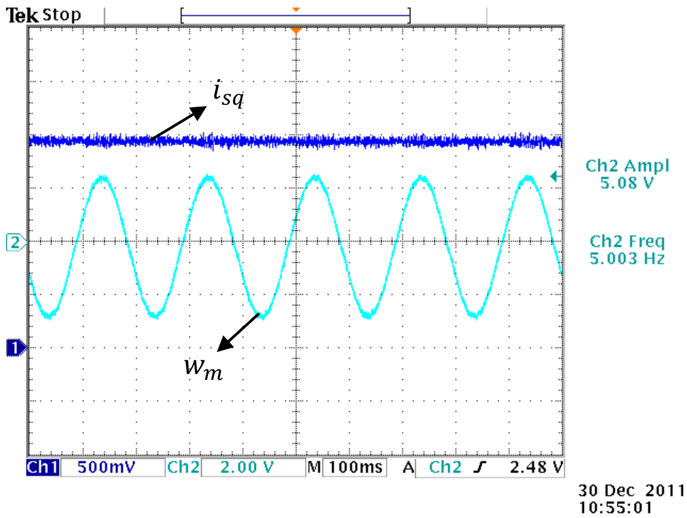

Figure 6.37. Shaft speed (cyan signal, 240 rpm per volt) and q-axis current response (blue signal, 2.5A per division) with decoupling method obtained experimentally when the shaft speed changes sinusoidally (magnitude: 600 rpm, frequency: 5 Hz).

For a step change on the shaft speed, q-axis current is shown in Figure 6.38. As compared to Figure 6.35 where the decoupling method has not been implemented; there is a significant improvement in the transient response of the current controller.

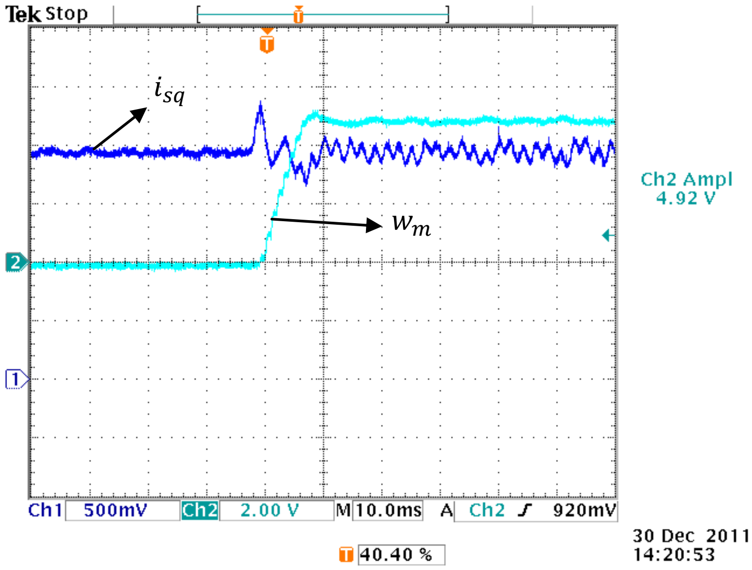

Figure 6.38. Shaft speed (cyan signal, 240 rpm per volt) and q-axis current response (blue signal, 2.5A per division) with decoupling method obtained experimentally when a 600 rpm step change occurs on the shaft speed.

6.11 Experimental Results of the Load Torque Estimator

In this section, firstly, the performance of the conventional P-I speed controller is analyzed. Then, the load torque estimator is added to system and the resulting performances are compared.

During the tests conducted in this part, load drive is commanded with different signals for torque regulation. The tested drive system tries to regulate the shaft speed under different load torque conditions. Speed controller is implemented with P-I regulator with the parameters given in Table 6.5.

Table 6.5. Parameters of the speed controller.

Proportional constant, K_{ps}	0.27
Integral constant, K_{is}	30

The drive system under test is commanded with 600 rpm constant speed. The speed responses are seen in Figure 6.39, Figure 6.40 and Figure 6.41 for 1 Hz, 5 Hz and 10 Hz sinusoidal load torque respectively. In the figures the pink signal represents the desired speed of the tested drive system. Cyan signal shows the speed response of the controller. The blue signal is the output of the load torque estimator. The zero-level of the variables are shown with the channel number of the scope at the left sight of the screenshot. Zero-levels of the channel-2 and channel-3 are at the same level. In the figure, for the shaft speed; one volt corresponds to 240 rpm and for the load torque; one volt corresponds to 0.29 Nm. As can be seen, although a constant speed of 600 rpm is commanded, there exists an oscillation in the speed response with the same frequency of the applied load torque. Amplitude of the oscillations grows with the increasing frequency.

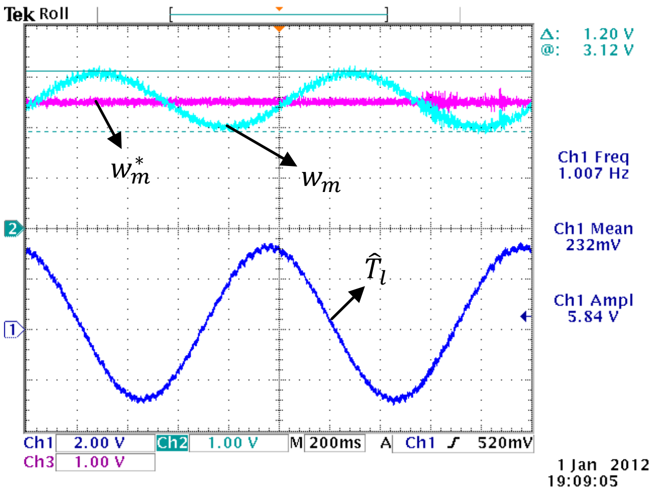

Figure 6.39. Commanded speed (pink signal), actual speed (cyan signal, 240 rpm per volt) and estimated load torque (blue signal, 0.29 Nm per volt) obtained experimentally when the load torque changes sinusoidally with frequency 1 Hz.

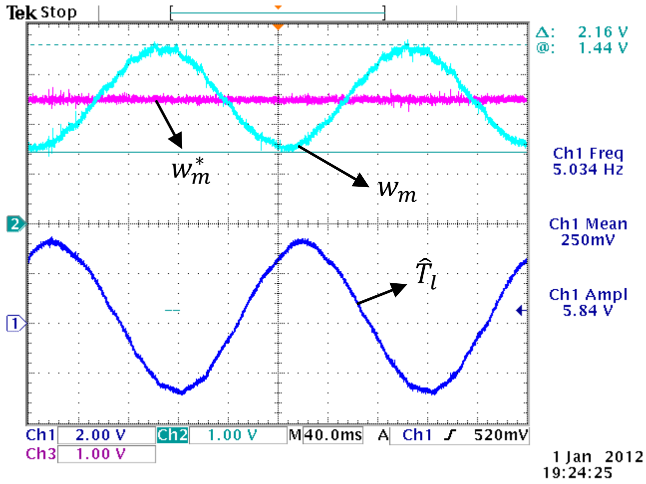

Figure 6.40. Commanded speed (pink signal), actual speed (cyan signal, 240 rpm per volt) and estimated load torque (blue signal, 0.29 Nm per volt) obtained experimentally when the load torque changes sinusoidally with frequency 5 Hz.

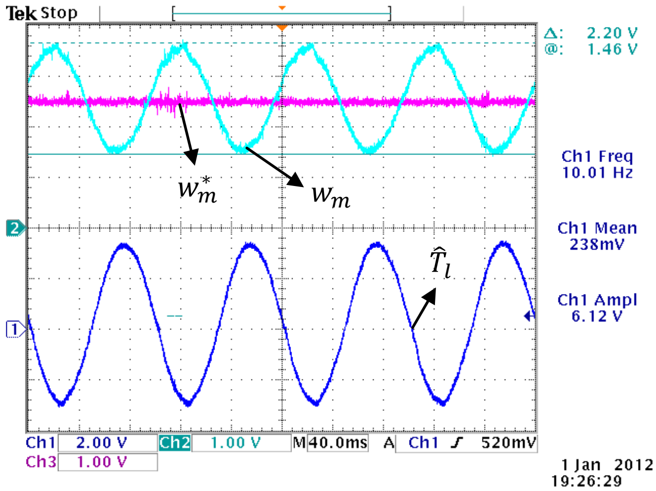

Figure 6.41. Commanded speed (pink signal), actual speed (cyan signal, 240 rpm per volt) and estimated load torque (blue signal, 0.29 Nm per volt) obtained experimentally when the load torque changes sinusoidally with frequency 10 Hz.

Another test is conducted when a step load torque is applied. Obtained results are demonstrated in Figure 6.42. When the step load torque is applied, a perturbation occurs on the shaft speed. The speed controller regulates the speed to the desired value but, with a poor transient response.

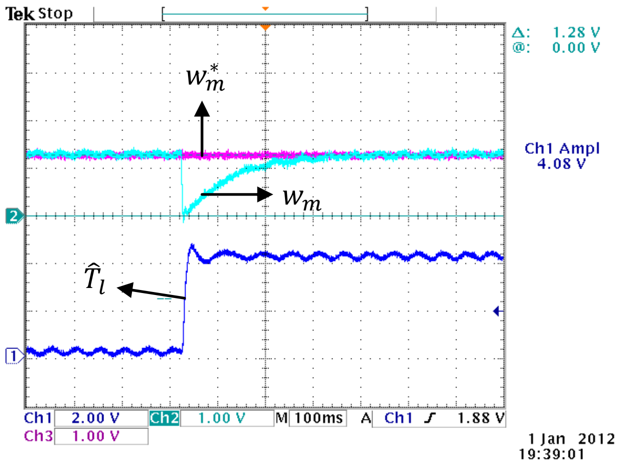

Figure 6.42. Commanded speed (pink signal), actual speed (light-blue signal, 240 rpm per volt) and estimated load torque (blue signal, 0.29 Nm per volt) obtained experimentally when a step change occurs on the load torque.

In the second part, load torque estimation algorithm is added to control loop and the same tests in this section are conducted again. Measurement noise covariance needed for the Kalman filter is found by an experiment on the speed sensor. A set of speed data is collected when the drivers are disabled (zero shaft speed). This data set is processed by MATLAB software and the covariance of the data set is calculated as 10.2475. The mean of the data is found as 2.7391. As stated before, non-zero-mean noise components are cancelled out by compensating the offset at the start of every operation.

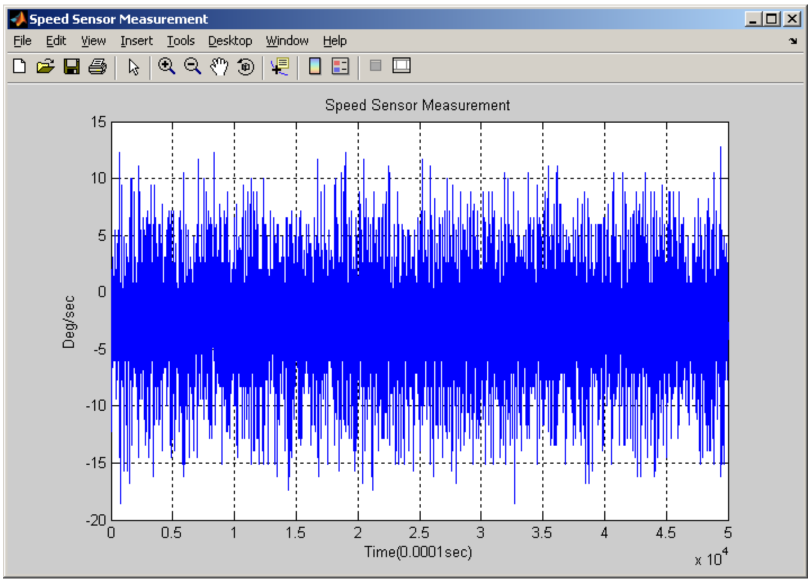

Figure 6.43. The data collected from the speed sensor when the shaft is not moving.

Another need for the Kalman filter is the process noise covariance. As stated before, process noise covariance cannot be obtained by an analytical process or by a test. It should be tuned according to frequency response of the Kalman filter. Therefore, various values for process noise covariance are used as trials for the process noise covariance and the optimum value is found to be 10^7. When this value is increased further, the filter weighs the measurements more heavily therefore, it amplifies the sensor noise. Decreasing the covariance causes that, the filter weighs the system model more heavily instead of sensor data. In this case, the filter becomes more sluggish. The covariance is adjusted such that, the filter can estimate the sinusoidal signals up to 10 Hz.

The initial state estimate for the filter is set to the zero vector. The initial state estimate error covariance, P_0^+ is chosen as in (6.8). As stated before, the initial estimates only affect the starting behavior of the filter.

$$P_0^+ = \begin{bmatrix} 0.01 & 0 & 0 \\ 0 & 0.01 & 0 \\ 0 & 0 & 0.01 \end{bmatrix}. \tag{6.8}$$

The torque constant of the machine is used as the same specified by the manufacturer. To calculate the load torque, total moments of inertia of the mechanical system is needed. Therefore, a test has been done to find it. A pulsed torque is exerted on the total moments of inertia and the speed of is measured. Then, effective inertia is calculated according to (2.54) and is found to be 1.06 $kgcm^2$.

The speed responses with load torque estimator are seen in Figure 6.44, Figure 6.45 and Figure 6.46 for 1 Hz, 5 Hz and 10 Hz sinusoidal load torque respectively. The drive system under test is commanded with a constant speed of 600 rpm. In the figures, the pink signal represents the desired speed of the tested drive system. Cyan signal shows the speed response of the controller. The blue signal is the output of the load torque estimator. The zero-level of the variables are shown with the channel number of the scope at the left sight of the screenshot. Zero-levels of the channel-2 and channel-3 are at the same level. In the figure, for the shaft speed; one volt corresponds to 240 rpm and for the load torque; one volt corresponds to 0.29 Nm.

As can be seen from the figures, there is a significant improvement in the speed performance of the drive when the load torque estimator is implemented. The oscillations in the 1 Hz case are nearly vanished. For the 5 Hz and 10 Hz cases, a considerable decrease is observed in the magnitude of the oscillations.

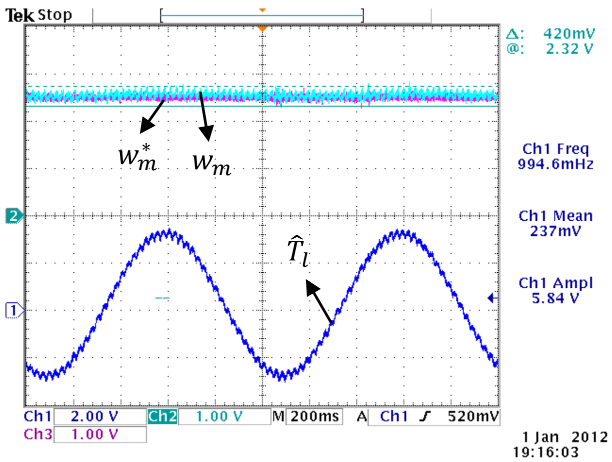

Figure 6.44. Commanded speed (pink signal), actual speed with load torque estimation (cyan signal, 240 rpm per volt) and estimated load torque (blue signal, 0.29 Nm per volt) obtained experimentally when the load torque changes sinusoidally with frequency 1 Hz.

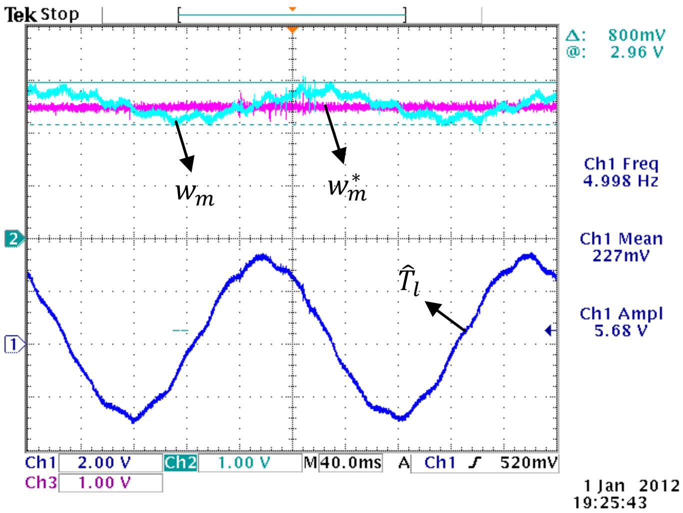

Figure 6.45. Commanded speed (pink signal), actual speed with load torque estimation (cyan signal, 240 rpm per volt) and estimated load torque (blue signal, 0.29 Nm per volt) obtained experimentally when the load torque changes sinusoidally with frequency 5 Hz.

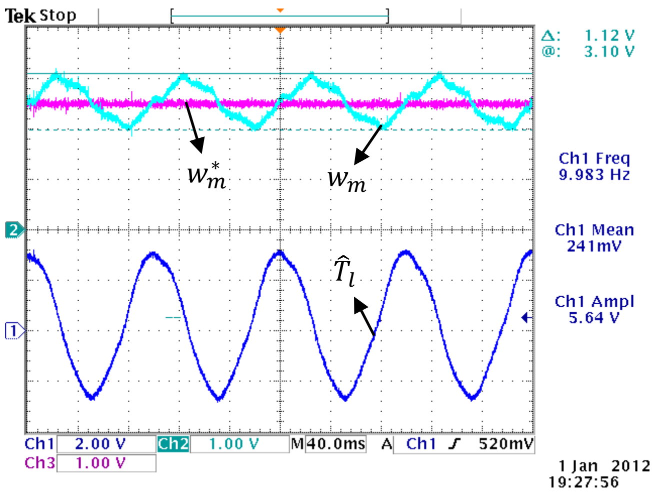

Figure 6.46. Commanded speed (pink signal), actual speed with load torque estimation (cyan signal, 240 rpm per volt) and estimated load torque (blue signal, 0.29 Nm per volt) obtained experimentally when the load torque changes sinusoidally with frequency 10 Hz.

Step load torque test is repeated when the load torque estimator is utilized and the results are presented in Figure 6.47. Compared to results given in Figure 6.42, it can be concluded that, a better transient response is achieved with the load torque estimator.

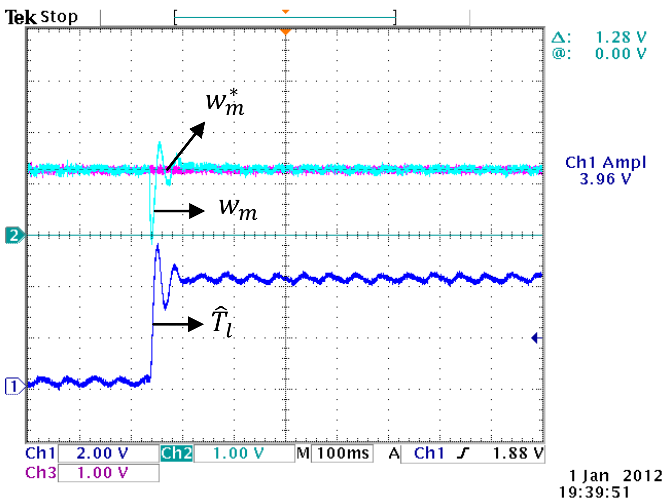

Figure 6.47. Commanded speed (pink signal), actual speed with load torque estimation (light-blue signal, 240 rpm per volt) and estimated load torque (blue signal, 0.29 Nm per volt) obtained experimentally when a step change occurs on the load torque.

6.12 Discussions on the Experimental Results

In the first part of the experimental tests, the effect of the non-ideal behavior of the MOSFET inverter on the stationary frame and synchronous frame currents has been examined. Then, the volt-second compensation algorithm is utilized and performance improvement is examined. To determine the direction of the current, rotor angle information is used rather than using current transducer and the problems regarding to switching nature of the current is eliminated. Note that, this method does not require the d-axis current to be zero. Experimental results show significant improvements in phase currents and synchronous frame currents that means, a better torque control is achieved.

In the second part of the experiments, effect of the coupling variables on the current control performance is studied. It has been examined that, the q-axis current control performance is degraded when a change occurs in the shaft speed. The decoupling algorithm is implemented and tested to improve the current controller performance. A considerable improvement is achieved in the current control performance with decoupling method.

The last part of the experiments is about the load torque estimation algorithm. Firstly, the conventional P-I speed regulator performance is tested. Then, load torque estimator is designed and added to the system then, same tests are repeated. Speed regulation performance of the drive system is also improved significantly.

CHAPTER 7

CONCLUSION

A common problem in the electric drive systems is the nonlinearity of the power converter due to nonideal characteristics of the power semiconductors. In this thesis, the volt-second compensation algorithm is applied to resolve this problem. The nonlinearity of the VSI is investigated in detail. Not only the effect of dead-time but also the effect of the device voltage drop and turn-on/off times of the power switches are also examined. Then, the volt-second algorithm is analyzed theoretically, and implemented and tested in simulation and in experimental work.

Volt-second compensation method uses the information of the phase current direction to compensate the volt-second error introduced by the VSI. In this study, rather than using current transducer to determine the direction of the current, rotor angle information is used and the problems regarding to switching nature of the current is eliminated successfully. After the implementation of the volt-second method, simulation and experimental results show significant improvements in phase current and synchronous frame current waveforms. The magnitude of the oscillations on the synchronous frame currents is decreased approximately by 60% when the machine operates at a speed of 300 rpm.

Although volt-second compensation improves the phase current waveform, there are still distortions on it, especially in zero-crossings of the phase currents. This is due to the so-called zero-current clamping phenomenon. When the phase current is close to zero, during the dead-time, current decreases to zero and remains there during the rest of the dead-time. Then, that phase of the machine is disconnected from the inverter and phase voltage becomes equal to back-emf voltage. Therefore, another method should be used to overcome the distortion resulting from zero-current clamping in addition to the volt-second method.

Another weakness of the volt-second compensation is the variation of the parameters used in the calculation of the volt-second error. The nominal values of the diode forward voltage and turn-on/off times are used in the compensation. However, these parameters are subject to change with changing current level and temperature. Compensation methods based on the disturbance observer should be employed to overcome the parameter variation problem.

Another problem faced in the high performance PMSM drive is the implementation of the synchronous frame current regulator. Synchronous frame current regulation makes the closed-loop system robust to the operating frequency since ac currents at synchronous frequency become dc quantities. However, d- and q-axis voltages, currents and rotor velocity terms in the synchronous frame are coupled to each other. These couplings degrade the performance of the controller with the increasing frequency of the electrical excitation. Decoupling method is utilized to work out this problem. In CHAPTER 5, detailed analysis of these couplings is made and decoupling method is described. The application of the decoupling method in the simulation and experimental work shows a considerable improvement of the performance of the synchronous frame current regulator. With this method, the effect of the variation of the shaft speed on the d- and q-axis currents nearly vanish, which means that, a better disturbance rejection capability is achieved. The maximum deviation on the q-axis current for a 600 rpm step change on the shaft speed is decreased approximately by 50%.

Decoupling algorithm needs d- and q-axis inductances and permanent-magnet flux linkage values. Permanent-magnet flux linkage magnitude varies with the temperature. d- and q-axis inductances change with the amplitude of the phase current due to nonlinearity of the magnetic material or saturation. In a future study, these parameters used in decoupling algorithm can be updated using online parameter estimation algorithms.

In this thesis, besides the torque control, the speed control of the PMSM is also realized. Specifically, the effect of the disturbance torques is analyzed. The conventional P-I speed controller is found to be inadequate for compensation of the disturbance torques due to its finite bandwidth.

In order to increase the disturbance rejection capability of the speed control, load torque estimation algorithm is implemented. This algorithm is introduced and explained in CHAPTER 5. It is proved that, in addition to the disturbance torque rejection, load torque estimation algorithm can also handle the parameter variation problem. These parameters are the effective inertia and motor torque constant which are likely to change during the operation.

The angular acceleration information needed for the load torque estimation is obtained through a Kalman filter from noisy shaft speed measurements. A discrete-time Kalman filter is utilized for this purpose.

The load torque estimation algorithm is implemented both in simulation and in hardware. The performance of the algorithm is tested comprehensively. A substantial improvement is achieved in the disturbance rejection capability of the speed controller with the proposed load torque estimator. A better transient response of the speed controller against the disturbance torque is attained with the use of this method. 200 ms transient response time for 1.3 Nm step load torque change decreases to 50 ms by means of the load torque estimation.

The critical point in the load torque estimation is the extraction of the angular acceleration from noisy speed measurements. In the study, a linear discrete-time Kalman filter is utilized for this purpose. The frequency response of this filter is adjusted by changing the model noise covariance value used by the filter. A following work should attempt to utilize the other version of the Kalman filter for a better frequency response.

A common problem faced in all of the algorithms utilized in this study is the delays in the control loops. The sources of the delays can be listed as;

- delays in the sampling of the feedback signals,
- delays due to digital computation and
- delays in the actuation.

Delays in the control loop degrade the performance of the controllers. Moreover, they decrease the effectiveness of the applied algorithms. High speed sensors and analog-to-digital converters should be utilized for high performance drive applications. The parallel processing capability of FPGAs can be used in order to achieve smaller digital computation delay. The investigation of a method that compensates the delays in the system will be a good candidate for a future study.

There are mainly three original points in the thesis. One of them is to analyze the nonideal nature of the VSIs with Power MOSFETs and the implementation of the volt-second method in these VSIs. In the literature, this work is done for VSIs with IGBTs. The second point is the current polarity determination method in the volt-second compensation algorithm. The current polarities are determined using the measured rotor angle information and the computed torque angle. The proposed method does not require the d-axis current to be zero. These two points are emphasized in [43]. The third original point is the use of Kalman filter for load torque estimation algorithm. The acceleration information needed for the load torque estimation is extracted successfully from the noisy velocity measurements by means of a Kalman filter.

This thesis is focused on improving the torque and speed control performance of PMSM drive without a modification on the hardware. The study tries to resolve the problems originating from the imperfections in the electric drive system by implementing some sophisticated algorithms. The computational burden of these algorithms is not a problem for the emerging DSPs. In the wake of this study, a significant improvement of the torque and speed control performance of PMSM drive is achieved without increasing the cost of the system.

REFERENCES

[1] R. Krishnan. “Electric Motor Drives: Modeling, Analysis and Control”, Prentice Hall, 2001.

[2] P. Vas. “Sensorless Vector and Direct Torque Control”, Oxford University Press, 1998.

[3] D. W. Novotny and T. A. Lipo. “Vector Control And Dynamics Of AC Drives”, Oxford University Press, 1996.

[4] N. Mohan. “Advanced Electric Drives”, Mnpere, 2001.

[5] R. Monajemy, “Control Strategies and Parameter Compensation for Permanent Magnet Synchronous Motor Drives”, PhD Thesis, Virginia Polytechnic Institute and State University, 2000.

[6] “Dynamics and Control of AC Drives”, lecture notes, University of Wisconsin Madison, 2010.

[7] J. Kang, G. Xu, J. Xu, C. Zhou, “Study of Compensation Method on Dead-time Effects for VSI Fed Drive Systems”, Power Electronics Specialists Conference, 2007. IEEE , vol., no., pp.548-552, 17-21 June 2007.

[8] H. -W. Kim, M. -J. Youn, K. –Y Cho, H. -S Kim, “Nonlinearity Estimation and Compensation of PWM VSI for PMSM Under Resistance and Flux Linkage Uncertainty”, IEEE Transactions on Control Systems Technology, Vol. 14, No. 4, JULY 2006.

[9] L. Ben-Brahim, “On the Compensation of Dead Time and Zero-Current

Crossing for a PWM-Inverter-Controlled AC Servo Drive”, IEEE Transactions on Industrial Electronics, Vol. 51, No. 4, October 2004.

[10] Ö. Göksu, “Shaft Transducerless Vector Control of the Interior Permanent Magnet Motor With Speed and Position Estimation Using High Frequency Signal Injection and Flux Observer Methods”, M.Sc. thesis, Middle East Technical University, Turkey, 2008.

[11] N. O. Çetin, “Design And Implementation Of Advanced Pulse Width Modulation Techniques And Passive Filters For Voltage Source Inverter Driven Three-Phase Ac Motors”, M.Sc. thesis, Middle East Technical University, Turkey, 2010.

[12] A. M. Hava, R. J. Kerkman, T. A. Lipo, “Simple Analytical and Graphical Methods for Carrier-Based PWM-VSI Drives”, IEEE Transactions on Power Electronics, Vol. 14, No. 1, January 1999.

[13] S. Chakrabarti, T.M. Jahns, R.D. Lorenz, “Current Regulation for Surface Permanent-Magnet Synchronous Motor Drives Using Integrated Current Sensors in Low-Side Switches”, IEEE Transactions on Industry Applications, Vol. 42, No. 4, July/August 2006.

[14] J. Holtz, “State of the Art of Controlled AC Drives without Speed Sensor”, Power Electronics and Drive Systems Conference Records, pp. 1-6, Singapore, 1995.

[15] H. Kim, M. Degner, J.M. Guerrero, F. Briz, R.D. Lorenz, “Discrete-time Current Regulator Design for AC Machine Drives”, IEEE Transactions on Industry Applications, Vol. 46, No. 4, pp. 1425-1435, July/August 2010.

[16] T. Rowan, R. Kerkman, “A New Synchronous Current Regulator and an Analysis of Current-regulated PWM Inverters”, IEEE Trans. On Ind. Appl., vol. IA-22, no. 4, pp. 678-690, July/August 1986.

[17] L. Laurila, “Analysis of Torque and Speed Ripple Producing Nonidealities of Frequency Converters in Electric Drives”, PhD thesis, Lappeenranta University of Technology, Finland, 2004.

[18] D. G. Holmes, T. A. Lipo, “Pulse Width Modulation For Power Converters”, IEEE Press, 2003.

[19] N. Mohan, T. M. Undeland, W. P. Robbins, “Power Electronics Converters, Applications and Design”, John Wiley & Sons, 1995.

[20] Y. Murai, T. Watanabe, H. Iwasaki, “Waveform Distortion and Correction Circuit for PWM Inverters with Switching Lag-Times”, IEEE Transactions on Industry Applications, Vol. IA-23, No. 5, September/October 1987.

[21] T. Sukegawa, K. Kamiyama, T. Matsui, and T. Okuyama, “Fully digital, vector-controlled PWM VSI-fed AC drives with an inverter dead-time compensation strategy,” in *IEEE Ind. Applicat. Soc. Annual Meet.,* pp. 463469, 1988.

[22] J. Seung-Gi and P. Min-Ho Park, “The analysis and compensation of dead time effects in PWM inverters,” *IEEE Trans. on Ind. Electronics,* vol. 38, no. 2, pp. 108—114, April 1991.

[23] F. Blaabjerg, J. K. Pedersen, and P. Thoegersen, “Improved modulation techniques for PWM-VSI drives,” *IEEE Trans. On Industrial Electronics,* vol. 44, no. 1, pp. 87-95, 1997.

[24] R. B. Sepe and J. H. Lang, “Inverter nonlinearities and discrete-time vector current control,” IEEE Trans. on Industry Applications, vol. 30, no. 1, 1994, pp. 62-70.

[25] J. W. Choi and S. K. Sul, “Inverter output voltage synthesis using novel dead time compensation,” *IEEE Trans. Power Electron.*, vol. 11, pp. 221–227, Mar. 1996.

[26] D. Leggate and R. J. Kerkman, “Pulse-based dead-time compensator for PWM voltage inverters,” *IEEE Trans. Ind. Electron.*, vol. 44, no. 2, pp. 191–197, Apr. 1997.

[27] A. R. Munoz, and T. A. Lipo, “On-line dead-time compensation technique for open-loop PWM-VSI drives,” *IEEE Trans. On Power Electronics*, vol. 14, no. 4, pp. 683-689, 1999.

[28] J. W. Choi and S. K. Sul, “A new compensation strategy reducing voltage/current distortion in PWM VSI systems operating with low output voltages,” *IEEE Trans. Ind. Applicat.*, vol. 31, pp. 1001–1008, Sept./Oct. 1995.

[29] L. Ben-Brahim, “The analysis and compensation of dead-time effects in three phase PWM inverters,” in *Proc. IEEE IECON’98*, pp. 792–797, 1998.

[30] H. Zhao, Q. M. J. Wu, and A. Kawamura, “An accurate approach of nonlinearity compensation for VSI inverter output voltage,” IEEE Trans. Power Electronics, vol. 19, no. 4, July 2004. pp. 1029–1035.

[31] K. Hyun-Soo, K. Kyeong-Hwa, and Y. Myung-Joong, “On-line dead-time compensation method based on time delay control,” *IEEE Trans. on Control Systems Technology,* vol. 11, no. 2, pp. 279-285, 2003.

[32] P. Shihong, and T. M. Jahns, "A novel dead-time elimination method using single-input enhanced phase-leg configuration." *Proc. of IEEE Industry Applications Conf.,* vol. 3, pp. 2033-2040, 2003.

[33] N. Urasaki, T. Senjyu, T. Kinjo, T. Funabashi and H. Sekine, “Dead-time compensation strategy for permanent magnet synchronous motor drive taking zero-current clamp and

parasitic capacitance effects into account", IEE Proc.-Electr. Power Appl., Vol. 152, No. 4, July 2005.

[34] N. Urasaki, T. Senjyu, K. Uezato et al., "An adaptive dead-time compensation strategy for voltage source inverter fed motor drives," *IEEE Trans. on Power Electronics,* vol. 20, no. 5, pp. 1150-1160, 2005.

[35] K. Wiedmann, F. Wallrapp, A. Mertens, "Analysis of inverter nonlinearity effects on sensorless control for permanent magnet machine drives based on High-Frequency Signal Injection," *Power Electronics and Applications, 2009. EPE '09. 13th European Conference on*, vol., no., pp.1-10, Sept. 2009.

[36] R. Raute, C. Caruana, C.S. Staines, J. Cilia, M. Sumner, G.M. Asher, "Analysis and Compensation of Inverter Nonlinearity Effect on a Sensorless PMSM Drive at Very Low and Zero Speed Operation," *Industrial Electronics, IEEE Transactions on*, vol. 57, no. 12, pp.4065-4074, Dec. 2010.

[37] X. Yuan, I. Brown, R.D. Lorenz, A. Qui, "Observer-based inverter disturbance compensation," *Energy Conversion Congress and Exposition, 2009. ECCE 2009. IEEE,* vol., no., pp.2520-2527, 20-24 Sept. 2009.

[38] R. D. Lorenz, D. B. Lawson, "Performance of feed forward current regulators for field oriented induction machine controllers," *IEEE Trans. Ind. Applicat.*, vol. 23, pp. 597–602, July/Aug. 1987.

[39] H. Kobayashi, S. Katsura, K. Ohnishi, "An Analysis of Parameter Variations of Disturbance Observer for Motion Control," *IEEE Transactions on Industrial Electronics*, Vol. 54, No. 6, December 2007.

[40] D. Simon, *Optimal State Estimation*, John Wiley and Sons Inc., New Jersey, 2006.

[41] P.B. Schmidt, R.D. Lorenz, "Design Principles and Implementation of Acceleration Feedback to Improve Performance of dc Drives," *IEEE Transactions on Industry Applications*, Vol 28, No 3, May/June 1992.

[42] K. Hasse, "Zur Dynamik Drehzahlgeregelter Antriebe mit Stromrichtergespeisten Asynchron-Kurzschlusslaufermachinen," PhD Dissertation, Tech. Hochschule Darmstadt, July 1969.

[43] Ü. Büyükkeleş, A. Ersak "Analysis and Compensation of Nonlinear Effects in an Inverter with Power MOSFETs," *15th International Power Electronics and Motion Control Conference, EPE-PEMC 2012 ECCE Europe*, Novi Sad, Sept. 2012. (accepted).

[44] Y.S. Jeong, S.K. Sul, "Analysis and Design of a Decoupling Current Controller for AC Machines," in *Proc. of IEEE IAS Annual Meeting*, Hong Kong, pp. 751-758, 2005.

[45] F. Briz, M.W. Degner, R.D. Lorenz, "Analysis and Design of Current Regulators Using Complex Vectors," *IEEE Trans. on Ind. Appl.*, vol. 36, pp. 817-825, 2000.

[46] F. Briz, M. W. Degner and R. D. Lorenz, "Dynamic analysis of current regulators for ac motors using complex vectors," *IEEE Trans. Industry Applications*, vol. 35, pp. 1424–1432, Nov./Dec. 1999.

[47] Y. Hori, "Disturbance Suppression on an Acceleration Control Type DC Servo System," *19th Annual IEEE Power Electronics Specialists Conference*, 1988.

APPENDIX A

ELECTROMAGNETIC POWER EQUATION IN ROTOR REFERENCE FRAME

In this appendix, the electromagnetic power equation in rotor reference frame is derived.

The instantaneous power supplied to a PMSM can be calculated as the product of the instantaneous phase voltages and currents,

$$P_{ins} = v_{sa}i_{sa} + v_{sb}i_{sb} + v_{sc}i_{sc}\,. \tag{A.1}$$

The instantaneous power can also be calculated from voltage and current space vectors,

$$\vec{v}_s^a(\vec{i}_s^a)^* = \frac{2}{3}[v_{sa} + \vec{a}v_{sb} + \vec{a}^2v_{sc}]\frac{2}{3}[i_{sa} + \vec{a}^2i_{sb} + \vec{a}i_{sc}]$$

$$= \frac{4}{9}[v_{sa}i_{sa} + v_{sb}i_{sb} + v_{sc}i_{sc} + \vec{a}(v_{sa}i_{sc} + v_{sb}i_{sa} + v_{sc}i_{sb})$$

$$+\vec{a}^2(v_{sa}i_{sb} + v_{sb}i_{sc} + v_{sc}i_{sa})]\,. \tag{A.2}$$

$(\vec{i}_s^a)^* = \frac{2}{3}[i_{sa} + \vec{a}^2i_{sb} + \vec{a}i_{sc}]$ is the complex conjugate of the current space vector. Real part of the expression can be written using (2.13),

$$Re\{\vec{v}_s^a(\vec{i}_s^a)^*\} = \frac{4}{9}[v_{sa}i_{sa} + v_{sb}i_{sb} + v_{sc}i_{sc}$$

$$-0.5v_{sa}(i_{sb} + i_{sc}) - 0.5v_{sb}(i_{sa} + i_{sc}) - 0.5v_{sc}(i_{sa} + i_{sb})]$$

$$= \frac{2}{3} v_{sa} i_{sa} + v_{sb} i_{sb} + v_{sc} i_{sc} \,. \tag{A.3}$$

Therefore, instantaneous power into the machine can be found as:

$$P_{ins} = \frac{3}{2} Re[\vec{v}_s^a (\vec{i}_s^a)^*]. \tag{A.4}$$

The power equation can be written in terms of rotor reference frame variables using (2.32),

$$P_{ins} = \frac{3}{2} Re[\vec{v}_s^a (\vec{i}_s^a)^*] = \frac{3}{2} Re\left[\vec{v}_s^d \left(\vec{i}_s^d\right)^*\right] . \tag{A.5}$$

Using (2.30),

$$P_{ins} = \frac{3}{2} \left(v_{sd} i_{sd} + v_{sq} i_{sq}\right) . \tag{A.6}$$

Note that, the power supplied to the three-phase winding is $3/2$ times the power through the d- and q-axis winding set. This is due to the normalization factor 2/3 which is used in non-power invariant space vector definition. For power invariant form, normalization factor should be taken as $\sqrt{2/3}$ instead of 2/3.

Inserting (2.46) and (2.47) into (A.6),

$$P_{ins} = \frac{3}{2} \Big[\left(R_s {i_{sd}}^2 + R_s {i_{sq}}^2\right) + \left(\frac{1}{2} L_d \frac{d}{dt} {i_{sd}}^2 + \frac{1}{2} L_q \frac{d}{dt} {i_{sq}}^2\right)$$

$$+ w_r \left(L_d i_{sd} i_{sq} + \lambda_{PM} i_{sq} - L_q i_{sq} i_{sd}\right) \Big] . \tag{A.7}$$

The power equation consists of three different terms. First term accounts for resistive power loss. Second term accounts for time rate of change of the magnetic energy stored in inductances. The last term corresponds to the power transferred to the air gap which is generally named as electromechanical power.

APPENDIX B

ANALYSIS OF DIFFERENT TORQUE ANGLE CONDITIONS

In this appendix, the different torque angle control methods are examined.

- **Zero direct-axis current control**

In zero direct-axis current control technique, torque angle δ is constant at 90^0 therefore, $i_{sd} = 0$. This method is analogous to a separately-excited dc machine. It is commonly used for speed control applications in a range of speeds lower than the base speed [5]. It is easy to implement. Vector diagram of this method can be seen in Figure B.1.

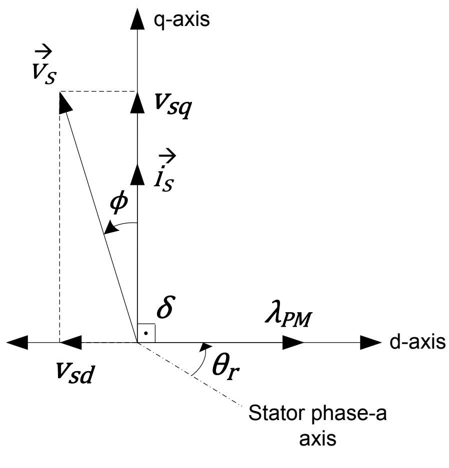

Figure B.1. Zero direct axis current control vector diagram.

Steady-state voltage equations can be written as:

$$v_{sd} = -w_r L_q i_{sq} \tag{B.1}$$

$$v_{sq} = R_s i_{sq} + w_r \lambda_{PM} \; . \tag{B.2}$$

Note that, $i_{sd} = 0$ and derivative terms in the voltage equation are zero at steady state. The magnitude of the voltage space vector is,

$$|\vec{v}_s^a| = \sqrt{v_{sd}^2 + v_{sq}^2} = \sqrt{\left(w_r L_q i_{sq}\right)^2 + \left(R_s i_{sq} + w_r \lambda_{PM}\right)^2} \; . \tag{B.3}$$

Power factor can be written as:

$$\cos \emptyset = \frac{|v_{sq}|}{|\vec{v}_s^a|} = \frac{1}{\sqrt{1 + \frac{(L_q i_{sq})^2}{\left(\frac{R_s i_{sq}}{w_r} + \lambda_{PM}\right)^2}}} \tag{B.4}$$

or alternatively,

$$\cos \emptyset = \frac{1}{\sqrt{1 + \frac{(w_r L_q)^2}{\left(R_s + \frac{w_r \lambda_{PM}}{i_{sq}}\right)^2}}} \; . \tag{B.5}$$

(B.4) and (B.5) show that, the power factor deteriorates for increasing rotor speed and increasing stator current.

In order to determine the maximum permissible speed in this method, neglecting the resistive drop in (B.3) we get,

$$w_{r_{max}} = \frac{|\vec{v}_s^a|_{max}}{\sqrt{(L_q i_{sq})^2 + {\lambda_{PM}}^2}} \; . \tag{B.6}$$

As seen, the maximum speed is dictated by the maximum stator voltage.

- **Unity power factor control**

Unity power factor control method tries to lock the power angle $\emptyset$ to 0^0 by controlling the torque angle. The vector diagram for this method takes the form shown in Figure B.2.

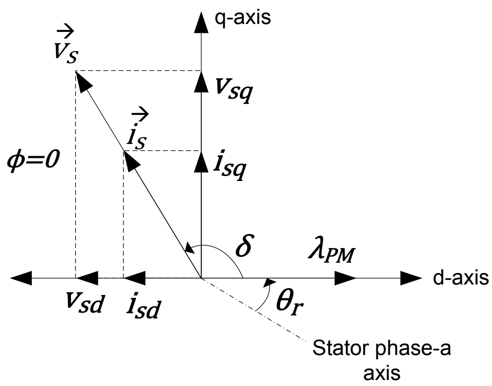

Figure B.2. Unity power factor control vector diagram.

The torque angle δ can be determined from,

$$\frac{v_{sq}}{v_{sd}} = \frac{i_{sq}}{i_{sd}} = \tan\delta\,. \tag{B.7}$$

Substituting (B.1) and (B.2) into (B.7) and using the non-saliency of the rotor, the torque angle becomes,

$$\delta = \cos^{-1}\left(-\frac{L_q|i_s|}{\lambda_{PM}}\right). \tag{B.8}$$

- **Constant air gap flux control**

Constant air gap flux control has an advantage of limiting the air gap flux linkage to avoid saturation of the core. In general, the air gap flux is kept constant at λ_{PM},

$$\sqrt{(L_q i_{sq})^2 + (L_d i_{sd} + \lambda_{PM})^2} = \lambda_{PM}\,. \tag{B.9}$$

Rearranging (B.9) and again using non-saliency, the torque angle δ can be found as,

$$\delta = \cos^{-1}\left(-\frac{L_q|i_s|}{2\lambda_{PM}}\right). \tag{B.10}$$

- **Maximum torque per ampere control**

The maximum torque per ampere control method requires high saliency ratio. In non-salient machine it is equivalent to zero direct axis current control. Therefore, this method is not analyzed in this thesis.

- **Flux weakening control**

The flux weakening control is needed when the machine is operated over the base speed. Up to the base speed machine is operating on constant torque region and over the base speed it can be operated on constant power region as shown in Figure B.3.

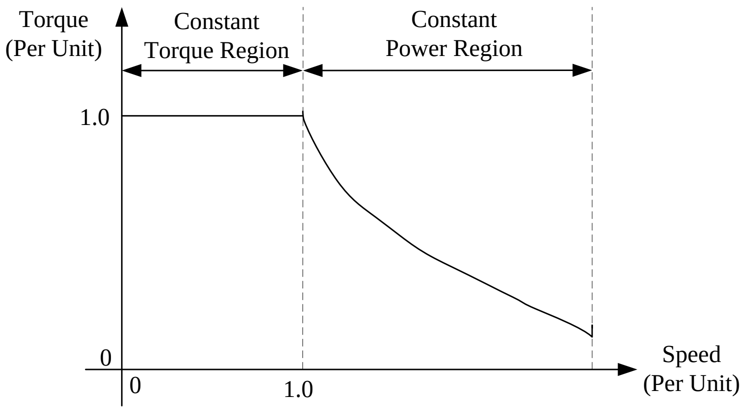

Figure B.3. Torque speed capability curve.

Flux linkage of the permanent magnets cannot be controlled, but the air gap flux which is equal to $\sqrt{(L_q i_{sq})^2 + (L_d i_{sd} + \lambda_{PM})^2}$, can be reduced by injecting negative d-axis current i_{sd}. By this method, developed voltages in the stator windings are decreased and speed limit can be exceeded. However, flux weakening capability of the machine depends on the ratio $\frac{\lambda_{PM}}{L_d}$. In general, for surface mounted PMSM, direct-axis inductances are relatively small due to the large air gap. Also flux linkage of the permanent magnets is relatively high because magnets are the only sources of torque. Therefore, surface mounted PMSMs generally have poor flux weakening capability [6], [13].

APPENDIX C

STEADY-STATE ANALYSIS OF SURFACE-MOUNTED PMSM

In this appendix, the steady-state analysis of the surface-mounted PMSM is given.

Voltage equation of stator phase-a winding, (2.1) can be written using (2.5), (2.11) and (2.13) as,

$$v_{sa} = R_s i_{sa} + L_s \frac{d}{dt} i_{sa} + e_a \tag{C.1}$$

where L_s is the *synchronous inductance* which includes the effect of the mutual coupling from the other two phases as well as the self-inductance of the corresponding phase. Synchronous inductance, L_s can be written as,

$$L_s = L_{ls} + \frac{3}{2} L_{ms} \,. \tag{C.2}$$

e_a is *internal voltage* produced by the permanent-magnet field, which is proportional to the permanent-magnet field strength and the rotor speed,

$$e_a = -w_r \lambda_{PM} \sin \theta_r \,. \tag{C.3}$$

For sinusoidal excitation, the steady-state voltage equation can be written using phasor representation with the rotor flux rotating synchronously at angular frequency of the ac excitation ($w_r = w_e$)

$$\hat{V}_a = R_s \hat{I}_a + jX_s \hat{I}_a + \hat{E}_a \tag{C.4}$$

where X_s is the *synchronous reactance* defined as,

$$X_s = w_e L_s \tag{C.5}$$

Equivalent circuit and phasor diagram of the surface mounted PMSM in sinusoidal steady-state is shown in Figure C.1.

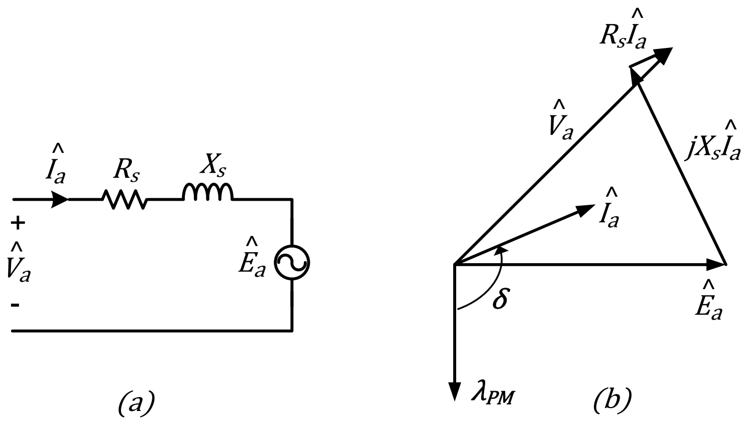

Figure C.1. Per phase equivalent circuit (a) and phasor diagram (b) of the surface-mounted PMSM

Active power input to the internal voltage for phase-a can be found as,

$$P_{in,a} = E_{rms} I_{rms} \cos\left(\frac{\pi}{2} - \delta\right). \quad \text{(C.6)}$$

Total active power delivered to the internal voltage is three times the one calculated for single phase. The electromagnetic torque of the machine can be obtained from active power input to the internal voltage (back-emf) divided by the mechanical rotor speed,

$$T_e = 3\frac{E_{rms} I_{rms}}{w_m} \sin\delta. \quad \text{(C.7)}$$

The rms amplitude of E_a is proportional to the permanent-magnet field strength and the rotor speed,

$$E_{rms} = \frac{w_r \lambda_{PM}}{\sqrt{2}}. \quad \text{(C.8)}$$

Mechanical rotor speed is related to the angular frequency of the rotor flux,

$$w_m = \frac{w_r}{P/2}. \quad \text{(C.9)}$$

Using (C.8) and (C.9), (C.7) can be written as,

$$T_e = \frac{3}{\sqrt{2}}\frac{P}{2}\lambda_{PM} I_{rms} \sin\delta. \quad \text{(C.10)}$$

The torque expression obtained here is very similar to corresponding equation for a dc machine if $\delta = 90^0$.

APPENDIX D

SIMULATION MODELS USED IN THE THESIS

In this appendix, the Simulink models used through the simulation studies of this thesis are given.

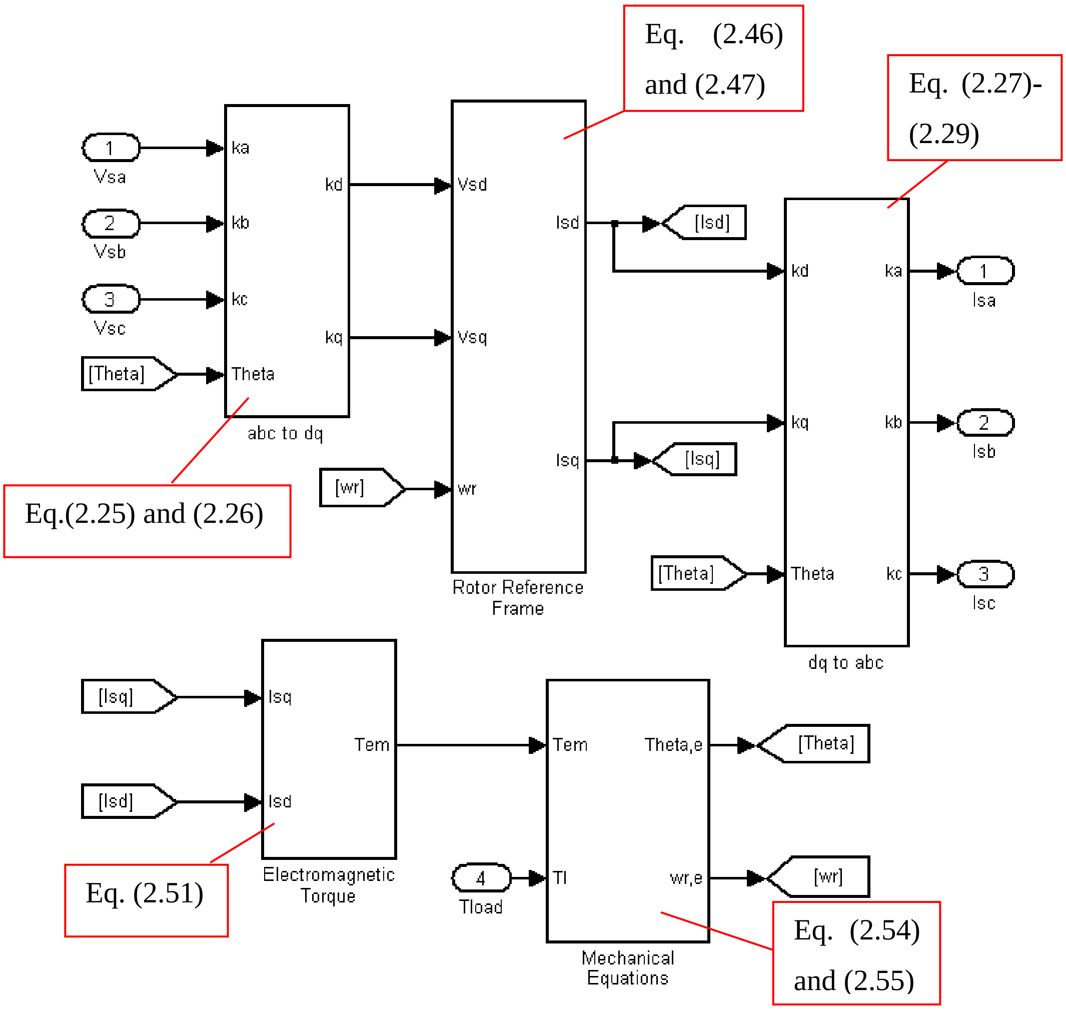

Figure D.1. Mathematical model of the PMSM used in the simulation work.

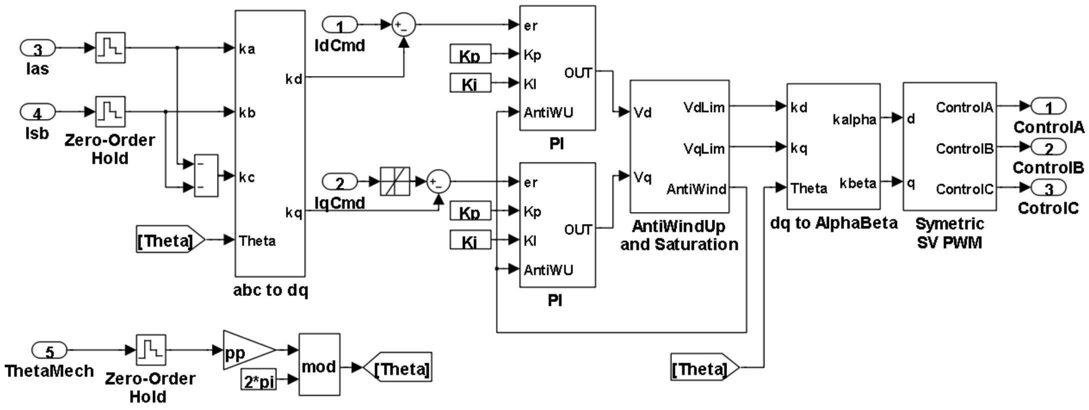

Figure D.2. Simulation model for vector control algorithm.

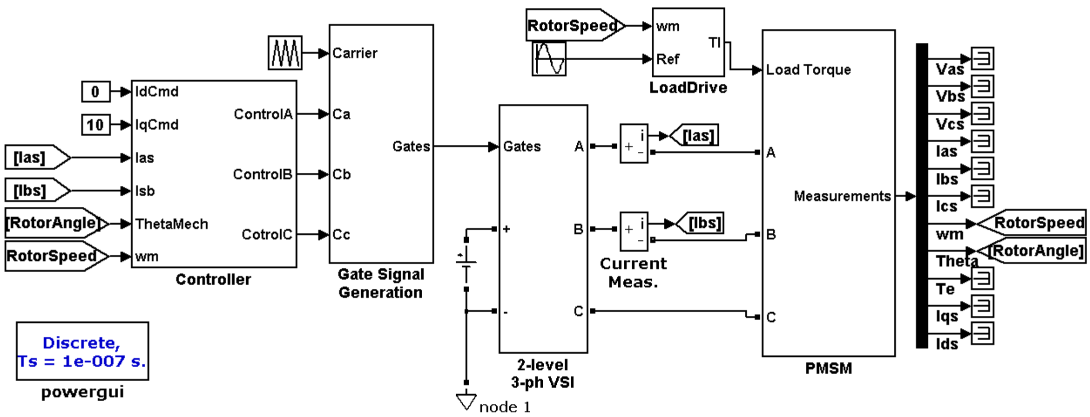

Figure D.3. Complete simulation model of the electric drive system.

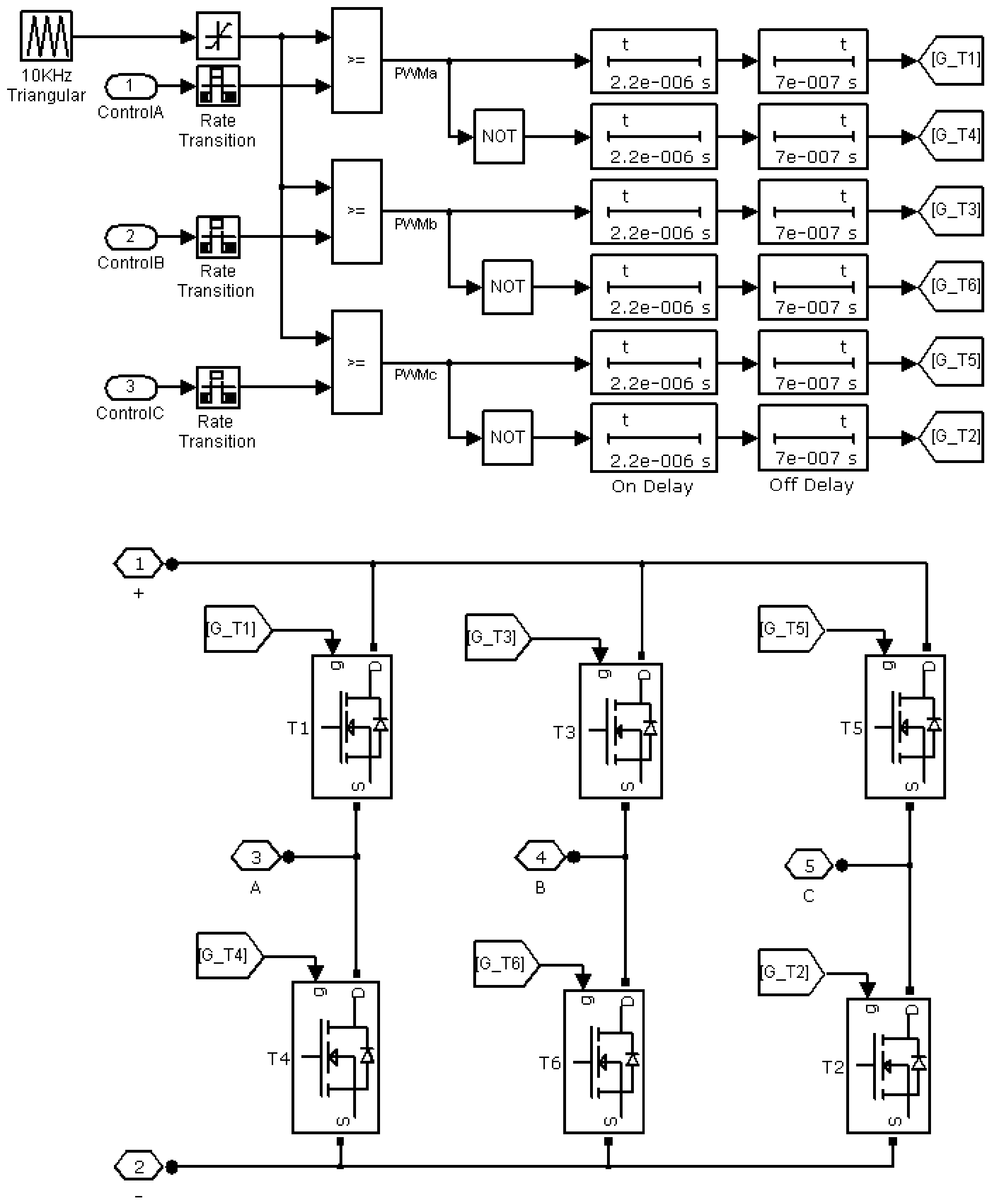

Figure D.4. Simulation model used in VSI nonlinearity study.

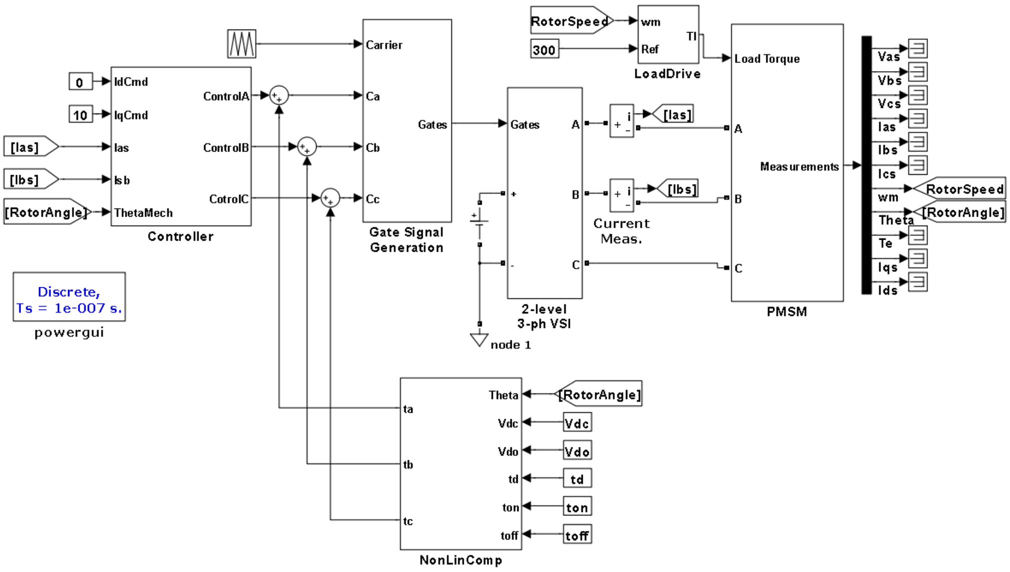

Figure D.5. Volt-second compensation method in the simulation study.

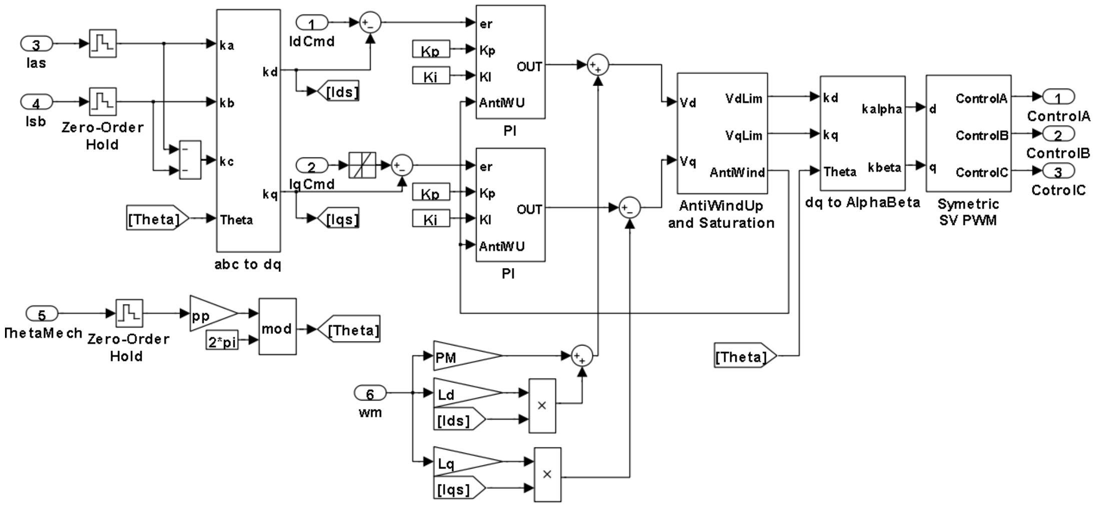

Figure D.6. Implementation of the decoupling method in the simulation.